UiT
THE ARCTIC
UNIVERSITY
OF NORWAY

Faculty of Science and Technology
Department of Physics and Technology

Distributed Renewable Generation and Power Flow Control to Improve Power Quality at Northern Senja, Norway

Tobias Thørnquist Jacobsen

EOM 3901 - Masters Thesis in Energy, Climate and Environment

June 2019

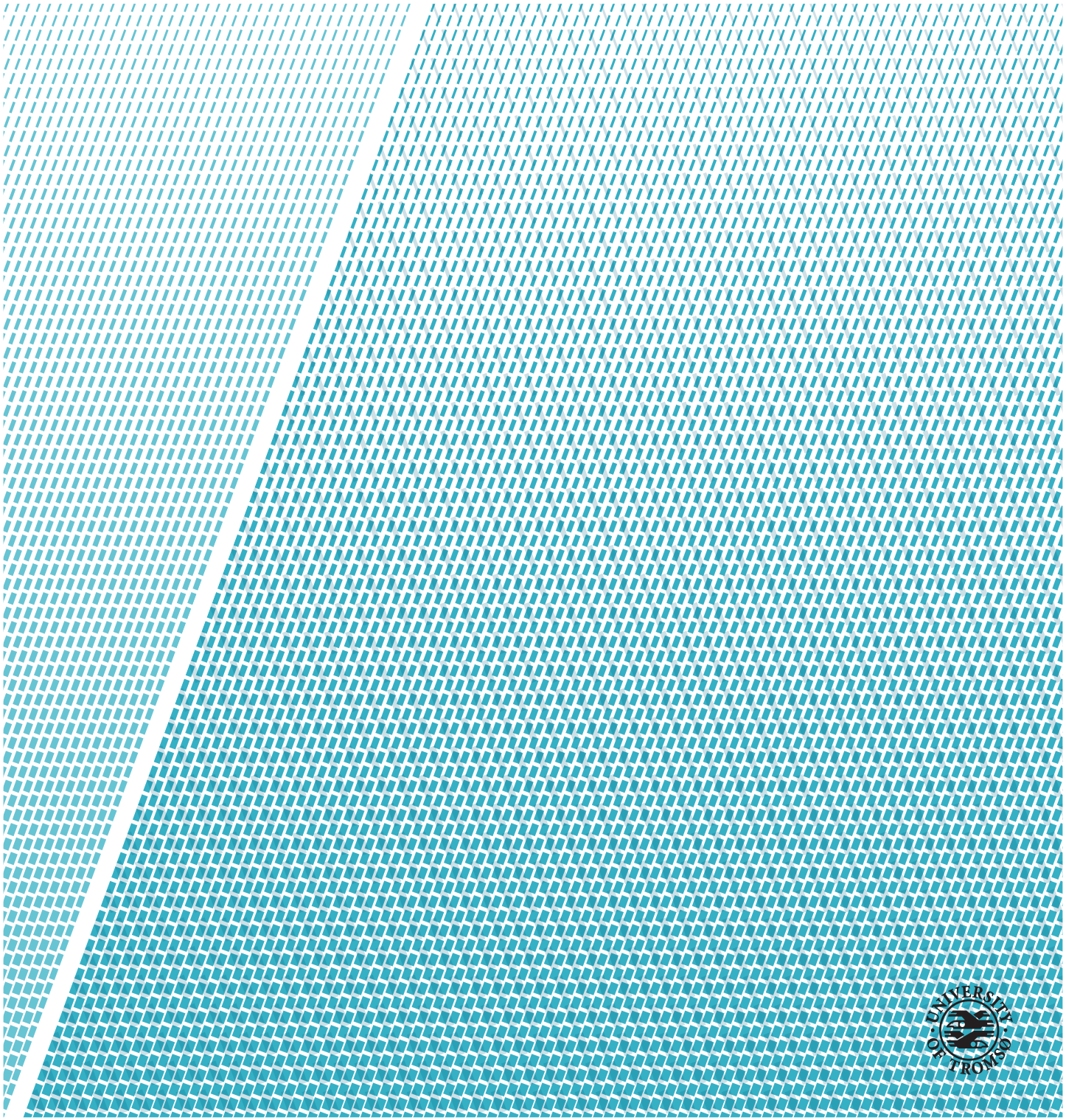

Abstract

Distributed renewable generation and power flow control are promising technologies for increasing power system efficiency. Renewable energy production close to consumption reduces need for transport of power to these locations. The benefits of reactive flow control are well documented, and in recent years the use of energy storage for active power control has increased in relevance. The power system at Senja in northern Norway is suffering from limited transfer capacity, and the energy demand is expected to increase in coming years. In this thesis, the performance of distributed renewable generation and power flow control is evaluated. The potential production of solar and wind energy systems at the island is quantified through simulations, and the effect this production can have on network performance is discovered. Shunt capacitors for reactive power compensation, and energy storage systems for peak load shaving are also evaluated in terms of network performance. A good potential for renewable generation is found, especially for wind. It is found that 20 % of the bottleneck feeder load can be released as a result of renewable generation, which limits requirements for hydro production. However, the main feeder will become overloaded with increasing demand, even with the addition of renewable generation. Implementation of power flow control measures shows promising results, enabling a reduction of 30-50 % in voltage drops during heavy load in the distribution network. Network losses are also reduced, which indicates that the network operates more efficiently. From these results, it is evident that the components considered will have the possibility to enhance network performance. Based on these observations, additional topics to be analyzed in further work is proposed.

Acknowledgements

I would like to thank everyone that has made my studies at the University of Tromsø such an exciting and memorable time. Fellow students and all of my friends, you have made these past five years one of the best periods of my life. A special thanks goes to Tuomas Heiskanen, for always taking the time to share your broad knowledge with all of your classmates.

I would like to thank my supervisor Tobias Boström, and my co-supervisor Ronald Hardersen, for valuable guidance and help during this project. I would also like to thank Sigurd Bakkejord at *Troms Kraft Nett*, for taking the time to guide and provide valuable input on power system analysis. I could not imagine how this thesis would have been without the knowledge they have shared.

I am forever grateful for the support I have received from my family throughout my studies, thank you. And thank you, my dear Stine, for supporting me in everything I do.

Contents

List of Figures

List of Tables

Abbreviations

AC Alternating Current

AM Air Mass

BESS Battery Energy Storage System

DC Direct Current

DFIG Doubly Fed Induction Generator

EoT Equation of Time

GHI Global Horizontal Irradiance

GIS Geographical Information System

HAWT Horizontal Axis Wind Turbine

HRA Sun Hour Angle

IEC International Electrotechnical Commission

IFS Integrated Forecasting System

LST Local Solar Time

LSTM Local Standard Time Meridian

LT Local Time

MPPT Maximal Power Point Tracking

NOCT Nominal Cell Operating Temperature

pf Power Factor

PFC Power Factor Correcting Capacitor

PMSG Permanent Magnet Synchronous Generator

PV Photovoltaic

SCC Shunt capacitor compensation

SCIG Squirrel Cage Induction Generator

SCR Short Circuit Ratio

STATCOM Static Synchronus Generator

STC Standard Test Conditions

SVC Static Var Compensator

TC Time Correction

TSR Tip-Speed Ratio

uf Utilization Factor

UTC Universal Coordinated Time

VAWT Vertical Axis Wind Turbine

VSC Voltage Source Converter

WRF Weather Research and Forecasting Model

Nomenclature

δ	Solar Declination Angle	degrees
γ	Impedance Angle	degrees
θ_z	Solar Zenith Angle	degrees
I_{DIF}	Diffuse Irradiance	$\frac{\mathrm{W}}{\mathrm{m}^2}$
I_{DN}	Direct Normal Irradiance	$\frac{\mathrm{W}}{\mathrm{m}^2}$
I_{GH}	Global Horizontal Irradiance	$\frac{\mathrm{W}}{\mathrm{m}^2}$
S_0	Solar Constant	$\frac{\mathrm{W}}{\mathrm{m}^2}$
S_k	Short Circuit Capacity	VA
α	Solar Elevation Angle	degrees
β	Collector Tilt	degrees
$\dot{m}$	Mass Flow Rate	kg/s
η	Effciency	%
$\overline{x}$	Mean Sample Value	
Φ	Solar Azimuth Angle	degrees
ϕ	Latitude	degrees
ρ	Density	$\frac{\mathrm{kg}}{\mathrm{m}^3}$
ρ_r	Ground Reflectance	%

σ	Sample Standard Deviation	
σ^2	Sample Variance	
I	Current	A
I_{RC}	Reflected Irradiance on Collector	$\frac{\mathrm{W}}{\mathrm{m}^2}$
P	Active Power	W
Q	Reactive Power	var
R	Resistance	Ω
r	Pearson Correlation Coefficient	
S	Complex Power	VA
X	Reactance	Ω
Z	Impedance	Ω
A	Area	m^2
a	Transformer Turn Ratio	
bias	Sample Bias	
E	Energy	Wh
l	Surface Roughness Length	m
m	Mass	kg
v	Speed	$\frac{\mathrm{m}}{\mathrm{s}}$
z	Height	m

1 Introduction

1.1 Background

With the shift towards renewable energy technologies in recent years, the implementation of renewable distributed generation has become increasingly relevant. Historically, distribution networks have not been designed to handle the power fluctuations distributed generation can introduce, and thus the effects have to be analyzed when implementation is considered [Vita et al., 2015]. This, in addition to a more fluctuating demand pattern, introduce the need for control in distribution networks. Reactive power flow control performed by shunt capacitors's effect on distribution system reliability has been well documented for many years [Sallam et al., 1994]. In recent years, utilization of energy storage for increased network reliability has also been studied [Alhamali et al., 2016].

The coastal community at Senja experience limitations in the electrical network, mainly from the increasing energy consumption due to expansions in the seafood industry. The increasing demand is expected to jeopardize stable operation of the power system if measures are not initiated. Today power to the island is supplied by a 66 kV cable, which is nearing its capacity. The 22 kV distribution network feature long radial feeders, which makes the voltage at the end points susceptible to low network voltages during heavy load. These problems impose a risk for unstable and inadequate supply of power, which could have critical consequences for the industrial establishments, which rely on a stable and secure power supply.

1.2 Scope of the Study

The local power distributor *Troms Kraft* in cooperation with the *Artic Centre for Sustainable Energy*, wishes to examine possible solutions that give the power system at northern Senja the robustness it needs for the future. The solution to this question is a complex one, touching upon several topics. In this thesis active and reactive power flow control, as well as distributed renewable energy production, will be considered. The underlying objective is to limit current flow in transmission lines, in order to minimize line losses and voltage drops. If proven effective, these measures can postpone and possibly reduce investment costs in new power transformers, lines and such. In order to confine the scope of this thesis, this work will focus on the performance of the system. Evaluation of the economics is suggested as further study.

The traditional supply of power is based on transmission of power over long distances from large power plants. This methodology impose high requirements on the transmission network. Utilization of distributed generation, enables production of power near the locations it is being consumed at, thus limiting the transmission distance. This can release transmission capacity in parts of the network that are subject to bottleneck problems. In this thesis, the potential of wind and solar production for this application is studied. In order to quantify the potential, yearly simulations on power output is performed.

The solar power plant is a rooftop system, that is simulated at the roof of a to be established fish containment factory owned by *Salmar*. Two possible configurations will be considered, which have different orientation. The solar plant is in the rated capacity range 1-2 MW. The wind power plant will be located in mountainous terrain, and the yearly output of a 9.9 MW system will be considered. The yearly performance of the distributed production systems will be evaluated in terms of how they can improve network performance. The study will revolve around the potential released capacity the power plants can accomplish. As mentioned, the island is constrained on delivering capacity, and with the addition of the new factory, released transfer capacity can prove to be crucial.

As described, the transfer capacity in the radial distribution network at the northern part of the island is also constrained. The thermal capacity in this network is not constraining, however voltage is. A study on the performance of active and reactive power flow control will be conducted. Reactive power control is performed by shunt capacitors, and the active flow control is performed by energy storage. Both the reduction in power losses as well as improvements in voltage regulation are evaluated. The improved performance due to higher voltages can postpone investments for the network operator, and hence enable a sustainable grid operation for the remainder of the existing

network component's lifetime.

1.3 Outline of the Thesis

This thesis will be divided into the following chapters excluding the introduction:

- **Chapter 2** - In the second chapter, a theoretical background on the subjects of this thesis will be presented. The section will provide necessary theory related to the power system, as well renewable energy sources and energy storage. A brief introduction of statistical analysis of data will also be given.

- **Chapter 3** - In this chapter the locations relevant for this thesis are presented. Relevant information on surface conditions and orography will be given. Existing power plants and their location, as well as the existing power network is also introduced.

- **Chapter 4** - The fourth chapter will present the data and methods used in this thesis.

- **Chapter 5** - Potential output of the renewable energy sources will be presented and discussed in this chapter.

- **Chapter 6** - In this chapter the improvement of network performance with the inclusion of the proposed components is presented and discussed.

- **Conclusion** - Summary and concluding remarks is presented.

2

Theoretical Background

2.1 The Modern Power System and its Components

2.1.1 Generation - Synchronous Generators

Most of the power production in the power system of today comes from an electrical machine called the three phase Alternating Current (AC) *Synchronous Generator*. Synchronous Generators transforms mechanical energy into electrical energy through utilization of basic electromagnetic principles. All synchronous generators consists of two magnetic parts, one which is stationary (stator) and one which is rotating (rotor) [Masters, 2013]. When the rotor is subject to a mechanical torque, two rotating magnetic fields are formed. The angle between these δ_r, or rotor angle, determines the power produced by the generator. For grid connected three phase generators it is essential that all generators operates at the same frequency, to synchronize generation assets [Machowski, 2008].

The windings in the rotor are supplied by a Direct Current (DC). This current can be controlled by the generator excitation system. The excitation system alters the current in the DC windings in order to maintain the generator voltage at nominal value. Altering this current also alters the reactive power of the generator, which is a useful effect in reactive power flow control [Saadat, 2010].

2.1.2 Transmission Network

The transmission network is the part of the power system that deliver power from generation to end users. Several voltage magnitudes are utilized in the power system, in order to have an efficient and cost effective power transport [Saadat, 2010]. In Norway, the transmission network is divided into three categories [EnergiNorge, 2018].

- **Central Network** - Long distance, high voltage transmission which delivers power at the highest voltages of 420 kV, 300 kV and 132 kV. The central network delivers power over long distances, and thus require high voltages to limit power losses.

- **Regional Network** - The regional network is a medium distance transmission network that connect the central and distribution network. In the regional network power is transmitted to network substations, in Norway the regional network operates at a voltage of 132, 66, 47 or 32 kV.

- **Distribution Network** - This network transmits power from network substations to costumers. The voltage is stepped down to 400 or 230 V at residential level, and is usually transmitted at 22 - 11 kV from substations. The distribution network mostly feature a radial structure, which can cause high voltage drops in long network feeders. Operation of the distribution network has traditionally been passive, but with new load patterns and distributed generation, active operation might be required. This is due to the fact that weak distribution networks are sensitive to fluctuations, and thus with increasing fluctuations active operation will improve stability [Coster, 2010].

In order to step the voltage between these networks, transformers are used. Transformers step up voltage from generation, and step the voltage down to appropriate utilization voltages. The voltage change from a transformer is described through the *turn ratio*, which is shown in (2.1) [Saadat, 2010].

$$a = \frac{V_1}{V_2} = \frac{N_1}{N_2} \tag{2.1}$$

Where V_1 and V_2 denotes the primary and secondary side voltages, and N_1 and N_2 the number of windings. Transformers usually have the possibility to increase or decrease the number of windings on the secondary side, in order to maintain desirable voltage at the secondary side. In the distribution networks however, this usually has to be performed manually, which in turn becomes costly if the process has to be performed regularly [Coster, 2010].

Complex Power Flow and Bus Classification

In AC systems the power is *complex*, which means that the power has a real and an imaginary part. The complex power (S), is the product of the sinusoidal voltage and current waveforms. The real part is known as *active power* (P), and the imaginary part is known as *reactive power* (Q). The complex power is defined as [Masters, 2013]:

$$S = VI^* = P + jQ \tag{2.2}$$

Where V is voltage, and I^* is the complex conjugate of the current phasor. Reactive power is formed if the current goes out of phase with the voltage. In power lines, this phenomena occurs due to a line's inductive or capacitive properties, which contributes a lagging and leading effect respectively. The magnitude of the complex power, $|S|$ is known as the apparent power. The amount of apparent power injection needed to deliver a certain amount of active power, depends on transmission line and load characteristics [Saadat, 2010].

When the solution of a complex power flow problem is to be found, nodes in the system has some known and some unknown parameters. Based on the parameters known, the nodes are classified as follows [Saadat, 2010]:

- **Slack bus/Swing bus** - The slack bus is usually considered as the systems connection with the interconnected system. In the slack bus, the voltage magnitude and phase angle is fixed. The slack bus can thus be seen upon as a generator with a power rating large enough to maintain nominal voltage during all load conditions.

- **Generator bus** - The generator bus, or PV-bus is a bus where the active power and voltage magnitude is fixed. This is called a generator bus, because it resembles the operation of a generator. The reactive power can be altered to the generator excitation system, and comes from the load flow solution.

- **Load bus** - The load bus, or the PQ-bus, is a bus where the complex power consumption is known. The voltage phase angle and magnitude comes from the load flow solution.

Power Losses in Transmission and Line Constraints

Power losses in transmission lines are a consequence of the *impedance* of the transmission lines. The impedance consists of *resistance* (R) and *reactance* (X) as such:

$$Z = R + jX \tag{2.3}$$

Where R is the per phase line resistance and X is the per phase line reactance. The relation between resistance and reactance defines whether the line is resistive or inductive. This can be expressed through the impedance phase angle γ, which is given as [Saadat, 2010]:

$$\gamma = \cos^{-1}\left(\frac{R}{|Z|}\right) \tag{2.4}$$

High voltage transmission lines typically inherit inductive properties, which corresponds to $\gamma = 55-85$ degrees. Lower voltage lines, such as the distribution network, usually possess resistive properties, corresponding to $\gamma = 25 - 55$ degrees [Tande et al., 2007]. The resistance depends on the conductivity of the conductor material, line length and cross sectional area. The inductance of lines is dependent on the flux linkage between conductors, which increases with increased phase spacing. Active power losses (P_L) in transmission lines are lost due to line resistance. The real three phase power losses are given as [Saadat, 2010]:

$$P_{L(3\phi)} = 3I^2R = \frac{3R}{V^2}(P^2 + Q^2) \tag{2.5}$$

Where I, R and V are the per phase current, resistance and voltage. P and Q is the per phase active and reactive power. (2.5) shows that the line current is an essential value to control in order to reduce line losses. Since the losses also are inversely proportional to the voltage squared, losses are considerably reduced during transport at higher voltages. At extremely high voltages, other losses such as corona discharge might outweigh the reduced resistive losses [Saadat, 2010]. For a given voltage level with a fixed resistance, the only parameter that can be optimized to reduce losses is the current. Since a certain active power is demanded and $I = {}^{S^*}/_{V}$, this can be obtained by limiting reactive power flow in the line. This will be discussed in more detail later in this section.

Transmission lines are limited to a certain flow of apparent power. This is due to the fact that the conductor heats and stretches with increased loading. This can cause sagging of lines, and in order to prevent irreversible damage, a thermal flow constraint is defined. Loading of lines above the thermal constraint, might damage the conductor and greatly reduce component lifetime. The

thermal constraint on power flow of a three phase line is defined in (2.6), where V and $I_{thermal}$ are per phase values [Saadat, 2010].

$$S_{thermal} = 3V * I_{thermal} \tag{2.6}$$

Voltage Drop in Transmission

When current flows, the impedance of the transmission line induces a potential opposite to the direction of flow. This causes the voltage to reduce with line length. Several models for transmission lines, which vary in complexity are available. The most complex models are suitable for long distance high voltage lines, where phenomena such as charging through line capacitance cannot be neglected. Shorter lines at low voltage can be approximated by only considering the series impedance of the line, which means that the sending end current (I_S) is equal to the receiving end current (I_R). The linear approximation for shorter lines is called the short line model. The per phase equivalent circuit of this model is shown in figure 2.1 [Saadat, 2010].

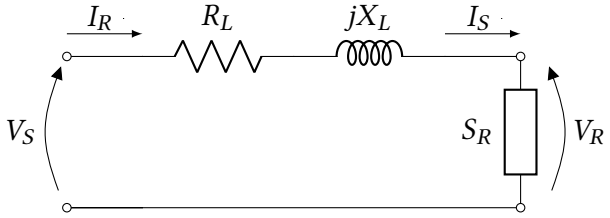

Figure 2.1: Short line model for short to medium range transmission at voltages below 69 kV [Saadat, 2010].

Where V_S and V_R is the sending and receiving end voltage, and R_L and X_L is the lines series resistance and reactance. S_R is the receiving end apparent load power. The reactive flow balance in a line greatly influences the voltage drop over the line. Across the grid, there are sources and sinks of reactive power. Medium voltage lines are sinks of reactive power through their inductance, which causes the current waveform to lag the voltage. This increases the amount of current needed to meet active power demands, due to the resulting flow of reactive power [Masters, 2013].

The voltage regulation of a transmission line defines the voltage drop/rise over a line [Saadat, 2010]. Voltage regulation depends on line impedance and the Power Factor (pf) at loads, which is defined as the ratio between active power consumption and apparent power consumption. The sign of the reactive power consumption defines wether the load has a leading or lagging power factor. If reactive power is consumed at a load, it is said to be inductive and

consumes reactive power. If it injects reactive power into the network, it is capacitive. Inductive loads have a lagging power factor, while capacitive ones have a leading power factor [Masters, 2013]. If a single line is considered, a capacitive load would cause an opposite reactive power flow which will in fact contribute a voltage rise in the line. The current magnitude is however increased, and thus the active power losses suffer from this effect. A lagging and leading power factor is illustrated through the phasor diagrams in figure 2.2

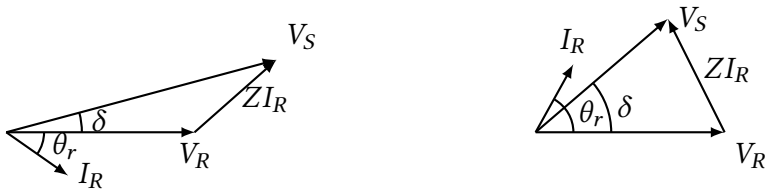

Figure 2.2: Phasor diagram for a lagging pf load (left), and leading pf load (right). Inspired by [Saadat, 2010].

δ is the difference in voltage phase angle from the sending to the receiving end, and θ_R is the angular difference between voltage and current phasors. When the power factor lead/lag leads to unwanted voltage characteristics or unnecessary power losses, compensating measures can be initiated in order to maintain desired voltage. The most typical compensation techniques are [Saadat, 2010]:

- **Shunt Reactor Compensation** - For loads with a leading pf, the voltage increase over the line might become unsatisfactory. In this case shunt reactors are connected at the receiving end of the line. The reactance of the shunt reactor (X_{sh}) compensates for the injected load reactive power, thus improving the pf.

- **Shunt Capacitor Compensation** - When the pf is lagging, the voltage might drop substantially over the line. A shunt capacitor supply reactive power, correcting the load pf. Capacitors can be connected in the tertiary windings of a transformer, or directly to a bus bar. For loads with high penetration of inductive components, the power factor is exposed to fluctuations. In this case the reactive power compensation has to be dynamic, using switchgear controllers. Shunt Capacitor Compensation (SCC) is discussed in greater detail in subsection 2.1.4.

- **Series Capacitor Compensation** - In this case a capacitor is connected in series with the transmission line. The effect is reduced line reactance, which help reduce voltage drops over the line. The contributed production of reactive power from the capacitor depends on line loading, which

exclude the need for a control system. However, the circuit can become resonant with a series capacitor installed. This can lead to oscillations below synchronous frequency during a disturbance, which may damage generators in the system.

2.1.3 Distribution Network Strength

Network strength is an inherent characteristic of any power system. It is a measure of network stability, and affect the magnitude of voltage changes following changes in consumption and generation. Strong networks posses better voltage control in response to disturbances, while low system strength causes increased network voltage volatility during disturbances [AEMO, 2016]. The network strength is usually measured by the available fault current at a node, or the short circuit capacity S_k. The expression for the short circuit capacity is given in (2.7) [Saadat, 2010]. The International Electrotechnical Commission (IEC) standard TR 60725:2012 defines a reference impedance used to test equipment connected to weak networks. This impedance corresponds to a short circuit current (I_{kmin}) of 1.1 kA. A considerable amount of locations in the Norwegian distribution network is reported to have a I_{kmin} lower than this [Seljeseth, 2013]. Thus the problems related to low system strength are very relevant for many Norwegian distribution networks.

$$S_k = \sqrt{3} V_L I_{kmin} \cdot 10^{-3} \text{MVA} \tag{2.7}$$

In (2.7) V_L is the line to line voltage and I_{kmin} is the available fault current. The available fault current vary depending on the network location. Close to synchronous generation, the available fault current is usually higher. In remote locations located far away from generation, the available fault current is lower. This is what causes the system strength to be lower in the outer edges of radial networks without nearby synchronous generation. Since weaker areas in the network are sensitive to fluctuations, distributed and fluctuating generation such as wind and solar can cause increased voltage instability if not controlled.

2.1.4 Optimal Placement and Sizing of Shunt Capacitors

As described, SCC can contribute reduced system losses due to reduced reactive currents. They can also release additional reactive power capacity within the network, and thus improve voltage regulation [Fuchs and Masoum, 2008]. [Fuchs and Masoum, 2008] reports that strategically placed SCC can also reduce total harmonic distortion in the network, and thus increase overall power quality. The allocation problem concerns the number, size and location of capacitors. The benefits associated with SCC implementation are greatly dependent not

only of size and location, but the operational control is also of great importance. The main benefits of SCC are [Fuchs and Masoum, 2008]:

- **Improved voltage profile** - Since SCC reduce reactive currents and improve load pfs, reactive power consumption in the network is reduced. In turn, an improved voltage regulation is obtained. The maximal voltage improvement is obtained by placing the capacitor at feeder endpoints.

- **Reduced active power losses** - If reduction of reactive currents is maintained during most operating conditions, a continuous reduction in current magnitude can be obtained. This results in a reduction of I^2R power losses. If loss reduction is extensive enough, the network operator usually get return on investment. The lowest cost is obtained if capacitors are installed at the high voltage side, due to considerable lower pricing of high voltage units.

- **Released power capacity** - Reduced reactive currents reduce the apparent power flow in the transmission network. As a consequence, greater amounts of active power can be delivered with the same apparent power injection. This means that heavily loaded lines in the network can release some transfer capacity.

Medium to high voltage capacitors are usually built by several one phase capacitor units, connected in parallel to give desired voltage and in series to give the appropriate rating [ABB, 2013].

Placement Strategies During Sinusoidal Operating Conditions

Many methods for optimal placement and sizing of SCC during sinusoidal operation conditions exists. The methods range from simple analytical methods to more complex, computational heavy algorithms. The most basic analytical methods assume uniformly distributed values, such as load and line parameters. One of the early acknowledged methods is the *two thirds rule*, which suggests a capacitor rated two thirds the total reactive power demand located two thirds along the length of the feeder. Later techniques account for variation in load distribution and line parameters, and thus produce better results [Fuchs and Masoum, 2008].

Numerous methods which makes use of more heavy computing exist. These include: numerical programming [Baran and Wu, 1989], heuristic methods [Chis et al., 1997], AI-methods [Miu et al., 1997] and sequential quadratic programming [Abril and Quintero, 2003]. All these methods rely on system parameters such as nodal loads, line parameters, and generation in power

plants. The load flow is calculated, and capacitors are placed in order to minimize an objective function. The objective function typically factors cost and losses, in order to provide the most cost effective solution.

Control of Shunt Capacitors

Capacitors which are not controlled, can yield unwanted effects in distribution networks with high load variability. Unnecessary reactive currents can flow in the network, and unwanted high voltages can occur. With the addition of more complex phenomena within distribution networks, capacitor banks should be controlled in some way. The variable upon which the control is performed is usually either voltage or reactive power flow. In voltage control, the capacitors are operated for certain defined upper and lower voltage limits. If the capacitors have several steps, different limits apply for each step. Reactive power flow control is operated from a similar operational strategy. When the reactive power flow of the line exceeds a certain level, the capacitor is switched. Equivalently, if there is several steps available, each step has a corresponding reactive power limit [Kleinberg and Miu, 2011].

2.1.5 Network Connection of Non-Synchronous Sources

Requirements

Most alternative sources of energy in this thesis is connected to the network through power electronics. When power is injected into the network through power electronics, the power has to be filtered in order to meet network specifications. The parameters of concern are [Kroposki et al., 2006]:

- **Network Frequency** - The nordic power system delivers alternating current at a frequency of 50 Hz. It is important that power is injected at synchronous frequency.

- **Network Voltage** - Voltage has to be injected at the voltage magnitude and phase angle for the given location in the grid. This means that the voltage waveform from the power converter has to be matched with the waveform of the network at the specified location. For larger systems, grid code can require the power plant to keep the voltage at the point of coupling within certain limits. Which is performed by controlling reactive power, this is explained below [Sourkounis and Tourou, 2013].

- **Harmonics** - Power electronics can introduce harmonics in the grid. The amount of harmonic distortion has to be minimized in order to prevent

resonant circuits that may damage equipment and reduce power quality. This is becoming increasingly important with increasing amounts of power electronics in the network. Harmonics is a phenomena that occurs when the injected AC current has a frequency several orders higher, or lower than the nominal grid frequency.

- **Reactive Power Control** - Since power converters have the capability to inject complex power into the network, the power factor has to be controlled to meet the network requirements. If for example a large wind plant connected to a weak network has a specified voltage requirement, it might be required that reactive power injections can be controlled in order to maintain voltage [Sourkounis and Tourou, 2013].

- **DC-AC conversion** - Sources such as Photovoltaic (PV) power plants and battery energy storage deliver direct currents. DC power has to be converted into three phase AC power in order to be injected into the network. The quality of injections has to meet all requirements listed above.

- **Safety** - Systems connected through inverters should have a safety system that disconnect the system in case of severe faults or maintenance. However, the requirements for operation during faults has become increasingly relevant for larger non-synchronous systems [Tande et al., 2007].

Complications

Grid connected non-dispatchable distributed generation, can cause challenges related to stable network operation. The fluctuating injections from a distributed power plant can cause changes in voltage, which exceeds the regulated limits (see subsection 2.1.6). If distributed generation is connected to the distribution network, it has to be assessed whether the network is strong enough to coupe with the possible variations in power injections from the unit. This is necessary to control, as overvoltages can cause unwanted stress on system components, which in turn can cause damage and reduce system lifetime. If bottlenecks are present in the network, large injections from distributed generation can also cause high loading in power lines, which also contributes to reduced system lifetime. Again, these problems introduce the need for active systems for control of reactive and active power flow in the network [Tønne et al., 2014].

2.1.6 Norwegian Power Quality Regulations

In the Norwegian power system, the power quality delivered to customers is regulated by power quality regulations. The regulations are formulated by NVE (Norges Vassdrags og Energidirektorat). Key regulations concerning power quality are [Lovdata, 2019]:

- **Slow variations in voltage magnitude** - Slow variations in the voltage magnitude should be within ±10 % at customers. This value is measured as the average over one minute, in the low voltage point of connection.

- **Overvoltages, undervoltages and voltage changes of low duration** - The amount of occurrences of deviations exceeding 3 % of the stationary voltage or 5 % above the maximal allowed voltage, is regulated to a maximum of 24 per day.

- **Voltage asymmetry** - The asymmetry between phases in the network should not exceed 2 % on average over a period of 10 minutes.

2.2 Solar Power

2.2.1 Properties of Sunlight

The total solar radiant flux density at the top of the earths atmosphere, often referred to as the solar constant (S_0), has been estimated to be 1366 ±7 $^{W}/_{m^2}$ based on previously used composite spectrums [Zeqiang et al., 2013]. However a revised value of 1361.1 ±0.5 $^{W}/_{m^2}$ has been quantified through a recalibration of irradiance data [Gueymard, 2018]. The variations in the constant is due to sun-earth distance and sun activity perturbations.

As sunlight travels through the atmosphere, a number of phenomena lowers the intensity of solar radiation. Some wavelengths in solar radiation is absorbed by gas molecules in the atmosphere, changing the spectral content of the radiation, but even though these make troughs in the radiation spectrum, they do not have a huge impact on the available power. The vast majority of the atmospherical power losses are due to absorption and scattering by air molecules and dust. The extent of the absorption is dependent on the path length, or Air Mass (AM), which varies with the suns position relative to the surface [Honsberg and Bowden, 2015].

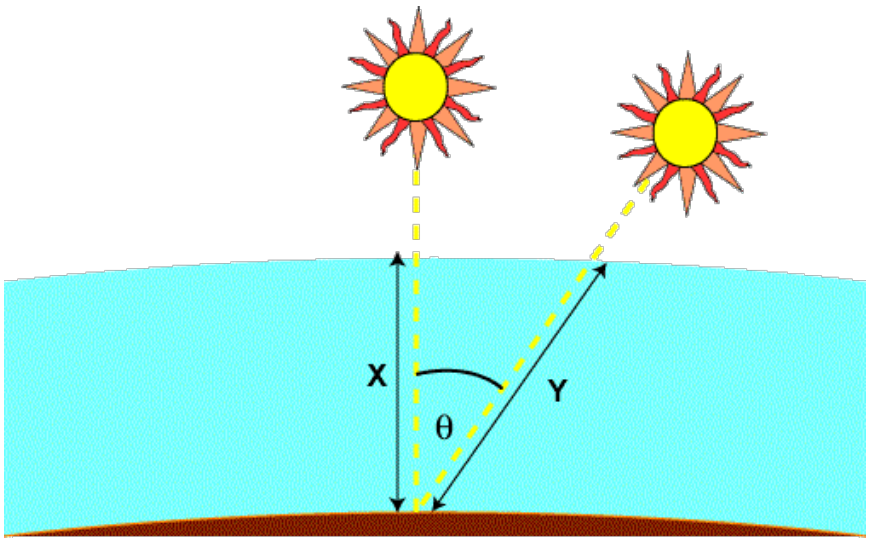

Figure 2.3: Calculation of Air Mass, from [Honsberg and Bowden, 2015].

In figure 2.3, the calculation of AM based on the zenith angle is shown. The zenith angle θ_z is the angle between the suns position and the vertical,

and calculation of AM is given by equation 2.8.

$$AM = \frac{1}{\cos(\theta_z)} \tag{2.8}$$

As mentioned, scattering plays a vital role in reducing the irradiance incident on the earths surface. This phenomena occurs when the electromagnetic field of photons hit the electric field of atmospheric particles such as molecules, dust and clouds. The scattering of radiation implies that some radiation is lost as it is scattered away from the earths surface, hence the irradiance intensity is reduced. Shorter wavelengths such as blue light are scattered in a process known as *Rayleigh scattering*, where smaller gas molecules scatter the radiation. Scattering by air molecules and dust, is known as *Mie scattering*. The amount of scattering is dependent on air mass, and atmospheric content [Lopes and Fernandes, 2014].

The result of atmospheric scattering, is the distinction between two types of solar irradiance incident on the earths surface. The total irradiance on a horizontal surface is referred to as the Global Horizontal Irradiance (GHI), and is composed of *direct irradiance* (I_{DN}) and *diffuse irradiance* (I_{DIF}) [Masters, 2013].

$$I_{GH} = I_{DN} \cdot \cos(\theta_z) + I_{DIF} \tag{2.9}$$

Where I_{GH} is the GHI. Direct irradiance reaches the surface without being scattered, while the diffuse fraction is scattered. Scattered light is often assumed to be undirected, implying that it appears isotropic, which means that it has the same intensity in all directions. *Reflected irradiance* can be seen upon as a third component of solar radiation, as some of the irradiance incident on the earths surface is reflected. Reflected irradiance does not affect I_{GH}, and is dependent on the surface tilt angle (β) and ground reflectance (ρ_r). The reflected irradiance (I_{RC}) incident on a collector surface is given as [Masters, 2013]:

$$I_{RC} = I_{GH}\rho_r \left(\frac{1 - \cos\beta}{2}\right) \tag{2.10}$$

It has been performed several studies on typical ground reflectance for different surfaces [Rana, 2012, Bourne, 2017]. Typical values for summer surfaces is in the range of 0-25 %, while fresh and old snow is reported to be in the range of 50-95 %.

2.2.2 The Solar Path

As the earth rotates around its own axis, the time of day changes. In terms of the solar resource, it is important to distinguish between the Local Time (LT) and the Local Solar Time (LST). The LST noon is when the sun is at its highest above the horizon, while the LT noon is at 12 o'clock. These variables often differ from one another because of the longitudinal differences within a time zone, as well as the eccentricity of the earths orbit, [Honsberg and Bowden, 2015]. Certain reference points are used for every timezone, these are called the Local Standard Time Meridian (LSTM). The LSTM is given as [Honsberg and Bowden, 2015]:

$$\text{LSTM} = 15^\circ \cdot \Delta T_{UTC} \tag{2.11}$$

Where ΔT_{UTC} is the timezone deviation from Universal Coordinated Time (UTC). LST can be found through the following formula [Honsberg and Bowden, 2015]:

$$\text{LST} = \text{LT} + \frac{\text{TC}}{60} \tag{2.12}$$

Where Time Correction (TC) corrects for longitudinal difference within each timezone, as well as the eccentricity of the earths orbit. The calculation of TC is shown in appendix A. The Sun Hour Angle (HRA) is a measure of time, and measures the angle away from noon at a particular time of day. With the expression for LST we have a way of finding the hour angle at a given location [Honsberg and Bowden, 2015].

$$\text{HRA} = 15^\circ(\text{LST} - 12) \tag{2.13}$$

As the earth orbits the sun, seasonal changes in the earthly tilt relative to the earths orbit plane occurs. This is due to the fact that the earth rotates around its own axis at a tilt of 23.5° relative to the orbit plane [Honsberg and Bowden, 2015]. In order to calculate the irradiance angle relative to the horizon, this angle has to be quantified. This tilt angle relative to the orbit plane is entitled the declination angle (δ) [Honsberg and Bowden, 2015]. The declination angle on the n-th day of the year is given as:

$$\delta = -23.45^\circ \cdot \cos\left(\frac{360}{365} \cdot (n + 10)\right) \tag{2.14}$$

The quantities derived up until this point in this section, enables us to define the two angles that are necessary to describe the solar path.

- **Elavation angle (α)** - The elevation angle describes the angle between sun beam radiation and the horizontal. It is related to the zenith angle as follows $\alpha = 90^\circ - \theta_z$. The elevation angle expression is given in (2.15).

- **Azimuth angle (Φ)** - The azimuth angle describes the compass direction in which the sun beam radiation is shining from. It is given in (2.16).

The elevation angle at a certain time of day, is given in equation 2.15, [Honsberg and Bowden, 2015].

$$\alpha = \sin^{-1}[\sin(\delta)\sin(\phi) + \cos(\delta)\cos(\phi)\cos(\text{HRA})] \tag{2.15}$$

The azimuth angle at any given time is calculated as follows:

$$\Phi = \cos^{-1}\left(\frac{\sin(\delta)\cos(\phi) - \cos(\delta)\sin(\phi)\cos(\text{HRA})}{\cos(\alpha)}\right) \tag{2.16}$$

Where $\Phi = 0^\circ$ equates to sunlight coming from the North.

2.2.3 Photovoltaic Cells

Photovoltaic Cells or PV cells convert the energy in solar irradiance into electricity. A PV-cell is made from semiconductors, which is a material which only conducts when electrons are excited to the conduction band. This demands a certain energy, which is dependent on the atomic characteristics of the material. When electrons are excited into the conduction band, they leave a *hole*. Electrons in the conduction band and holes that arise are referred to as *carriers*, and they participate in conduction within the material [Masters, 2013].

Carrier concentration is entitled *intrinsic carrier concentration*, and is dependent on material properties and temperature [Honsberg and Bowden, 2015]. The concentration of electrons and holes can be altered through a process called doping. Silicon, which is the most widely used material for PV applications, is a semiconductor in group IV in the periodic table. If impurities in the form of group V materials is added, the semiconductor becomes n-doped, meaning that electrons are the *majority carriers*. The opposite effect where holes are majority carriers can be obtained by doping silicone with group III materials, giving a p-doped material. If a n- and p-doped semiconductor is combined, it creates a p-n junction, which form the basis for electricity productions in solar

cells [Masters, 2013].

In a p-n junction an electric field from the n- to the p-side is formed due to the formation of immobile charge carriers in the junction. The electric field creates a *depletion region*, where mobile carriers are not able to flow, as it pushes mobile positive carriers towards the p-region, and vise-versa for negative carriers. If the cell is irradiated by the sun, mobile electron-hole pairs appear in the material. If these reach the vicinity of the p-n junction, the hole will be pushed into the p-region and the electron into the n-region, inducing a potential that can be used to deliver power to a load [Andrews and Jelly, 2017].

The equivalent circuit for a solar PV cell gives us a basis for describing the current flow through the external circuit of the cell. The most accurate model would include both series (R_s) and shunt resistance (R_{sh}), which alter IV-characteristics [Masters, 2013]. Shunt resistance causes the current to drop by $\frac{V}{R_{sh}}$ at any given voltage, while series resistance causes the voltage to shift to the right by a factor of IR_s at any given current [Honsberg and Bowden, 2015]. To reduce the effects of internal resistance, R_{sh} should be as high as possible, to limit current flow through the alternative path. R_s should be kept as low as possible. The equivalent circuit for a PV cell including both shunt and series resistance is shown in figure 2.4.

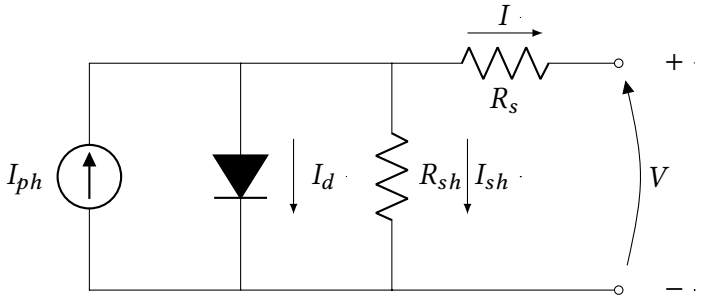

Figure 2.4: Equivalent circuit for a PV cell including series and shunt resistance [Sinha et al., 2014].

In figure 2.4, I_{ph} is the PV current, I_d is the diode current and V is the cell voltage. I, I_{sh} and I_s is the cell current, and current through the shunt and series resistance. The cell current is given as [Honsberg and Bowden, 2015]:

$$I = I_{ph} - I_0(e^{q(V - IR_s/kT} - 1) - \left(\frac{V + IR_s}{R_{sh}}\right) \tag{2.17}$$

Where I_0 is the diode reverse saturation current. q is the electron charge and k the Boltzmann constant. (2.17) can be used to find the short circuit current I_{sc} and open circuit voltage (V_{oc}) of the cell. During short circuit the $V = 0$,

solving (2.17) during these conditions gives I_{sc}, which is the highest obtainable current of the cell. V_{oc} is the highest obtainable voltage, and is found by solving (2.17) for voltage with $I = 0$, which equates to the circuit being open. The IV-dynamics of a solar cell can be summarized in a IV-curve. An ideal cell IV-curve is plotted in figure 2.5.

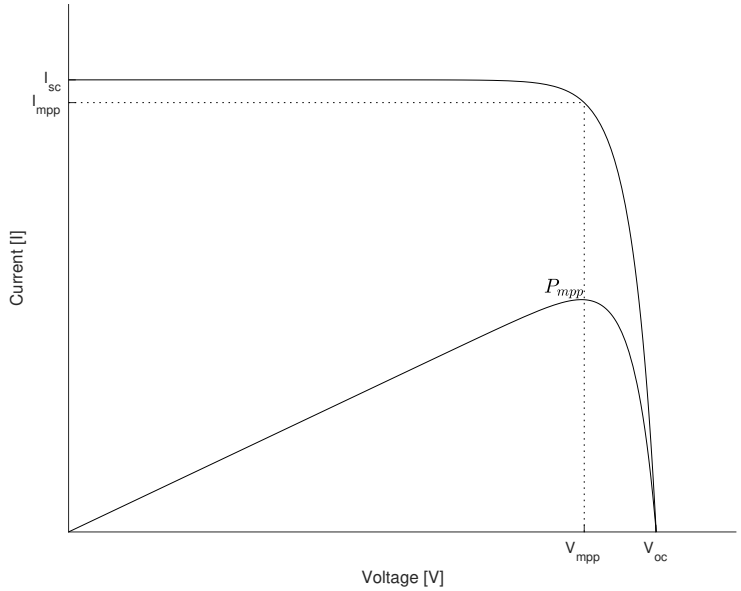

Figure 2.5: Typical IV curve for a PV cell, including the maximal power point.

The power produced by the PV cell is also plotted in figure 2.5. The point where the PV cell has the highest production is referred to as the maximum power point P_{mpp}. The voltage and current of the PV cell during maximum power point operation is known as V_{mpp} and I_{mpp}. Operation at P_{mpp} is essential for obtaining maximum efficiency [Bhatnagar and Nema, 2013].

2.2.4 Photovoltaic Cell Efficiency

The conversion efficiency of a PV cell comes from the relation between maximal power output, and the incident radiant power on the collector. The expression is shown in (2.18), here the incident radiant power is expressed through incident irradiance I_C and the cell area A.

$$\eta = \frac{P_{mpp}}{I_C A} \tag{2.18}$$

The most commonly installed technology in the world today, and the technology most relevant for this thesis, is the single-junction silicon PV cell [Fraunhofer,

2019]. The Shockley-Queisser limit defines the maximal conversion efficiency in single-junction direct bandgap cells. This maximal efficiency is calculated to be 33.16 % for an optimal band gap of 1.32 eV [Rühle, 2016]. A theoretical efficiency of about 29% is reported for silicon, with an indirect band gap of 1.14 eV [Andreani et al., 2019].

The limitations in conversion efficiency comes from several phenomena. All photons with lower energies than the semiconductor band gap, does not manage to excite electrons into the conduction band. These wavelengths are only absorbed as heat. The same goes for the energy levels above the band gap, where the excess energy cannot be converted to useful output. In addition, *carrier recombination* also contributes to lowering the theoretical efficiency [Rühle, 2016, Honsberg and Bowden, 2015].

The highest conversion efficiency in a single junction silicone cell as of March 2019, is 27.4 %. For commercial systems the efficiency is not likely to exceed 25 % [Deign, 2018]. The average efficiency for commercial cells is in the range of 17-21 % [Rühle, 2016]. These rated efficiencies are all obtained during Standard Test Conditions (STC) - that is, 1000 $^{W}/_{m^2}$, AM 1.5 and a cell temperature of 25°C. The power output under STC is referred to the peak power kW_p [Honsberg and Bowden, 2015]. STC does not accurately represent real operating conditions, since the cell temperature often deviates from 25°C. To better estimate the efficiency under real conditions, the Nominal Cell Operating Temperature (NOCT) is often used. NOCT is the temperature of an open circuited cell subject to 800 $^{W}/_{m^2}$ with the air temperature being 20°C [Honsberg and Bowden, 2015].

Due to the reduced efficiency during real operation conditions, a *derating factor* is defined. This describes the actual amount of power produced relative to the theoretical potential during STC. It factors the effect of pollution, shadowing and power losses due to internal and wiring resistance. This value tends to be in the range of 60 - 90 % [Masters, 2013]. Not to be confused with the derating factor is the degradation of a PV cell. This is the reduction of PV cell efficiency with time, as a result of deterioration of the PV cell material. For PV cells the rate of degradation typically ranges from 0.35-1 $^{\%}/_{\text{year}}$, depending on climatological conditions [Ndiaye et al., 2013]. The degradation process is usually slower in colder climates [Jordan et al., 2016].

Cell Temperature Effects on Efficiency

Since PV cells are made from semiconductors, their performance is sensitive to changes in operating temperature. Intrinsic carrier concentration increases with temperature due to a lower band gap, hence the rate of carrier recombination

increases. V_{oc} decreases substantially with increasing temperature due to increasing internal resistance, while I_{sc} only increases slightly due to the reduced band gap. The effect of this shift in IV characteristics is a drop in efficiency. A typical temperature coefficient for silicon PV cells is in the range of -0.4 to -0.5 %/°C [Masters, 2013].

The temperature of a PV cell does not solely depend on the ambient temperature, but it also on the intensity of irradiance. Even though the operating temperature decreases with lower light intensity, the effect of shunt resistance is far greater. As the radiant intensity decreases, the equivalent resistance of the cell approaches that of the shunt resistance. As this happens, the fraction of current that runs through the shunt resistance increases yielding higher losses. The effect on IV characteristics is that I_{sc} is directly proportional to radiant intensity, while V_{oc} decreases following a logarithmic relation. The method used for calculating cell operation temperature in this thesis is shown in Appendix A [Masters, 2013].

2.2.5 Modules and Arrays

A *module* is an encapsulated configuration of series connected cells. The purpose of the rigid encapsulation is to protect the cells against mechanical stress, as well as hindering corrosion in the electrical contacts. Modules come in many configurations and sizes. For grid connected systems, a module typically consist of 60-128 cells. The effect of the series connection of cells, is that the voltage adds. For example, a module consisting of 72 cells with $V_{oc} = 0.6V$ will obtain a module open circuit voltage of 43.2 V [Honsberg and Bowden, 2015].

When several modules are connected together into a larger system, the configuration is entitled an array. For modules connected in series the current remains constant, while the voltage equal the sum of the module voltages. For modules wired in parallel the voltage remain constant, and the current is equal to the sum of the current through each module. An array usually consists of branches of series connected modules, connected in parallel with one another. The series branches build up voltage as much as possible, while parallel branches again increase current to ultimately increase power to the desired specification. This configuration is preferred over strings of parallel connected modules, due to the fact that the outage of one string would not compromise production from the other strings. Larger modules have fewer contacts between them, which reduces line losses, this is an advantage for large PV systems [Masters, 2013, Honsberg and Bowden, 2015].

Shading of Cells and Bypass Diodes

If one cell in a string of cells become shaded, it has a very negative impact on the performance of the string. Shading of a cell is equivalent to the current source in figure 2.4 delivering zero current. If the current carried by unshaded cells in the string exceed I_{sc} of the shaded module, the diode becomes reverse biased carrying zero current, and hence the current has to travel through the parallel and series resistance. This contributes a drop in voltage over the module, drastically reducing power output performance. If the reverse bias in the solar cell become large, the cell can be come extremely hot, which can damage the cell [Honsberg and Bowden, 2015, Masters, 2013].

In recent years the most prominent mitigation measure for dealing with shaded cells has been bypass diodes. Bypass diodes forward bias the current around a shaded cell in the case of reverse bias current, contributing only a small voltage drop over the cell. The most widely used bypass diode is the Schottky diode. A Schottky diode causes a voltage drop of about 0.2-0.6 V [Masters, 2013]. It is possible to mount bypass diodes over every cell, however it is common to bypass groups of cells ranging from 12-24 cells. If one cell in this string gets shaded the entire string is bypassed, while the other strings still deliver power. The number of bypassed cells is chosen based on the breakdown voltage of cells in the string [Goldberg, 2012].

Several manufacturers have in recent years introduced *active* bypass diodes. These are based on fast switching transistors and capacitors. These bypass diodes are basically lossless, as the drop in voltage over such diodes are in the range of 40-50 mV. These devices are typically double the price of conventional diodes, however they offer advantages that can contribute to reduce overall solution cost [Goldberg, 2012].

Due to the drastic effects of module shading, it is important that PV modules are separated by an appropriate distance if several rows are installed. The distance between modules depends on the the size of the panels, panel tilt angle, solar azimuth and elevation angle. The solution can be obtained by applying simple geometry, and is given as follows:

$$d = l \sin \beta \cdot \frac{\cos(\Phi)}{\tan \alpha} \tag{2.19}$$

Where l is the length of the solar panel, and β is the panel slope.

Maximal Power Point Tracking

In order to ensure that PV systems operate at their highest possible power, Maximum Power Point Tracking (MPPT) is essential. Essential for this process is the ability to alter DC voltage, and this is done through a device called *buck-boost converter*. The voltage magnitude is altered to maintain optimal IV characteristics. There exist several algorithms for MPPT, including $^{dP}/_{dI}$ and $^{dP}/_{dV}$ feedback control loops [Masters, 2013]. [Romero-Cadaval et al., 2013] reports that MPPT tracking on module level can increase energy output by 16% compared to tracking on string level. If the tracking is done on cell level the increase can be as much as 30%.

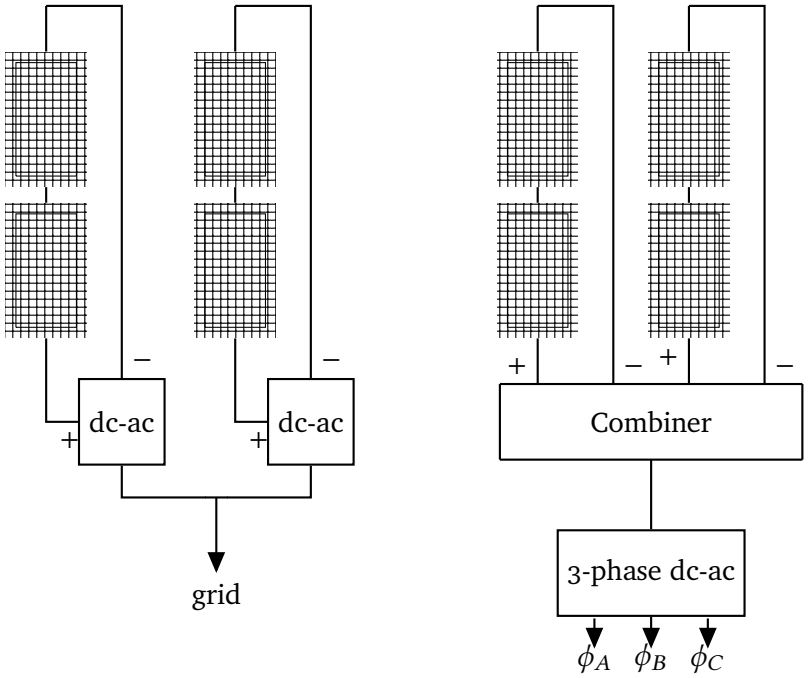

Figure 2.6: Typical array configurations for grid-connected systems. String configuration with one inverter per string (left), and central inverter system with one large inverter for the whole array (right). Inspired by [Masters, 2013].

PV Plant Topology

There exist multiple ways to configure a solar PV plant. Common for all configurations is grid connection through a DC/AC inverters as a consequence of PV systems delivering DC current. Different topologies have different complexity, and in system assessment one has to analyze the cost/yield-ratio of a configuration for a given case. The most common configurations for grid connected systems are [Romero-Cadaval et al., 2013]:

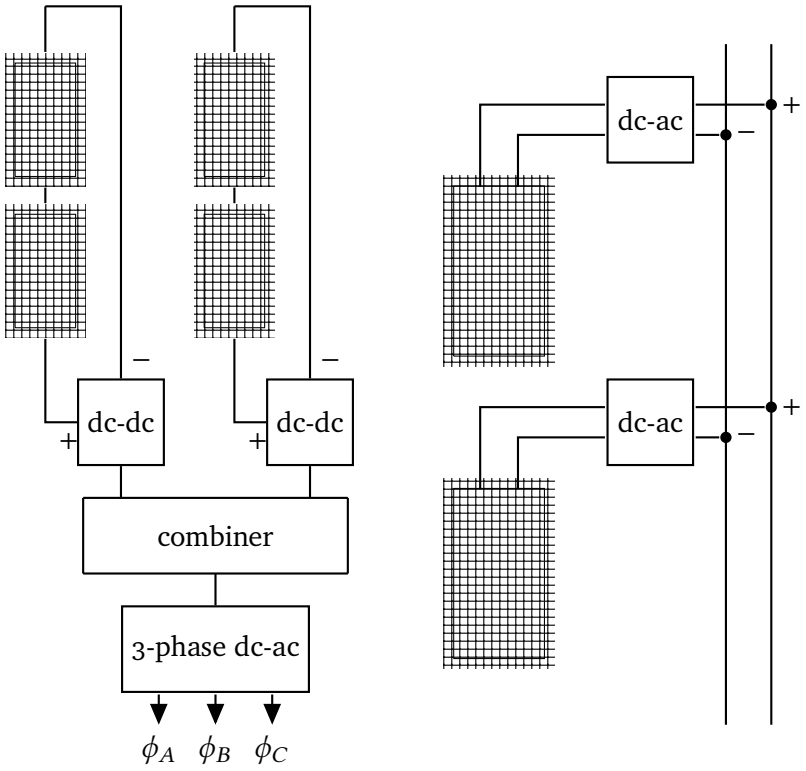

Figure 2.7: Multistring configuration (left). AC module configuration (right), with one MPPT microinverter for each PV module. Inspired by [Masters, 2013] and [Romero-Cadaval et al., 2013].

- **Centralized Configuration** - Centralized configuration is shown in figure 2.6, where $\phi_{A,B,C}$ represents each of the three phases. The power delivered from all stings in the array is combined, and connected to the grid through a three phase inverter. This is a typical design for systems above 10 kW_p.

- **String Configuration** - Similar to the centralized configuration, in this configuration however, each string has an inverter of its own. This topology is shown in figure 2.6.

- **Multistring Configuration** - This is a combination of the two previous configurations. In this case, a buck-boost converter is connected to each string upstream of the combiner, in order to ensure maximum power point operation for each string. As reported previously, this increases output power of the system. The multistring configuration is shown in figure 2.7.

- **AC module configuratuion** - Here each module is connected to the AC bus through a DC/AC inverter of its own, meaning MPPT is performed for each individual module. This yields even higher output compared to MPPT at string level, as discussed. However the costs as well as complexity associated with such systems can become to extensive for larger systems. The AC module configuration is shown in figure 2.7.

2.3 Wind Power

2.3.1 Power in the Wind

If we imagine a parcel of wind of mass m, the kinetic energy in this parcel is determined from the speed at which it travels (v). Thus the kinetic energy of the parcel is given as [Andrews and Jelly, 2017]:

$$E_k = \frac{1}{2}mv^2 \tag{2.20}$$

Power is given as Energy per unit time, and thus the power in the wind can be expressed through the flow rate of mass $\dot{m}$ in $^{kg}/_{s}$. If we define the density of air ρ_{air} in $^{kg}/_{m^3}$, the mass flow rate of air is given as:

$$\dot{m} = \rho_{air} A v \tag{2.21}$$

Where A is the area the wind flows through in m^2 , for example the area swept by wind turbine blades. And v is the speed normal to A the wind flows at in $^{m}/_{s}$. This gives us the final expression for power in the wind [Andrews and Jelly, 2017]:

$$P_w = \frac{1}{2}\rho_{air} A v^3 \tag{2.22}$$

Which is measured in watts. If we divide by the cross sectional area A, we get the *specific power* measured in $^{W}/_{m^2}$. It can be noted that the power available in the wind is dependent on the cube of the wind speed, which in turn means that a doubling of wind speed results in eight times the power.

Logaritmic Wind Profile

In the first few hundred meters above the ground in the lower atmosphere, the wind speed is greatly influenced by the friction from the surface. What this implies, is that an increase in height above ground level can yield substantial increase in wind speeds. One way to describe this increase in wind speed with height, is the logarithmic profile, which can be derived from fluid mechanics [Masters, 2013].

This profile does make some assumptions and simplifications however. The air density is assumed constant with respect to height, in other words the pressure is constant. The pressure gradient is also assumed small. The expression under the given assumptions becomes:

$$\frac{v}{v_0} = \frac{ln\left(\frac{z}{l}\right)}{ln\left(\frac{z_0}{l}\right)} \tag{2.23}$$

Where z is the tower height, and z_0 is the height we have measurements from. l is what is known as the roughness length, which describes the frictional effect of the surface. Some typical roughness lengths are given in table 2.1.

Table 2.1: Typical roughness length for typical terrain types, from [Djohra et al., 2014].

Terrain	l [m]
Very smooth ice	0.00001
Calm open sea	0.0002
Blown Sea	0.0005
Snow Surface	0.003
Fallow field	0.03
Crops	0.05
Few trees	0.1
Forests and woodlands	0.5
Suburbs	1.5

The wind profile for selected roughness lengths is plotted in figure 2.8. The measured wind speed at 10 m above ground in this example is 8 m/s.

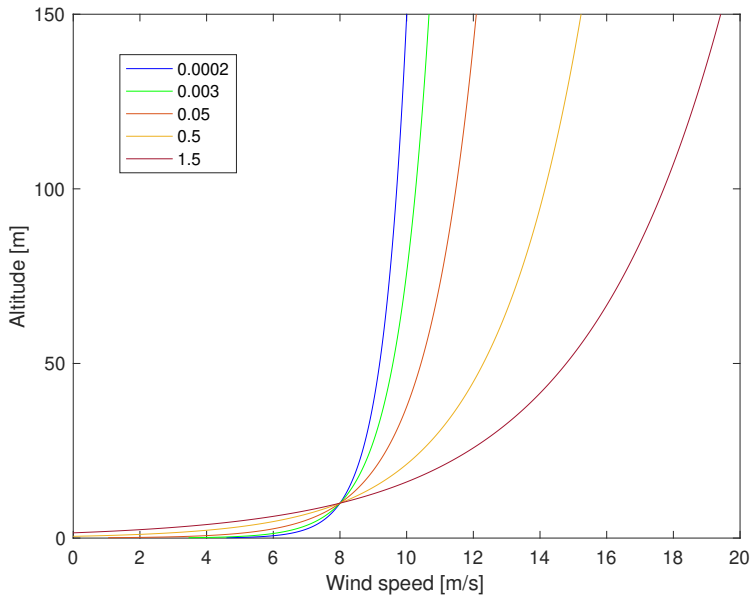

Figure 2.8: Wind speed profile for selected roughness lengths with 8 m/s measured wind speed at 10 m.

2.3.2 Efficiency of Wind Turbines

Betz' Law

The maximum theoretical rotor efficiency that is possible to obtain was derived by Albert Betz, and is known as the Betz limit. The limitations on wind turbine efficiency comes from the fact that in order for it to be flowing air downwind of the turbine, there has to be some kinetic energy that is not extracted by the turbine blades. Some assumptions are made in the derivation - the rotor has an infinite number of blades and they are frictionless. Their flow is incompressible, as well as axial at both sides of the turbine. In addition the thrust is uniform on the rotors [Andrews and Jelly, 2017]. The Betz limit is:

$$\eta_{max,w} = \frac{16}{27} = 59.26\% \tag{2.24}$$

Due to the effects that are neglected in the derivation of Betz' law, the efficiency of real turbines are slightly lower. Modern day turbines can obtain up to 45-50 % efficiency, placing them at about 80 % of the theoretical limit [Masters, 2013].

Tip Speed Ratio

The Tip-Speed Ratio (TSR) is often used as a measure to describe turbine efficiency. The TSR is the ratio of turbine blade tip speed (v_{tip}) relative to upwind wind speed (v_{wind}) [Andrews and Jelly, 2017].

$$TSR = \frac{v_{tip}}{v_{wind}} = \frac{2\pi\omega_t r_b}{v_{wind}} \tag{2.25}$$

Where ω_t is the rotational speed of the turbine blades, and r_b is the blade radius. The efficiency of a wind turbine can be expressed as a function of the TSR, meaning there is an optimal tip speed ratio. Since the wind speed varies, the rotational speed of the turbine also has to vary in order to ensure the correct TSR. Providing this flexibility in rotational speed is the purpose of the variable speed generators discussed in subsection 2.3.5.

Wind Turbine Power Curve

The power output of a turbine is dependent on the wind speed. The power characteristics of a turbine relative to the wind speed is usually summarized in a wind turbine power curve. An ideal version of such a curve created in MATLAB is shown in figure 2.9 [Lydia et al., 2014].

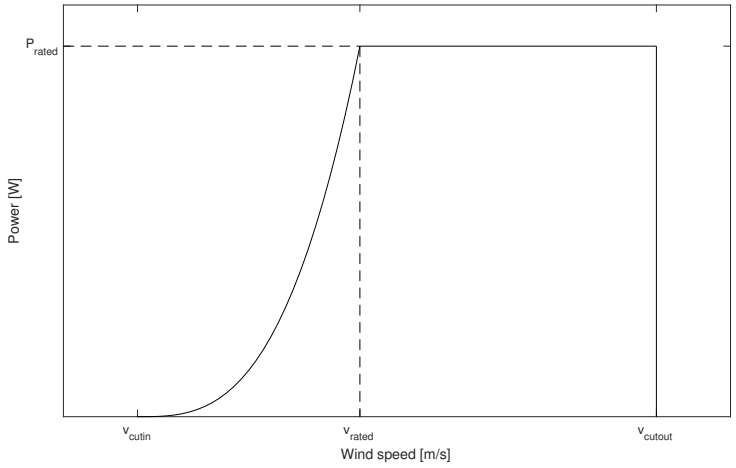

Figure 2.9: Ideal wind turbine power curve, inspired by [Lydia et al., 2014].

The parameters indicated in the figure are important parameters in describing the characteristics of the turbine. The following parameters are defined [Andrews and Jelly, 2017].

- **Cut in wind speed** - The cut in wind speed is the wind speed required for the turbine to start producing power, when winds are lower than this value there is no output.

- **Rated wind speed** - The rated wind speed is the wind speed where the turbine starts producing rated power outputs. Rated power is indicated in the figure. The turbine continue to produce at rated power beyond this wind speed, shedding the excess power through the control regimes described in section 2.3.4.

- **Cut out wind speed** - The cut out wind speed is the wind speed where the turbine stops producing power, due to risk of mechanical damage. Beyond this speed the blades are put parallel to the wind, capturing zero power.

There are two parameters that affect the power curve. Firstly, changing the swept area of the turbine blades will change the rated speed of the turbine. That is, if we assume the same generator being installed in the turbine. A larger swept area would increase power output at any given wind speed, hence reducing the rated speed. Secondly, altering the rated capacity of the generator also has an effect on the power curve. If the generator rating is increased, the rated wind speed would also increase [Masters, 2013]. Altering these parameters enables

construction of turbines that work optimally in different wind conditions. The IEC wind classes define the suitable operating conditions for different turbines. Class I for high winds for sites with 10 m/s annual average wind speed at tower height, class II for 8.5 m/s and class I for 7.5 m/s [Katsigiannis et al., 2013].

2.3.3 Turbine Design

Wind turbines are categorized based on their axis of operation, they are either Horizontal Axis Wind Turbine (HAWT), or Vertical Axis Wind Turbine (VAWT). Since the preferred technology in large scale turbines is horizontal axis orientation, this technology will be discussed in this thesis. Horizontal turbines are categorized based on how they extract power from the wind. They can either be [Andrews and Jelly, 2017]:

- **Downwind Trubines** - The main advantage of downwind turbines is that the wind itself can control the yaw operation, meaning the horizontal orientation. However, the power output and smoothness of operation is compromised due to wind shadowing effects from the tower.

- **Upwind Trubines** - In upwind turbines the rotor blades are facing into the the wind, hence there is no wind shadowing effects present. They do however require some sort of yaw control in order to ensure optimal operating conditions.

All modern large scale HAWTs are upwind turbines, because of their efficient and smooth operation compared to downwind turbines. [Wang et al., 2018b] reports greater fatigue loadings due to shadowing effects from the tower in downwind configurations. In addition, the power output is lower compared to a similar upwind turbine. In modern wind turbines three blades are the preferred quantity of blades, as it shows smoothest operation and efficiency, as well as it is deemed most visually pleasing [Masters, 2013].

2.3.4 Rotor Design and Control

In order to describe how a wind turbine extracts energy from the wind, we have to take a look at how the turbine blades extracts the kinetic energy from the wind. Turbine blades are airfoils, that utilizes Bernoulli's principle to generate lift. Bernoulli's principle states that when the flow rate of a medium increases, the pressure decreases. The streamline traveling above the airfoil at greater speed than the air beneath, results in higher pressure air beneath which in turn causes lift. Since the blades have rotational motion normal to the wind, the

effective wind direction on the blade becomes different than the direction of the wind itself. In order to obtain the correct angle of attack across the blade, it has to be twisted due to the difference in velocity across the blade [Masters, 2013].

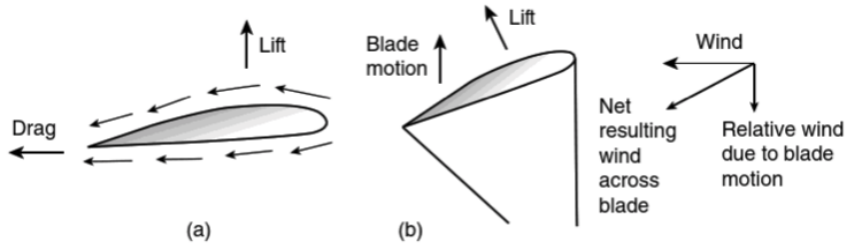

Figure 2.10: Lift in an airfoil with no motion normal to the wind (a), and in a turbine blade with motion [Masters, 2013].

Increasing the angle of attack, increases lift as well as drag up til a point. The phenomena that occurs beyond this point is known as stall. This is the point where the stream of air at the top of the airfoil no longer manages to follow the surface, this causes turbulence that reduces lift.

Since the power from a wind turbine increases cubicly with wind speed, the power can become too extensive for the generator specifications. This introduces the need for control mechanisms to control the turbine output. There are two main approaches to this phenomena, which are *passive control* and *active control*. The passive control scheme utilizes blades designed in a specific way, which causes the blades to stall when the rotational speed of the blades reaches a certain speed. Since the blades stalls, this is often referred to as stall-control [Masters, 2013].

The active control scheme relies on altering the angle of attack of the blades to control generator output, while generator rotational speed is kept constant [Njiri and Söffker, 2016]. This can be done in two ways [Masters, 2013].

- **Active Stall Control** - An active stall control scheme increases the angle of attack in order to induce stall, which in turn reduces the efficiency of the turbine. In this way the turbine output can be controlled.

- **Pitch Controll** - Pitch control utilizes the opposite principle, which is reducing the angle of attack away from the optimal angle. This reduces the lift generated, reducing turbine output. Nearly all large scale turbines utilizes a pitch control scheme.

In both cases an electronic control system monitors the generator output, and alters the pitch of the blades when necessary. With increasing turbine size, the emphasis on control of the structural load on turbine blades has increased. Due to the nonlinear nature of wind flowing through a turbine, the mechanical loading of each blade can vary. Advanced control mechanisms, controlling each blade separately, are introduced in larger turbines to reduce structural load and hence improve durability [Njiri and Söffker, 2016].

2.3.5 Turbine Generator Technology

As mentioned in subsection 2.1.1, power generation has traditionally almost exclusively come from synchronous generators. If a wind turbine uses a synchronous generator, it consequently has to operate at a fixed rotational speed. This is not preferable as it leads to reduced efficiency since the wind turbine would not have the ability to maintain the optimal tip-speed ratio at all wind speeds. In addition, the fluctuations in wind intensity that can be rapid in nature, could be damaging for a synchronous generator as it would not be able to damp these fluctuations in a desirable manner.

Variable Speed Generators

The response to the troubles concerning synchronous generators, is the utilization of variable speed generators. They differ from synchronous generators because they do not rotate at a fixed speed, meaning they are *asynchronous*. Variable speed generators can be either *induction generators*, or they can be synchronous generators where the rotational speed is controlled through power electronics. The main technologies are [Goudarzi and Zhu, 2013, Masters, 2013]:

- **Squirrel Cage induction generators** - The Squirrel Cage Induction Generator (SCIG) has a name inspired by its rotor shape, which lightly resembles a squirrel cage. These generators are the preferred choice for fixed speed stall control wind turbines. This is an inexpensive yet robust technology. The speed variation or the *slip* of the generator is however quite small, typically ±1%, and it is not controllable. SCIG does always consume reactive power.

- **Doubly Fed Induction Generators** - Doubly Fed Induction Generator (DFIG)s needs slip rings and brushes to energize the rotor through a three phase winding, but they do also provide a substantial increase in rotational speed control compared to the SCIG. This technology typically provides 30 % of speed reduction below synchronous speed, and 20 %

increase above synchronous speed. The stator is connected directly to the gird, meaning three phase voltage creates the rotating magnetic field in the stator. The rotor is connected to the gird through power electronics, allowing bidirectional flow. Absorbing power from the grid makes the generator operate sub-synchronous. When the speed is greater than synchronous speed, the rotor delivers power to the grid. One advantage with this technology is that the power electronics need only be rated at 30 % the turbine power. In addition, the reactive power can be controlled through the converter.

- **Permanent Magnet Synchronous Generator** - Synchronous generators can also be controlled using power electronics. They do however require power electronics rated at turbine power ratings. In wind systems, a Permanent Magnet Synchronous Generator (PMSG) is the most prominent synchronous generator technology. It is designed with a high number of poles, enabling elimination of the gearbox. Permanent magnet generators also avoid the complications and maintenance requirements of slip rings and brushes. The increased power electronics rating as well as generator design makes it costly compared to the doubly fed induction generator. However, maintenance costs are much lower.

2.3.6 Wind Turbines and Stable Network Operation

When large fractions of traditional sources of generation is replaced by renewables such as wind, renewables has to perform tasks earlier performed by the traditional sources. With the right control systems, wind power systems can contribute in both regulating network frequency and voltage.

With increasing wind penetration, the ability to contribute in voltage control has become increasingly important. Thus the ability to control reactive power injection/absorption is a feature of increasing interest in wind power systems. The reactive power requirements for a given voltage regulation is greatly dependent on the network impedance phase angle. [Tande et al., 2007] reports that reactive power required to maintain unity voltage in strongly inductive networks is quite low, while being higher for resistive networks. This implies that large scale wind is more suitable in areas of the power system where the network has inductive properties. As described in subsection 2.1.2, high voltage lines are typically more inductive than lower voltage ones.

The reactive power required to maintain unity voltage is also greatly dependent on the size of a wind farm. When installing wind farms in the network, the Short Circuit Ratio (SCR) is often utilized [Tande et al., 2007].

The short circuit ratio is given as $\frac{S_k}{P_r}$, where S_k is the short circuit capacity described in subsection 2.1.3 and P_r is the wind turbine rated power. $\frac{S_k}{P_r} > 25$ is considered as a strong network connection, while $\frac{S_k}{P_r} < 25$ is considered a weak network connection. In weaker networks a larger reactive power capability is often required [Tande et al., 2007].

In some cases where the voltage increments as a consequence of a wind farm are large, the need for continuous reactive power compensation is needed. For larger wind farms this is usually performed by either a Static Var Compensator (SVC), or a Static Synchronus Generator (STATCOM). SVCs is a system consisting of thyristor valve controlled shunt reactors and shunt capacitors (see section 2.1.2). The reactive power absorbed/injected is controlled by a control system in order to maintain stable network operation. A STATCOM uses a Voltage Source Converter (VSC) in order to either consume or provide reactive power, and thus control voltage. Both SVC and STATCOM systems continuously regulate voltage during steady operation, and during faults [Singh et al., 2009, Foster et al., 2006]. In smaller wind systems which utilizes induction generators, and where voltage increments due to wind injections are small, a Power Factor Correcting Capacitor (PFC) can be used in order to compensate the reactive power consumed by the induction generator.

2.4 Energy Storage

With increasing demand, as well as increasing penetration of renewable energy, the relevance of energy storage has increased. The increasing penetration of renewable energy, especially those non-dispatchable in nature, introduces increased fluctuation in power generation. This introduces the need for storage technologies that are able to handle these new demand patterns [Leitermann, 2012]. Implementation of newer storage technologies in the power system such as batteries has increased drastically in recent years, which in turn continues to drive price reduction [Robson and Bonomi, 2018]. Energy storage applications include high power low energy applications such as frequency control, voltage support and renewable smoothing. Applications demanding high energy such as peak shaving and transmission upgrade deferral, is becoming increasingly relevant with the lowering of storage prices [Eller and Gauntlett, 2017] [Gyuk et al., 2014]

In areas of the gird which are subject to constraints on delivered power, higher demand peaks might compromise stable grid operation. The use of Battery Energy Storage System (BESS)s for peak shaving in such conditions could contribute improved power system performance. In many countries

however, regulations and market structure hinders the network operators of utilizing storage for such applications, since storage units are unable to compete in energy Markets [Robson and Bonomi, 2018]. This restricts the implementation of energy storage for this application to network customers. The large investment cost of batteries, and lack of knowledge on the benefits of energy storage, might prevent investments in the technology at industrial customers [Eller and Gauntlett, 2017].

2.4.1 Round Trip Efficiency

Losses as a consequence of loading and utilization of energy storage systems, causes some of the energy to be lost. The efficiency in a full cycle of charging the medium, and discharging it, is referred to as the round-trip efficiency η_{rt} . The round trip efficiency is typically in the range of 60 to 95 % depending on technology, and is given as [Byrne et al., 2018]:

$$\eta_{rt} = \eta_c \cdot \eta_d \tag{2.26}$$

Where η_c and η_d is the charge and discharge efficiency. These losses come from from resistive and reaction losses in electrochemical applications. In mechanical systems the losses are typically thermodynamical or due to friction. Other losses of importance are inverter/rectifier losses or grid components like transmission and transformers. Auxiliary equipment which is required for operation also demand power, and contribute to the overall power balance of the storage medium. Examples of auxiliary services are fans for batteries as well as control systems that manage the unit [Leitermann, 2012].

2.4.2 Prominent Energy Storage Technologies

There are many types of energy storage systems, holding different characteristics. The application of the medium is important when deciding on the preferred technology. The most common technologies today are [Leitermann, 2012]:

- **Pumped Hydroelectric Storage** - The conversion of potential energy into electric power in elevated water reservoirs is explained in section 2.5. In pumped storage, a pumping system that can pump water from the lower reservoir into to the upper reservoir is utilized. The upper reservoir in such systems often have limited inflow of water. One of the main advantages with the technology, is that the energy storage

capacity usually is large, which enables energy to be dispatched with great flexibility.

- **Compressed Air Energy Storage** - This storage technology also feature large energy capacity, and is also based on traditional generation. In compressed air storage natural gas turbines is typically utilized. Air is compressed by a compressor, and stored in a container. The most economic containers are geological features such as underground caves. Since this technology uses conventional generator technology, the response is similar.

- **Electrochemical Storage** - Batteries store energy through chemical processes. Many different chemical configurations can be utilized, with different properties. Some batteries run at elevated temperatures, while some do not. Electrochemical devices are able to respond almost instantaneously, and are often high power low energy as price increases greatly with energy capacity. Batteries will be discussed in more detail in subsection 2.4.3.

- **Flywheels** - Flywheels are a mechanical storage device that stores energy in a rapidly spinning flywheel. For grid connected applications this spinning wheel is typically connected to an electrical machine. The response of flywheels is very rapid, making it useful for frequency regulation.

2.4.3 Electrochemical Energy Storage

As the geographical areas of interest in this thesis does not inherit the possibility of utilizing either pumped hydro or compressed air storage, utilization of BESS will be considered. As mentioned earlier, BESSs are suitable for numerous grid applications, both those demanding high power/low energy as well as high energy. There are many different chemical compositions currently being used for batteries. A selection of relevant chemistries are [Luo et al., 2015, Ierides et al., 2018]:

- **Lithium-Ion** - Lithium-Ion batteries are the most frequently installed technology for large scale grid applications [EIA, 2018]. The technology makes use of a lithium metal oxide cathode, and a porous carbon anode separated by an electrolyte. Alteration of anode and cathode materials, layer properties and electrolyte allows for customization of cell parameters. Some configurations have high energy density and low cycle life, while other have lower energy density and higher cycle life. [Hesse et al., 2017] presents the most common anode-cathode configurations, and their flaws and advantages. Lithium-Ion has the highest electrochemical

efficiency of the presented technologies, which can get as high as 97 %.

- **Lead-Acid** - Consists of lead plates submerged in an acid electrolyte. Due to the fact that lead-acid batteries has been present for so long, they are pretty inexpensive. They do however come with some limitations. Due to their chemical composition, the energy density is pretty low, and hence the batteries are quite large. In addition, the ability to cycle is also inferior to other technologies, as is the round trip efficiency which is in the range of 70-80 %.

- **Sodium-Sulfur** - High temperature battery with molten sulfur and sodium electrodes. The cycle life of this technology is higher than for lead-acid, as is the round trip efficiency which ranges from 75 to 90 %. They do however require substantial cooling systems, and are pricier compared to lead-acid.

Battery cycle life and typical efficiency for different technologies is summarized in table 2.2.

Table 2.2: Typical efficiency and cycle life for different battery technologies [Luo et al., 2015]

Chemistry	η_{rt} [% dc-dc]	Cycle Life [% DoD]
Lithium-Ion	80-97	1,000 - 10,000
Lead-Acid	70-80	500-1,800
Sodium-Sulfur	75-90	2,500 - 4,500

Key Battery Parameters

Several parameters are important for the performance of a battery system. The parameters relevant to the applications discussed in this thesis are [MIT, 2008]:

- **State of Charge (%)** - The SoC is the relation between present capacity and maximal capacity.

- **Depth of Discharge (%)** - The DoD is defined as the amount of capacity utilized in a discharge. For example, if the battery is emptied, the DoD is 100 %.

- **Nominal Energy(Wh)** - Describes the energy capacity of a battery.

- **Energy Density (Wh/kg)** - Describes the stored energy per kg of battery.

2.4.4 Electrochemical Storage Application Schemes

With increasing penetration of renewable energy technologies, power fluctuations will occur to a larger extent. As mentioned, batteries have the ability to act rapidly to such fluctuations which makes them suitable. By damping rapid power ramp rates, the stress on the network will be reduced, and at the same time network performance will increase. Damping of renewable power ramp rates might be essential for renewable applications in weak networks [Ertugrul, 2016].

Peak load shaving in large industrial establishments in the distribution network can also contribute a more satisfactory power network operation. Traditionally, peak shaving has been performed through linear programming methods, where the rate of return is weighted [Youn and Cho, 2009]. Other approaches such as nonlinear programming and dynamic programming has also been formulated [Weihao Hu et al., 2010, Riffonneau et al., 2011]. Later techniques have been formulated, which are not so heavy to compute. The algorithm proposed by [Rahimi et al., 2013] calculates the battery utilization based on the floating mean load profile.

2.5 Hydroelectric Power

When water is stored in a reservoir, the water holds potential energy. Hydroelectric power plants seek to transfer this energy into useful electric power. A typical schematic view of a Hydroelectric Power Plant is shown in figure 2.11.

The device that transforms the mechanical energy of a hydro turbine into electric power is the synchronous generator which is described in section 2.1.1. Due to the large amounts of energy typically contained in reservoirs, hydro plants can provide responses to load changes for long durations. Electricity produced from a hydro plant is usually quite cheap, the value depends on the *water value*. The water value describes the current value of the water, and is dependent on inflow characteristics as well as reservoir level [Wolfgang et al., 2009]. Plant owners often base their production on economical considerations. In other words electricity is being produced when it gives the highest revenue.

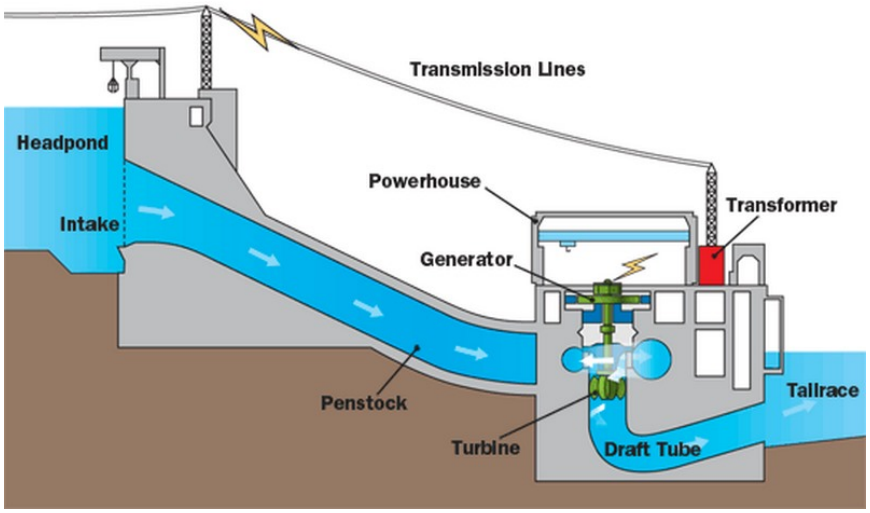

Figure 2.11: Schematic view of a typical Hydroelectric Power Plant, from north-harris.org

2.5.1 Power Output from a Dam

The power output from a dam is dependent on several parameters. The distance from the upper reservoir to the turbine is referred to as the *head* of the dam, which is measured in meters. This parameter does not only relate to the power output, but is also important when choosing turbine design. For low/medium head dams, reaction turbines such as Francis or Kaplan turbines are utilized. Due to the low head, these turbines are required to be large, as they demand large volume flow rates, and they typically spin slowly. When operating such power plants, the water runs through the *penstock* towards the turbine. The turbine blades are completely submerged in water as the water passes through, converting kinetic energy into mechanical energy in causing the turbine to spin. For dams that have a large head, an impulse turbine such as the Pelton turbine is utilized. In Pelton turbines, the water is converted into high speed jets which are fired at bowl-shaped blades [Andrews and Jelly, 2017].

The total power output depend on the volume flow rate of water Q, in $^{m^3}/_{s}$, since it describes the amount of water that is fed into the turbine per unit time. The potential energy of the water that is fed in from the reservoir can be described using the head h, $E_p = \rho_w g h$. Here ρ_w is the density of water in $^{kg}/_{m^2}$. Using the above, the power production can be described. However, one also need to factor in losses. As the water travels through the penstock, as well as upon interacting with the turbine, some power losses occur in the form of friction and turbulence. The conversion between mechanical power and electrical power does also include some losses, however they are very insignificant. The effect of total losses can be described in the total conversion

efficiency η_h which is typically around 90 % for hydro plants [Andrews and Jelly, 2017]. Thus, the total produced power becomes:

$$P = \eta \rho_w g h Q \tag{2.27}$$

2.5.2 Controlling the Power Output

The power output can as mentioned be decided based on maximizing profits, but can also be decided based on network stability requirements. The power in a hydro plant is regulated through a governor system which controls a gate at the intake. The position of this gate is altered in order to control the volume flow rate, which in turn controls the power production. There is also control systems in the turbines themselves to alter power. For reaction turbines the blade positions are altered, to alter rotational speed. In impulse turbines, valves can alter their position in order to alter the rotational speed of the turbines. All this regulation is done by governors which continuously monitors parameters such as frequency, and voltage waveforms [Andrews and Jelly, 2017,Machowski, 2008].

2.6 Statistical Analysis

In order to validate a simulated dataset, and compare it to real measurements, a statistical analysis might be conducted. For a set of random data, the mean value is given as [Knight, 2000].

$$\overline{x} = \frac{1}{n} \sum_{i=1}^{n} x_i \tag{2.28}$$

And the variation of the dataset, called the variance can be calculated as [Knight, 2000]:

$$\sigma^2 = \frac{1}{n-1} \sum_{i=1}^{n} (x_i - \overline{x})^2 \tag{2.29}$$

From the variance one can find the standard deviation, which is the square root of the variance. This is a measure of the spread of samples. In other words a low σ shows low variations in the dataset, while a high value suggests high spread.

2.6.1 Pearson Correlation Coefficient

In order to investigate the correlation between two datasets, one can calculate a correlation coefficient. The most common calculation to conduct, is the

calculation of the Pearson correlation coefficient. For a estimated set of values x_i and a measured set of values y_i it is given as [Disha, 2018]:

$$r = \frac{\sum_{i=1}^{n}(x_i - \overline{x})(y_i - \overline{y})}{\sigma_x \cdot \sigma_y} \tag{2.30}$$

This coefficient has a value between -1 and 1. Where 1 indicates exact positive correlation, 0 indicates no correlation and -1 exact negative correlation. Interpretation of the pearson correlation coefficient is summarized in table 2.3 [Disha, 2018].

Table 2.3: Interpretation of the Pearson Correlation Coefficient

Size of Correlation	Interpretation
± 1	Perfect Positive/Negative Correlation
$\pm(0.90 - 0.99)$	Very High Positive/Negative Correlation
$\pm(0.70 - 0.90)$	High Positive/Negative Correlation
$\pm(0.50 - 0.70)$	Moderate Positive/Negative Correlation
$\pm(0.30 - 0.50)$	Low Positive/Negative Correlation
$\pm(0.10 - 0.30)$	Very Low Positive/Negative Correlation
$\pm(0 - 0.10)$	Negligible Positive/Negative Correlation

2.6.2 Bias

In order to evaluate whether a simulated dataset over or underestimates a variable, one can calculate the bias. The bias is given as [Knight, 2000]:

$$\text{bias} = \frac{1}{n}\sum_{i=1}^{n}(x_i - y_i) \tag{2.31}$$

Where x_i is the simulated values and y_i are the measured values. If the bias is negative, the tendency is that the simulated values underestimates the variable. The opposite is concluded for a positive bias.

/3 Location

Senja is located at about 69 ° north along the coast in Troms, Norway. Senja is an island know for its mountainous terrain, and for its coastal communities harvesting the great seafood resources in the area.

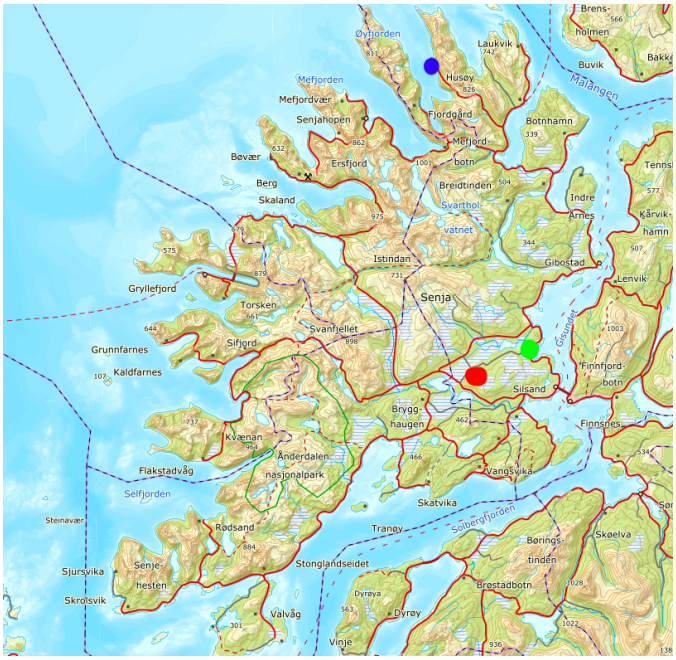

Figure 3.1: Map of Senja from Norgeskart, [Norgeskart, 2019b]

Long distances between supply and demand of power, makes the power infrastructure vulnerable with increasing demand. This is the problem which this thesis is based upon, and which the work presented seeks to find solutions to. Analysis of network performance is performed for two areas. The first is the voltage regulation performance in the radial distribution network supplying Husøy. The second is the loading of the main supply line to the island with increased industrial loading, which is evaluated in context of a new industrial establishment at Silsand. Husøy and Silsand is marked in figure 3.1 by a blue and green dot respectively. The red dot shows the location of the wind power plant considered in this thesis.

3.1 Surface Conditions

Since the island is located at nearly 70° N, the ground is covered by snow for long periods of time. Figure 3.2 shows a map of the snow cover conditions at the island in terms of days with snow cover above 5 cm, averaged from year 1971 up til 2000 [Norge, 2018].

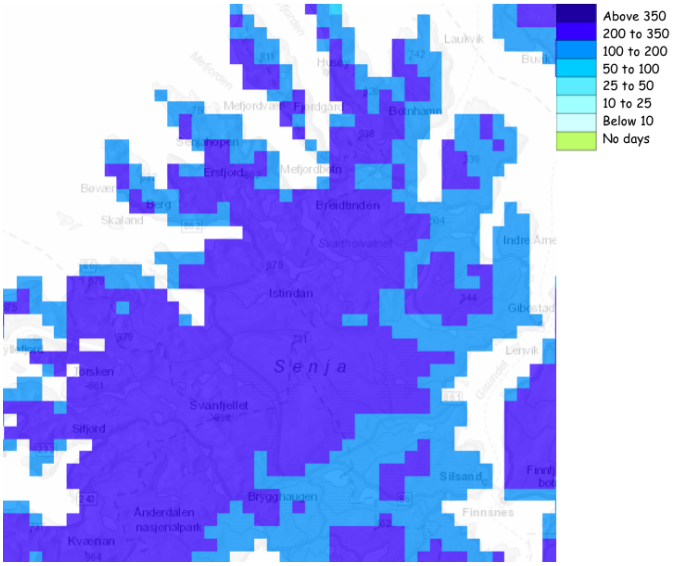

Figure 3.2: Days during a year with snow cover deeper than 5 cm, 1971-2000, from senorge

As one can see from the figure, the typical number of days is between 100 and 200 days a year for the areas at sea-level. Implying that snow can be present even in the early spring, which can have a positive impact on solar power production due to surface albedo [Masters, 2013].

As for the surface conditions and vegetation during times of the year with no snow cover, the types of topography is shown in figure 3.3. The map is from Norgeskart, using the overlay corine landcover [Norgeskart, 2019a]. It can be seen that the island has vast areas of forest, as well as areas of peat bog wetlands at the eastern side. Heath and moors and sparse vegetation dominate at the slightly higher elevations, and bare rock dominates in the mountains.

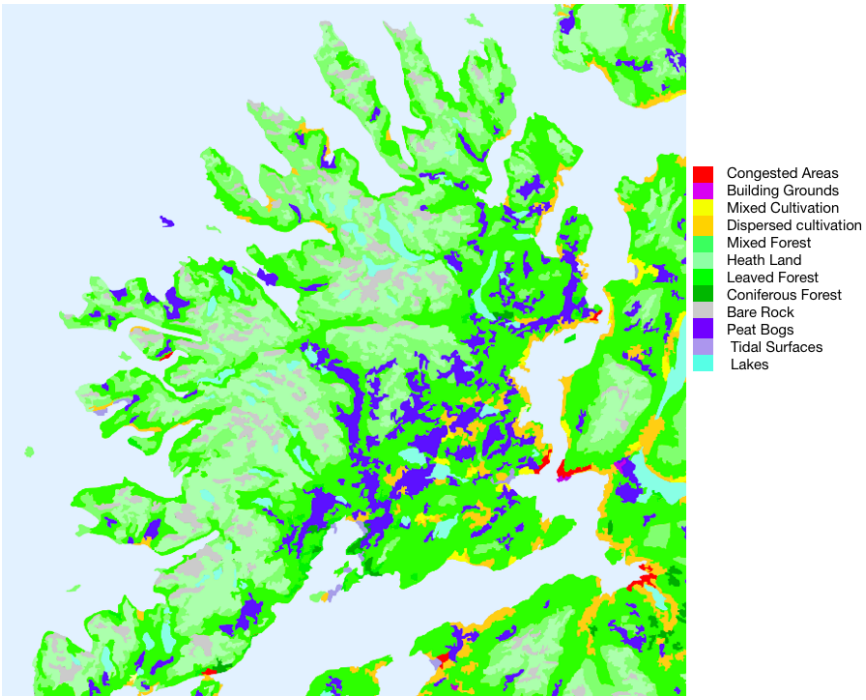

Figure 3.3: Vegetation and Surface conditions at Senja, [Norgeskart, 2019a]

3.2 Existing Power Plants

Today there are three hydro power plants at Senja. Two of them, Lysbotn and Bergsbotn are located at northern Senja, while a smaller power plant Osteren is located further south. The location of these power plants is shown in figure 3.4.

These power plants utilizes optimal economical dispatch. Meaning that they produce power when the highest profit is obtainable. All three power plants are small/medium scale plants, and the characteristics of the power plants are [NVE, 2019, TKN, 2019]:

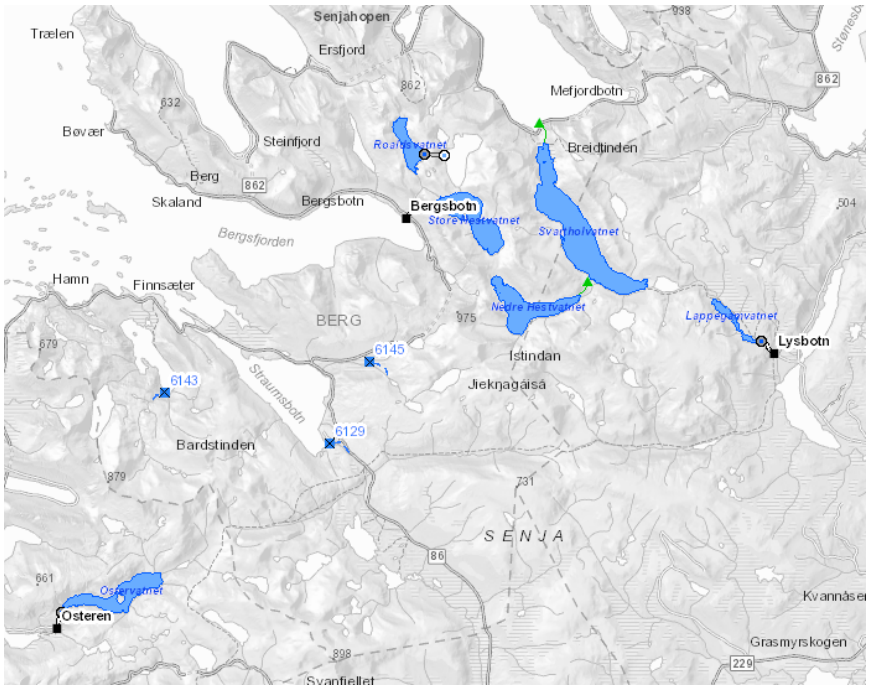

Figure 3.4: Map showing the hydro power plants at Senja and their reservoirs [NVE, 2019]

- **Lysbotn** - Lysbotn is a medium head power plant with a head of 106 m. The power plants' main reservoirs are *Svartholvatnet* and *Nedre Hestvatnet* with a combined reservoir volume of 38.4 Mm^3. The turbine generator has a rating of 6.3 MVA. In 2018 the total production from Lysbotn was 25.7 GWh.

- **Bergsbotn** - Bergsbotn is a high head power plant, the head being 354 m. The plant is supplied from the reservoirs *Store Hestvatnet* and *Roaldsvatnet* with a combined reservoir volume of 25.8 Mm^3. The peak apparent power output is 10 MVA. In 2018 the total production was 28.3 GWh

- **Osteren** - Osteren is a medium head power plant with a head of 136 m. *Ostervatnet* is the main reservoir, with a reservoir volume of 5.4 Mm^3. The peak apparent power output is 3.15 MVA. In 2018 the total production amounted to 13.1 GWh.

As mentioned, these power plants are operated from a perspective of maximal profit. For Husøy, power injection and correction from Lysbotn plays a vital role in maintaining desirable voltage regulation during heavy load periods. If the plants was run exclusively from a stability point of view, adequate voltage regulation might be possible even with increasing load patterns. This will be

discussed further in section 4.4.3.

3.3 Existing Network

The basic outline of the Norwegian power system is presented in subsection 2.1.2. The distribution network at Senja is supplied by a 66 kV regional network line from Finnfjordbotn. Three substations at the island steps down the voltage for distribution. These are located at Silsand, Svanelvmoen and Bergsbotn. The network at Senja is shown in figure 3.5, where all substations are indicated by red squares.

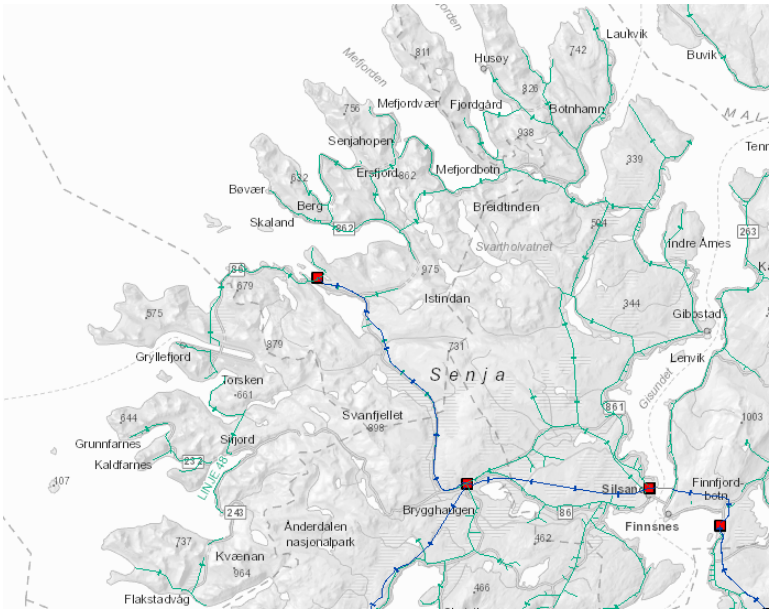

Figure 3.5: The topology of the electrical power network at Senja, from [NVE, 2019]

The regional network transmission line which is the source of regional network injections, is nearing its capacity [TKN, 2018]. With known planed industrial establishments, as well as regular demand increase, it is reported that a reduction of 5 MW peak load power referred to prognoses is needed in order to postpone a line upgrade 5 years. If the line is upgraded, it will be operated at 132 kV. From figure 3.5 it is evident that the distribution network spans over long distances, this is of concern due to increasing demand as this can compromise power quality. *Troms Kraft* processes a concession on a possible new 132 kV regional power supplying northern Senja. Alternatively the distribution network has to be upgraded [TKN, 2018].

4

Data and Methods

4.1 Weather Resource Data

4.1.1 Solar Resource Data

Measured Data

As a part of the *Smart Infrastructure Northern Senja* project, a pyranometer has been installed at Silsand. The pyranometer measures GHI, and has been outputting measurements since late 2018. The pyranometer is an Apogee SP-510s, which is a thermopile pyranometer. Thermopile pyranometers are known for great accuracy, and the SP-510s is reported to have a measurement insecurity of ± 5 % [Apogee, 2018]. The pyranometer is mounted at the top of a roof structure, and is not shaded by surrounding objects. Figure 4.1 shows the 24-hour averaged measurements from the period January 1st to April 31st 2019.

In order to perform yearly analyses, yearly data is needed. Thus, in this thesis simulated data is utilized. The simulated data is assessed through a statistical analysis comparing it to data from an existing measuring station. A Kipp and Zohen thermophile pyranometer owned by *Bioforsk*, located at Holt weather station is used for this purpose [Bioforsk, 2018]. The annual energy potential sums to 733.6 $^{kWh}/_{m^2}$, which equates to a daily average of 2.01 $^{kWh}/_{m^2}$.

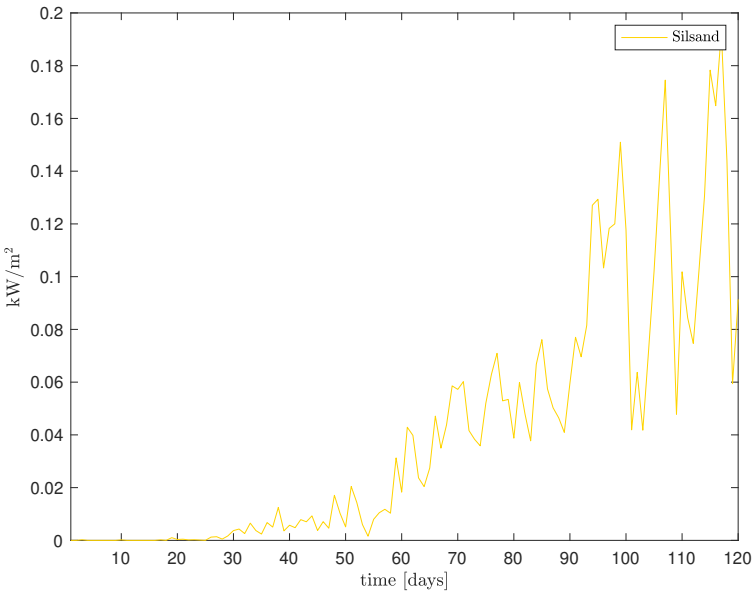

Figure 4.1: 24-hour averaged global horizontal irradiance at Silsand the four first months of 2019

ERA 5

Since there is no measured yearly data for Silsand, which is the solar assessment location in this thesis, simulated data is used. In this thesis the ERA-5 reanalysis dataset is used. The dataset is developed by the European Centre for Medium-Range Weather Forecasts (ECMWF). ERA-5 provides hourly forecast fields and analyses. To estimate the state of the atmosphere, ERA 5 assimilates data from available sources such as satellite data and local observations. The data is processed numerically through ERA-5's Integrated Forecasting System (IFS) [Wang et al., 2018a]. The resolution of 31 km is interpolated to 1 km. The accuracy of the simulated data will be evaluated using the Pearsson correlation coefficient and the bias (see section 2.6). The simulated yearly profile for 2017 is shown in figure 4.2.

The figure shows the 24 hour averaged values for Silsand in 2017. The total energy for 2017 amounts to 786.8 $^{kWh}/_{m^2}$ which equates to a daily yearly average of 2.16 $^{kWh}/_{m^2}$. In order to perform the statistical analysis, simulated data was also retrieved for Holt weather station in Tromsø. ERA 5 simulated a total yearly global horizontal energy potential of 760.5 $^{kWh}/_{m^2}$ at Holt weather station in 2017. This equates to a daily average of 2.08 $^{kWh}/_{m^2}$.

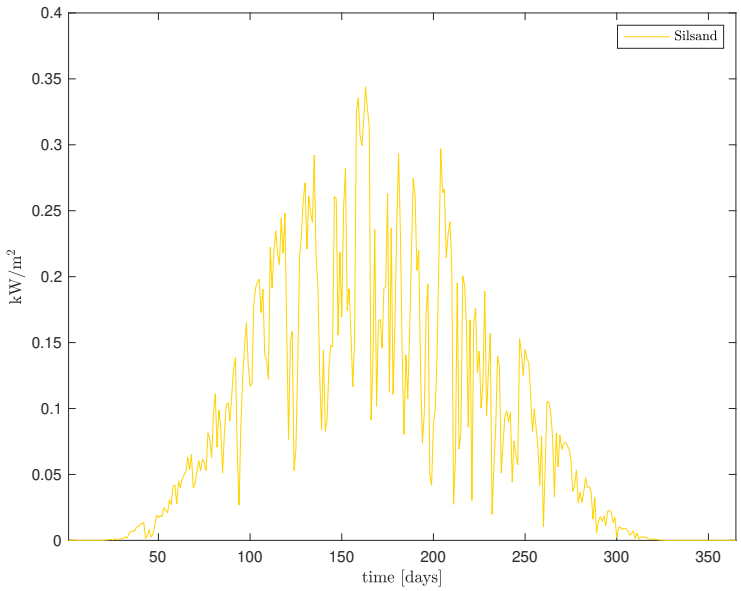

Figure 4.2: 24-hour averaged global horizontal irradiance for Silsand. The data is simulated values from the ERA 5 reanalysis dataset.

4.1.2 WRF Wind Data

As there was no available measured wind data for the location, simulated data from the Weather Research and Forecasting Model (WRF) was used. The WRF model is a forecast and assimilation system that makes use of advanced numeric methods to calculate the solution for each time step. First, the model initialize by pulling geographical information such as topography as well as assimilating data from various sources such as land measurements and satellites. The dynamic solver then calculate the solution for each time step [Powers et al., 2017].

The considered location for wind power in this study is mountainous terrain slightly west of Silsand, the location is shown in figure 3.1. The data outputs as north-south, east-west and vertical components of wind in 10 minute resolution. The data has a spacial resolution of 1 km. Effects of vertical winds will be neglected in this study, thus only the horizontal components was considered. The magnitude of wind speed was calculated from the two horizontal components. In figure 4.3 the 24-hour averaged wind speed for 2017 is shown. The average simulated wind speed over the course of 2017 is calculated to be 5.35 m/s.

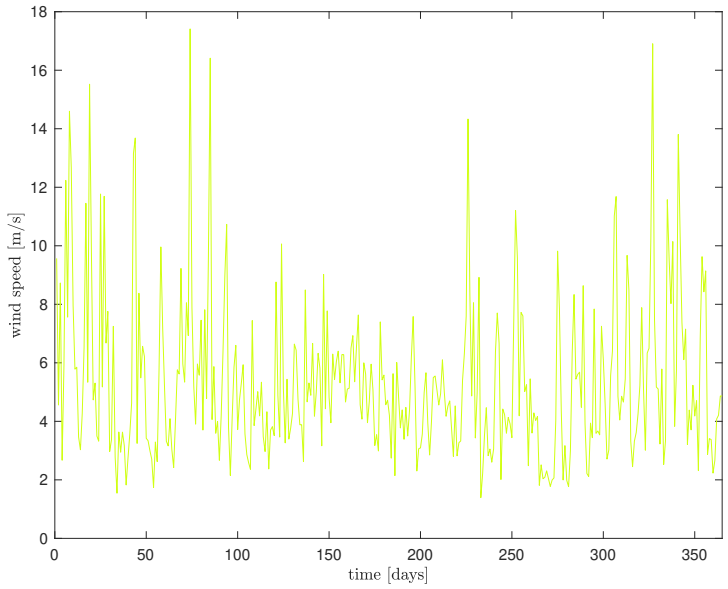

Figure 4.3: 24-hour averaged wind speed for the wind location in 2017. The data are averaged over 24 hours to show the general wind speed tendency.

4.1.3 Temperature Data

In order to find relevant temperature data, the Norwegian Meteorological Institutes data services was searched. It was not found any official weather station in the vicinity of the locations in this study that had hourly values, which are required for simulations. Thus, the temperatures used for estimation of PV temperature effects was retrieved through the simulation software HOMER's database. These values are monthly averages, and the insecurities this poor resolution creates must be kept in mind. The monthly average temperatures used in calculations are shown in table 4.1. HOMER states that the temperature is an average of observation between 1980 and 2005. The data was compared to the monthly averages of the nearest official weather station, which is located at the northern edge of Senja. It was found that the normal yearly average temperature there was 4.0°C, while the HOMER data has an annual average of 1.9 °C [eKlima, 2019]. The uncertainty of the temperature data must also be kept in mind when evaluating simulation results.

Table 4.1: Monthly averaged temperatures used in simulations, the yearly annual temperature amounts to 1.9°C.

Month	Daily average temperature [°C]
January	-5.1
February	-5.1
March	-3.6
April	-0.6
May	3.7
June	8.8
July	11.5
August	10.6
September	6.8
October	2.2
November	-2.0
December	-4.1

4.2 Existing Production and Load Data

4.2.1 Hydro Production at Senja

Troms Kraft has provided production data for the hydro power plants at Senja in 2018. The 24-hour averaged production from the power plants is shown in figure 4.4.

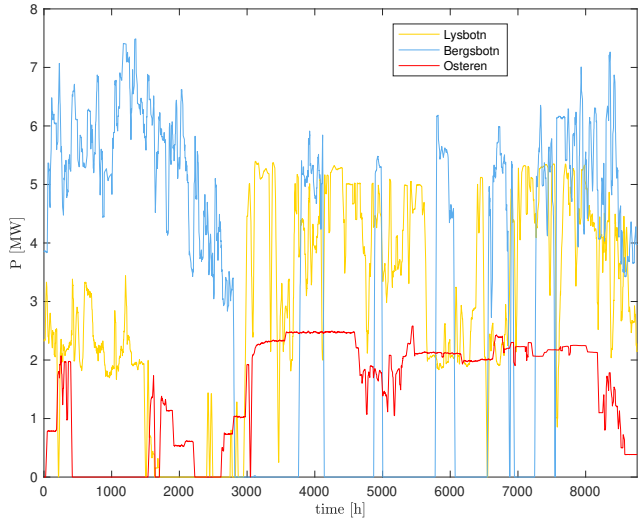

Figure 4.4: The 24-hour averaged production from the three hydro power plants at Senja in 2018.

In section 3.2 the operational principle of the power plants is explained. Optimal economic dispatch is the main reason behind the shape of the curve, as it can be observed that the production profile does not follow a typical load pattern. The result of this is that the network operator can't rely on power injection and correction from the power plants, which in turn complicates network operation from a voltage quality point of view.

4.2.2 Load Data

Load data for the period 1/11/2018-23/3/2019 at Husøy is given by *Troms Kraft*. The load profile is shown in figure 4.5.

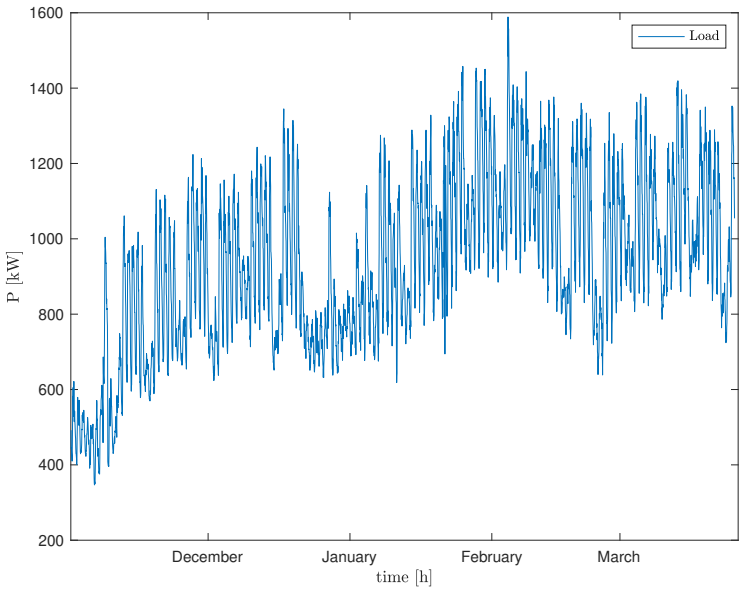

Figure 4.5: The load profile for Husøy in the period 1/11/2019-23/3/2019 in hourly values.

Figure 4.5 shows that the heaviest load during this period occurs in late January and early February. In the remainder of simulations, the load data present in the Netbas database will be utilized. The load data for 2018 is stored in the software, and all load scalings described in this chapter are scaled in accordance with 2018 load. From this data, the months with the highest peak demand is found to be within the period shown in figure 4.5. Thus it is assumed that the peak in the figure represents the yearly peak load.

4.3 Simulations on Distributed Renewable Generation Potential

4.3.1 Simulation Software HOMER Pro

HOMER Pro is used for performing simulations on the potential yield of the proposed distributed renewable generation. The software is one of the most widely used softwares for assessment of complex renewable energy systems. HOMER Pro is mainly targeted on small scale micro grid assessments, but can also be used for large grid connected systems. The software is developed by the National Renewable Energy Laboratory (NREL) in USA [Energy, 2019]. An advantage with the software is its user friendliness, as navigating within the software is easy. However, advanced configuration settings such as rooftop PV system scaling and shading analysis is not possible. In addition, the user cannot see nor interact with the codes used to produce outputs. This means that the user is not able to correct any bugs occurring in calculations.

The software inputs resource data such as wind and solar irradiance data, as well as performance parameters for each system component. The analysis is performed on an hourly time step, which implies that rapid power ramp rate behavior cannot be observed or analyzed. The software does also enable analysis on the effect of altering parameters such as weather resource data, efficiency and many more. All simulations on the distributed generation systems will be performed in HOMER Pro. The proposed solar and wind systems are of entirely different size and have different applications. Simulations will therefore be performed separately.

HOMER Pro was chosen due to its ability to simulate several components. Since both PV and wind systems are evaluated in this thesis, it was preferred to utilize a software capable of performing simulations for both systems. It was later found that the possibilities related to PV simulations were somewhat restricted, and some of these shortcomings will be discussed in the next subsection.

4.3.2 PV System Simulation Inputs

As described in section 1.2, the PV system considered in this thesis is a roof mounted system, and thus the space is restricted. The areas of the roof that will be covered in PV panels will be decided from a shading analysis of the roof structures. However, due to a confidentiality agreement with the owner of the factory, drawings of the roof will not be presented in this thesis. The area of installed panels will be quantified based on a standard 1.054 m x 1.590 m

PV module [Panasonic, 2017], and for the south facing system, the distances between rows will be calculated by using (2.19). A distance of 0.5 m is assumed between roof edges and PV arrays. It is decided that module shading should not occur for solar elevation angles above 10°. Simulations will be performed with a module tilt of $\beta = 10°$, further reasoning behind this choice is discussed in section 5.2.

It was also stated in section 1.2 that different orientations will be considered. Alteration of the panel azimuth angles will be performed in order to simulate this effect. The first configuration, PV1, will be a traditional south facing system with appropriate spacing in between rows (see section 2.2.5). The second configuration, PV2, will be a dome configuration with panels facing both east and west. HOMER does not allow for the configuration of a system with panels facing in different directions, and thus the output of PV2 will obtained by merging two simulations with different azimuth orientations. The panels will be aligned with the natural direction of the roof, which is deviating 20° from directly south. Thus, the panels will not be facing directly south or directly east or west. The directions of the PV system that will be used is shown in figure 4.6.

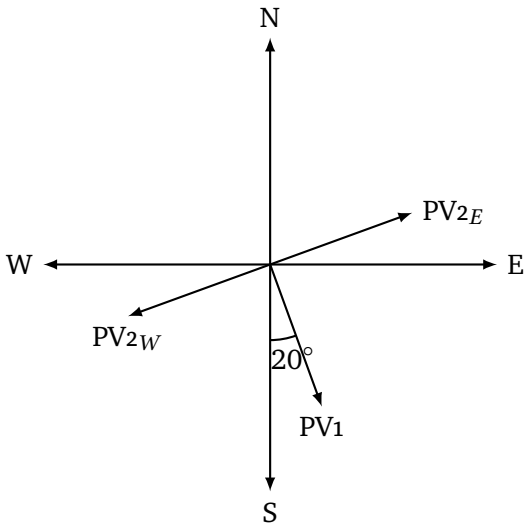

Figure 4.6: The resulting direction of PV panels for PV1 and PV2, both the east and west component of PV2 is shown.

As described in subsection 4.3.1, the software inputs performance parameters for the PV components. Thus performance parameters has to be defined before performing simulations. The system will be modeled with a PV module efficiency of 20 % based on information presented in subsection 2.2.4, as this resembles a typical commercial grade efficiency. Inverter efficiency typically ranges from 95-99 % [EnergyStar, 2013], and thus an efficiency of 97 % is

chosen for simulations. The inverter rating is automatically sized based on PV power output. In subsection 2.2.4, typical degradation rates and temperature coefficients are given. This information taken into account, a temperature coefficient of -0.4 $\%/^{\circ}C$ and a degradation rate of 0.4 $\%/year$ is utilized. The standard HOMER NOCT is used, in addition a derating factor of 90 % is defined to account for effects of shading and soiling.

HOMER does not account for changes in surface conditions. Based on observations in section 3.1, it is clear that the surface conditions will change over the course of a year. The effect will be approximated by merging simulation outputs with different ground reflectances. From November 1st to March 1st a ground reflectance of 90 % will be used, which resembles fresh snow cover. In the period March 1st to April 15th a reflectance of 60 % is chosen, as this resembles old snow cover. The rest of the year will be simulated with ground reflectance resembling cultivated areas, which is about 20 %. PV soiling effects are not included in simulations, other than through the derating factor, this has to be taken into consideration during the discussion of the results.

Table 4.2: Solar component and parameter settings for simulations

Component/Parameter	Input	Unit
PV module	Generic	
Electrical Bus	AC/DC	DC
STC Efficiency	20	%
NOCT	47	$^{\circ}C$
Temperature coefficient	-0.4	$\%/^{\circ}C$
Degradation Rate	0.4	$\%/year$
Derating factor	90	%
Panel slope	10	$^{\circ}$
Converter efficiency	97	%
Irradiance data	Imported	kW/m^2
Ground Reflectance	Varied	%
System lifetime	25	years

Table 4.2 shows the inputs for the PV system, based on the information presented in this section. All values are similar for both solar systems, except for installed capacity and panel azimuth angles. The GHI data is the imported data described in section 4.1, and the ground reflectance is varied as described earlier.

4.3.3 Wind System Inputs

The wind system considered in this study will consist of three Vestas V126 3.3 MW IEC class III wind turbines. Three turbines was chosen in order to keep the total rated power below 10 MW. The reasoning behind this is that concession applications have less strict rules for systems below 10 MW, and thus the possibility for realization is higher for systems of this size [NVE, 2007]. The power curve for these turbines is shown in figure 4.7. The turbines have a synchronous generator , which is driven by the turbine rotor through a three stage gear box (see section 2.3.5). The generator is connected through rated power converters. The control of the turbine is performed through pitch control and the variable speed of the generator. The tower height is 117 m, and the rotor diameter is 126 m [Vestas, 2019].

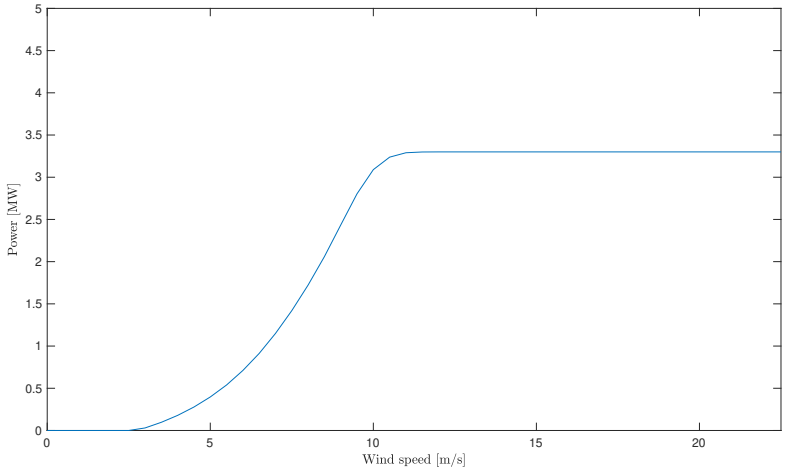

Figure 4.7: Power curve for the Vestas V126 3.3 MW turbine, retrieved from [windturbinemodels, 2015]

The air density was not defined for the curve, and it was thus chosen to use this curve throughout simulations, neglecting ambient temperature effects. Only electrical losses will be considered, but a sensitivity analysis will performed on the effect of increased losses (see section 4.3.4). [Colmenar-Santos et al., 2014] reports that typical power losses at rated power for a single turbine are 0.8 %. For a group of turbines the losses increase due to line resistance in the circuit. For a group of six turbines the losses are reported to increase to 1.1 % at rated power, while the total energy loss for various wind distributions is in the range of 1.1-2.1 %. Based on the average wind speed of the wind data (see section 4.1.2), the turbine losses is chosen to be 1.5 % in simulations.

To quantify the effect of surface roughness length, simulations will be

performed for several values. The roughness chosen for simulations is based on the WRF data's wind speed increase with height. By analyzing the WRF data, it was found that a roughness length of 0.05 m was appropriate. This seems to coincidence with the surface reported in section 3.1, which shows that the ground is covered in light coniferous forest. Due to the forest being coniferous, it was decided that the surface roughness will not be altered throughout the year in simulations.

Table 4.3: Wind component and parameter settings for simulations

Component/parameter	Input	Unit
Turbine	Generic	
Turbine Size	3.3	MW
Hub height	117	m
Cut in wind speed	3	m/s
Rated wind speed	12	m/s
Cut out wind speed	22.5	m/s
Number of turbines	3	
Electrical bus	AC/DC	AC
Wind speed	Imported	m/s
Anometer height	10	m
Height above sea level	236	m
Surface roughness	0.05	m

Table 4.3 shows the inputs for the wind system. The wind data is the simulated data discussed in section 4.1.2.

4.3.4 Sensitivity Analysis

As several parameters have a significant impact on the performance of the systems, a sensitivity analysis will be performed. First and foremost, the GHI and wind data is a representative of one single year. As there are yearly variations in wind patterns and yearly cloudiness, the effect of such variations will be examined. In addition to the weather data, the effect of altering the performance of other parameters is also of interest. All sensitivity parameters, and the values considered are summarized below:

- Global Horizontal Irradiance Data - 85 % (1.83 kWh/m^2), 90 % (1.94 kWh/m^2), **95 %** (2.05 kWh/m^2), 100 % (2.16 kWh/m^2), 105 % (2.27 kWh/m^2)

- PV conversion efficiency - 15 %, 17.5 %, **20 %**, 22.5 %, 25 %

- Wind speed - 80 % (4.28 m/s), 90 % (4.82 m/s), **100 %** (5.35 m/s), 110 % (5.89 m/s), 120 % (6.42 m/s)

- Turbine losses - **1.5 %**, 5 %, 10 %, 15 %, 20 %

The bold values are the values originally chosen for simulations. Altering the PV efficiency effectively change the power rating of the system, thus this effect will be simulated by changing the rated size of the system in HOMER. The effect of turbine losses is also of interest, since turbine losses can be considerable when wake and turbulence losses are included [Niayifar and Porté-Agel, 2016]. Thus the effect of increasing the turbine losses to resemble wake losses and turbulence will be examined.

4.4 Network Analysis

In the network analysis, two case studies will be performed. These are:

- **Case 1: The effect of Renewable Generation on Network Performance** In this case study, the effect of the simulated renewable energy systems on network performance will be analyzed. The *Salmar* factory will be connected to the network in this case study. The relieving capacity of the renewable generation will be quantified.

- **Case 2: The effect of power flow control on network performance** In this case study, the effect of SCC and BESS utilization on network performance will be assessed. The system will be designed to reduce current flow, and hence voltage drops in transmission line.

4.4.1 Simulation software: Netbas

For analyses related to optimization of power system performance, the simulation software Netbas is used. Netbas is a power system analysis tool developed by Powel, and is used by many network operators in Norway today, including *Troms Kraft*. The software gathers services such as documentation, grid maintenance and development as well as analysis in one platform. The software is essentially a Geographical Information System (GIS) for power system analysis, meaning that network components is geo-referenced. This makes maneuvering within the network easy [Powel, 2019].

The software enables the user to perform several forms of analyses on the power system. This include power flow analyses, which calculates the direction

and magnitude of active and reactive power flow as well as nodal voltages. When performing a power flow analysis, the load can be scaled in order to simulate different load conditions. Short circuit studies can also be performed within Netbas, which enables the user to quantify the network strength at different locations in the network. The selectivity of the network can also be studied within Netbas, to evaluate fault performance. The software does only support static calculations, meaning that the load flow is only calculated for a certain scenario at the time. This implies that transient fault analyses or any other sort of dynamical analysis is not possible to conduct within the software. As most of the problems considered by this thesis can be studied during static conditions, the software performs satisfactory.

One huge advantage with the software is that the exact topology of the power system is available in the network model. This means that the network model is built with all components and attributes. Access to the software and the model was provided by *Troms Kraft*, the model is also developed by them. Due to a confidentiality agreement, this model will not be shown, but the outline of the network can be seen in figure 3.5. The model can be simplified to only contain select subsystems. For example a part of the network situated below a power station in the network hierarchy, or analysis of a specific radial feeder.

Analysis Module

The majority of calculations are performed in the analysis module. In the analysis module, the network load can be specified. This can be done either by defining an overall load scaling, or by altering the load at individual customers. This enables the user to observe consequences related to changes both in evenly distributed load changes, or changes at individual establishments. After performing a power flow analysis within the module, the parameters of interest can be displayed. This include the power flow and nodal voltages discussed in the previous section. In addition one can determine power losses, which can be investigated down to component level.

The module also enables the user to perform topological changes in the network. This includes creating new power lines or cables, or connection of new loads. It also includes the connection of series and shunt elements such as capacitors or reactors. This allows the user to perform analyses and assessments on connection of new loads, new power lines or new components.

Detailed Analysis

Within the analysis module, one can perform a set of analyses which are conducted over time. One of them is the detailed yearly analysis, which calculates the solution and performance of the network in every hourly time step throughout the year. In this analysis, the software calculates the yearly load in MWh, as well as yearly losses in MWh. The monthly values are calculated as well, which enables the user to perform an assessment on performance throughout the year.

The analysis also enables several *advanced* options. These options include measures to control voltage, such as steping of transformers, or steping of shunt/series elements. The load is scaled in the same way as for normal load flow, and the software calculates the yearly load curve as a function of this.

4.4.2 Case Study: Effect of Renewable Generation on Network Performance

The network model in this assessment is the complete model of Senja, supplied by Finnfjordbotn network station. The 66 kV busbar at Finnfjordbotn is defined as the slack bus of the system, and hence maintains 66 kV consistently. The operation of hydro generators and the *Salmar* factory is shown in table 4.4.

Table 4.4: Rating and values for the slack bus, generators in the network and the factory

Component	Rating	Type	Parameters
Finnfjordbotn busbar	500 MVA	Slack bus	V = 66 kV
Lysbotn power plant	6.3 MVA	Inactive	P = 0 MW, V = 6.6 kV
Osteren power plant	3.150 MVA	Inactive	P = 0 MW, V = 6.6 kV
Bergsbotn power plant	10 MVA	Inactive	P = 0 MW, V = 6.6 kV
Salmar Factory	-	PQ bus	P = 9 MW, Q = 2.96

The hydro power plants are considered inactive, in order to asses the line loading during the worst case scenario. The worst case scenario will be considered, as it is the scenario that the network has to be dimensioned for. This is in order to prevent network breakdown if the scenario should occur. Load will be scaled 80 % in all simulations to resemble heavy load (see subsection 4.4.3), except for the *Salmar Factory*, which has maximal load. This load scaling is chosen in order to observe the immediate effect of the connection of the factory, and thus the overall increase in energy consumption described in subsection

4.4.3 will not be not considered.

Effect of Industrial Scale PV

As mentioned, the new factory planned at Silsand will introduce a new large consumer of power at Senja. A maximal active load power of 9 MW has been estimated, which will increase the overall maximal consumption at Senja by nearly 20 %. In simulations, this factory will be connected to the existing network through two cables connected to Silsand network station. The bottleneck for Senja's power system is the 66 kV cable from Finnfjordbotn, the loading of this line will be evaluated in simulations. The factory load will be simulated as a 0.95 pf inductive load, meaning that the maximal apparent load power demand becomes $S = 9 + j2.96$ MVA.

The results of the PV power potential simulations described in section 4.3.2 will be used in order to quantify how much the load can be reduced during certain periods of the year. This is to see if the implementation of such a system can contribute to keep the network from becoming overloaded. The performance will be calculated between 9 pm and 15 pm, as this is the period with typical high power price rates, as well as the period where a PV system has a good output. The average daily profile for each month will be used, and the following parameters will be considered: Minimal power output, average power output and maximal power output.

A case study will be conducted in Netbas, in order to quantify the PV systems ability to relive the power system bottleneck. As described in subsection 4.4.2, the hydro generators will be inactive, and the load will be scaled to 80 % to resemble heavy load conditions. A conductor temperature of $T = 80°$ is considered. The effect of PV generation on the main feeder loading will be examined. As the system size for PV and wind are different, a hypothetical upscaling of PV will be considered, to enable a comparison of the sources (see subsection 6.1.1).

Effect of the Wind Power Plant

The 9.9 MW wind power plant described in subsection 4.3.3 will be located along the 66 kV transmission line between Silsand and Svanelvmoen (see figure 3.5). An analysis of the network strength will be performed in Netbas, in order to quantify voltage increments as a result of the wind farm. This will be done by calculating the short circuit ratio, which is described in subsection 2.3.6. The reactive capability required in order to maintain voltage will also quantified. The voltage increments caused by the wind plant will be evaluated

with different power factor injections. Injections will be performed with 0.95 inductive, unity and 0.95 capacitive pf.

In order to quantify wind farm effect on network loading, simulations will be performed in Netbas. The wind farm will be modeled as a PQ-bus with unity pf, meaning that there is no reactive power injections or consumption. This implies that it is presumed that the wind power plant is corrected to unity pf. This pf will be maintained for all power injections by the wind farm, in order to provide comparable results. The analysis will be performed for several wind power outputs. The two first power outputs represents high production, while the other scenarios represent the high and low end of the probable average. In the discussion of the results, the potential for relieving the main feeder will be linked with the results of the wind system performance discussed in section 4.3.3. The production scenarios are summarized in table 4.5.

Table 4.5: Wind production scenarios considered in analysis of wind production effect on main feeder loading

Active Power [MW]	Reactive Power [Mvar]	Fraction of Rated Power
9.9	0	1
7.425	0	$^3/_4$
4.95	0	$^1/_2$
2.475	0	$^1/_4$

In the PV system assessment, the monthly daily profiles was considered. In the wind assessment, it was decided to perform the analysis for four fractions of rated power output. This is due to the fact that the wind power production would vary more randomly over the course of a month, while the PV production is dependent on the solar path. Thus the average monthly wind profile would be a poorer estimate of expected conditions, then in the case of the PV system. With this in mind, it was decided that the analysis presented would provide a better basis for analysis, because it is a representative of the whole wind power output range.

4.4.3 Case Study: Husøy

In this case study, only the radial 22 kV network supplying northern Senja will be considered. The network substation is chosen as the slack bus, meaning that the voltage at this node will always remain at 22 kV independent of network loading. This is done in order to produce comparable results in the analysis. Simulation will be performed for three different network configurations. Configuration one features todays network, configuration two utilizes SCC, and configuration

three SCC and BESS. Simulations for each load scenario presented in table 4.7 will be performed for each grid configuration. Prerequisites for the sources of power in the simulations are shown in table 4.6.

Table 4.6: Rating and values for the slack bus, as well as the generator at Lysbotn power station.

Component	Rating	Type	Parameters
Svanelvmoen busbar	100 MVA	Slack bus	V = 22 kV
Lysbotn power plant	6.3 MVA	PV-bus	P = 5.3 MW, V = 6.6 kV

In Netbas the load is referred to as a percentage of the maximal load for the previous year, where 100 % represents a scenario where all loads are subject to their maximal load. *Troms Kraft* informed that analysis concerning present low and high load situations are done using a scaling of 20 and 80 % respectively. In order to asses the grid performance in future scenarios, different scalings of heavy load will be considered.

Load prognoses presented by *Sjømannsklyngen Senja*, presents a possible increase of 200 % in energy demand from the fishing industry by 2030 [TKN, 2016]. Today this industry accounts for about 20 % of the total energy demand at Senja [TKN, 2018], and thus such an increase will contribute an overall increase of about 40 % from todays total energy demand. It is however difficult to predict how the load demand will develop in the radial feeder considered in this case study, and thus it was decided in conversation with *Troms Kraft* on four suggested scenarios entitled S1-S4. S1 presents present day heavy load. S2 has a 10 % increase in overall load, representing an even growth in demand among residential and industrial scale customers. In S3 and S4 industrial scale loads have a higher growth rate than residential customers. Industrial loads are scaled by 130 % and 150 % in scenario three and four respectively. The scenarios are summarized in table 4.7. All simulations will be performed with a conductor temperature of T = 20°C, in order to provide comparable results.

Table 4.7: Future load scenarios for the radial feeder supplying Husøy at northern Senja. The percentage in the parenthesis indicates the increase from 2018 load power.

Scenario	Residential scaling	Industrial scaling	Load [MW]
S1	80 %	80 %	3.615 (0 %)
S2	90 %	90 %	4.072 (12.6 %)
S3	90 %	130 %	4.560 (26.1 %)
S4	90 %	150 %	4.808 (33.0 %)

Shunt Capacitor Compensation

As mentioned, SCC is considered to provide reactive power compensation, and thus improve voltage and reduce system losses. The working principle of SCC is explained in subsection 2.1.2. In subsection 2.1.4, several methods for solving the allocation problem of SCC in radial distribution networks was presented. It was decided to implement a method that was able to efficiently allocate SCCs based on obtaining optimal network performance. Due to restrictions on the ability to implement user defined methods into the simulation software, the method proposed by [A. Salama et al., 1985] was used. It was found that this method was of relevance, since it considers a radial feeder with a considerable end load, which is also the case in the network considered. The method is considered to be of the more accurate analytical placement methods [Aman et al., 2014]. The algorithm is explained in appendix B.

It was described in section 1.2, that the main objective of the SCC installment is improved system performance during all conditions. The dimensioning condition for system performance is the worst case scenario, hence the allocation problem will be solved for this scenario. The worst case scenario in this case refers to zero hydro production during heavy load. This justifies the simplicity of the allocation method, due to the fact that it considers similar conditions. When the allocation problem is solved, three variables are of interest. The total reactive current (I_1), the fraction of this supplied to the end load (I_2) and the number of capacitors installed. The allocation problem will be solved for S1-S4, and a configuration will be chosen for network implementation.

In addition to the allocation of SCC along the main feeder, large industrial customers elsewhere in the network will also be considered for SCC implementation. The reasoning behind this, is that large industrial customers often have a high reactive power consumption, and thus reactive current flow increases the overall system losses. As reported in subsection 2.1.4, limiting these reactive currents are beneficial for network performance. Thus large consumers of reactive power not located directly along the feeder part should also be fitted with SCC. It is important to note, that even though the allocation problem will be solved for a specific scenario, it is intended that the SCCs should implement stepping, which is described in the system loss section.

Battery Energy Storage System

In addition to the shunt capacitor compensation, a BESS located at Husøya is considered. The battery will be performing peak shaving to limit active power demand in the network. The peak shaving algorithm proposed by [Rahimi et al., 2013], was used as a basis for the peak shaving algorithm. However an

alternative method for quantifying battery utilization was used. This method is explained in appendix C. In simulations the amount of power shaved will be subtracted from the industrial loads at Husøy. As the industrial loads at Husøy is modeled with a 0.95 pf, the battery power injection is also performed at this pf in order to avoid lowering the load pf. Since batteries deliver DC power, this has to be done through power electronics. The load data presented in section 4.2.2 only feature the active power consumption at Husøy, and thus the shaving will be performed based on the active load power.

The energy capacity of the battery will be scaled such that it provides desirable performance during the heaviest load scenario. Desirable performance is chosen to be a battery that can deliver the demanded power and energy, with a Utilization Factor (uf) above 0.85 without discharging completely in each discharge cycle. The power capability of the battery will not be evaluated in much detail, other than that it will be sized to be able to supply the required power capability for maximal shaving. The shaving algorithm was selected due to its performance oriented approach. Other algorithms presented in section 2.2 emphasize optimal economical gain, and since the objective discussed in section 1.2 is to improve performance, the operational principle proposed by [Rahimi et al., 2013] is chosen.

Limited Hydro Production

During simulations, Netbas assumes high production in hydro power plants as standard. Since the hydro power plant Lysbotn operates based on optimal economical dispatch, the effect of limited hydro production will be discovered. Figure 4.4 was examined in order to find a typical low production scenario during a high load period. An extreme case where the power plant is out of operation is also considered. The synchronous generator will also be operated as a generator bus in this case, keeping a steady voltage of 6.6 kV as well as constant active power production. Due to over-excited operation during lower production to maintain voltage, the generator will typically inject reactive power into the grid. This will give a reactive power compensation in itself, thus it is interesting to evaluate the performance of compensating components with this in mind. The operation of Lysbotn in the two cases is:

- Operated as PV-bus - P = 1.75 MW and V = 6.6 kV. The voltage is increased in order to utilize the reactive capability of the generator.

- Inactive - P = 0 MW. No injection from the power plant.

System Losses

The overall losses of the system is of great importance for network operators. Therefore, *Troms Kraft* wants to investigate the possible loss reduction that can be obtained using SCC. Thus, in addition to the high load scenarios, a detailed simulation over a year will be performed. Only shunt capacitors will be included in these simulations, as the operation of a BESS was hard to implement into the module. In addition, the power loss saving from capacitors will be the main feature of interest for the network operator, as they contribute a direct saving. What is meant by this, is that they reduce losses, while the same amount of active power is supplied to customers. The placement and sizing of the capacitors is the same as for other simulations. The effect of the complexity of the compensator system will be examined, using different amounts of steps available within the capacitors. The configurations considered are summarized in table 4.8.

Table 4.8: Complexity of capcitors used during analysis of capacitor complexity effect on system losses.

Configuration	Shunt capacitors	Steps
1	no	zero
2	yes	1
3	yes	5
4	yes	10

The analysis on the effect of capacitor complexity will be performed in order to assess whether it is worth investing in a more complex system. The easiest configuration, which only has the possibility to be ON or OFF, is of lesser cost than more complex systems [NEPSI, 2012]. In the analysis the capacitors will be operated based on voltage regulation. Since Netbas features a somewhat black box layout, it is not possible to account for what operational regime this implies. However, it is stated that the *optimal* capacitor step is found in each time step, to ensure optimal operation.

5

Performance of Renewable Energy Sources

5.1 Statistical Analysis of Weather Data

5.1.1 Accuracy of ERA 5 Solar Irradiance Data

The Pearson correlation coefficient (equation 2.30) and the bias (equation 2.31) for the simulated and measured solar radiation data at Holt weather station is shown in table 5.1. The coefficients are calculated for hourly, daily and monthly values. Due to the amount of zeros in simulated data for December, no Pearson correlation is found for this month. Weekly and monthly values are only calculated for the whole year, while daily and hourly correlations are calculated on a monthly basis.

Table 5.1: Pearson correlation coefficient and bias for simulated and measured solar irradiation data at Holt weather station in 2017.

Time period	Coefficient	Resolution		
		60 min	24 hours	Weekly
Yearly	Pearson	0.9314	0.9632	0.9895
	Bias	3.0665	3.0675	3.0759
January	Pearson	0.6965	0.6039	-
	Bias	-0.8011	-0.7815	-
February	Pearson	0.8197	0.5753	-
	Bias	0.5449	0.6430	-
March	Pearson	0.8884	0.5746	-
	Bias	16.9874	16.7358	-
April	Pearson	0.9518	0.9425	-
	Bias	14.5804	14.0770	-
May	Pearson	0.8993	0.8505	-
	Bias	9.6104	9.3174	-
June	Pearson	0.9023	0.9045	-
	Bias	-7.8532	-3.4943	-
July	Pearson	0.8979	0.9329	-
	Bias	0.7998	0.2639	-
August	Pearson	0.8752	0.8291	-
	Bias	1.4348	-1.0848	-
September	Pearson	0.9262	0.8243	-
	Bias	0.5164	0.0992	-
October	Pearson	0.9499	0.9618	-
	Bias	1.2381	1.1720	-
November	Pearson	0.8271	0.6352	-
	Bias	-0.2983	-0.0470	-
December	Pearson	-	-	-
	Bias	-0.3776	-0.3782	-

Table 5.2: Measured and simulated mean solar irradiance [$^{W}/_{m^2}$] for Holt weather station in 2017.

Time period	Holt	Holt ERA 5
2016	83.75	86.82
January	1.08	0.27
February	13.67	14.21
March	50.35	67.34
April	150.24	164.82
May	169.62	179.23
June	224.20	216.34
July	165.24	166.04
August	113.76	115.19
September	86.04	86.56
October	25.38	26.62
November	2.20	1.90
December	0.38	0.0

The observations from table 5.2 is presented visually in figure 5.1, which shows 24-hour averaged values for both measured and simulated data.

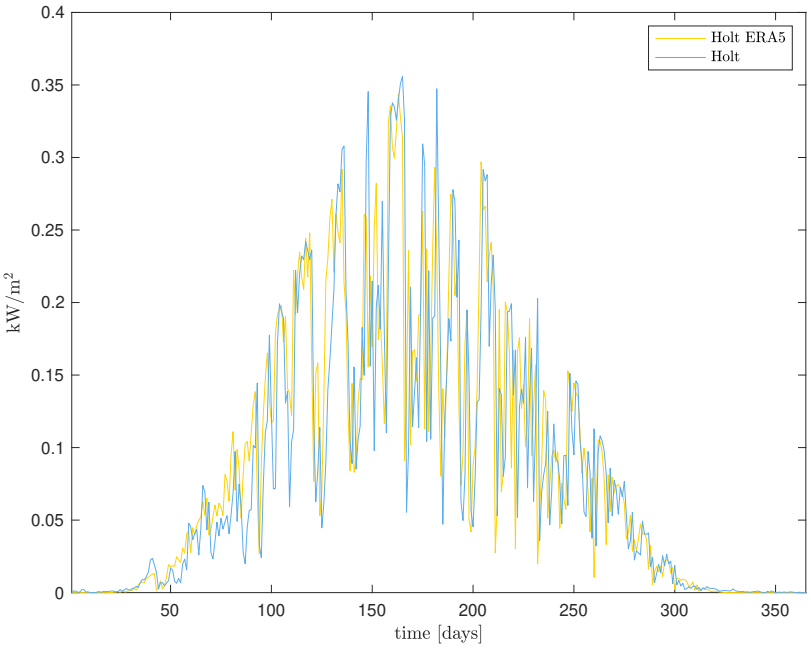

Figure 5.1: 24 hour averaged solar irradiance data for Holt, comparison between measured and simulated data.

From table 5.1 it can be observed that most months, the Pearson correlation shows a high to very high positive correlation (see table 2.3). For the hourly data, only January shows a lower than high correlation, falling into the medium category. For the daily values January, February and November show medium positive correlation, while the rest of the months have high to very high correlation. The yearly correlation coefficient is very high for both hourly, daily and weekly averages.

Both the monthly and yearly bias show little deviation between resolutions. Simulation errors seem to be most significant in the months March through June, while the rest of the months have small biases. The yearly average bias of about 3.07 $^{W}/_{m^2}$ shows that the simulated data only overestimates slightly over the year. This is also evident from table 5.2, which shows the overall tendency of a slight overestimation. As mentioned, the overestimation is most prominent during March through May, while the simulated data underestimates the irradiance in June.

A shift of the solar noon was found in the simulated data. Thus the data was shifted 7 hours, to better align the solar noon of the two data sets. The overall impression when examining the data more thoroughly is that this just is a timing-error in the data. However, some days seem to have a slight shift in solar noon compared to measured data, even after the shift. Shifting of values might produce errors in correlation calculations, meaning that the correlation between the datasets might be even higher in the absence of the shift. As mentioned, the overall tendency in the datasets is an alignment of the solar noon, and thus this will not be addressed further.

The simulated data overestimates the measured data by 3.7 %. This implies that a scaling of the simulated data is necessary during simulations. A scaling of 95 % was selected for the solar irradiance data. Since the statistical analysis is performed at Holt weather station, there is no guarantee for exactly the same results at Silsand. However the both Silsand and Holt are located at sea-level, and have very similar climatological conditions, which could indicate that a similar tendency could be observed at Silsand.

5.1.2 Solar Irradiance Data at Silsand

Silsand is located a little further south than Holt, and one would expect that the solar potential is slightly higher at the location. The total solar radiant energy for Holt and Silsand is shown in table 5.3.

Table 5.3: Yearly energy yield in 2017 at Holt and Silsand, measured data is presented for Holt, while ERA5 data is presented for both Holt and Silsand.

Location	$^{kWh}/_{m^2}$ 2017
Holt	733.65
Holt ERA 5	760.54
Silsand ERA 5	786.83

Since no measured data for Silsand exists, it is not included in the table. However, in the future the installed pyranometers will provide accurate measurements for more accurate assessment. Table 5.3 shows us that the yearly global horizontal solar energy yield as expected is slightly higher at Silsand compared to Holt in Tromsø. With a scaling of 95 % as discussed, the yearly solar potential sums to 747.49 $^{kWh}/_{m^2}$. In order to quantify wether the year 2017 is a good representative, the GHI for 2012-2017 was retrieved. Ideally this analysis should have been performed for more years, however data was only available for 2012-2017. It was found that the average in this period was 2.04 $^{kWh}/_{m^2}$. Thus 2017 had a 5.9 % higher average potential than the average in the years 2012-2017. The sensitivity analysis in section 5.2.3, will quantify the effect a lower output would have on performance.

5.2 Technical Performance of the PV System

5.2.1 PV System Configuration Effect on System Yield

In subsection 4.3.2, two PV system alternatives was proposed. The tilt angle $\beta = 10°$ described in subsection 4.3.2, is chosen to prevent shading of panels for solar elevation angles above 10°. If the tilt had been chosen higher, PV2 panels would become shaded for elevation angles above the defined limit. In addition a larger spacing would be required for PV1. HOMER does not allow for automatic rooftop system sizing, thus the total area of installed panels is calculated manually in accordance with the method described in subsection 4.3.2. The shading analysis found that a total roof area of 10300 m^2 was suitable for PV panel placing. The resulting configurations are shown in table 5.4.

Table 5.4: Orientation, panel slope and panel area for PV1 and PV2.

Scenario	Panel slope [°]	Φ [°W of south]	Area [m^2]	Rated Power [MW]
PV1	10.00	- 20.00	5000	1 MW
PV2	10.00	70.00 and -110.00	9500	1.9 MW

The simulated yearly potential with the inputs defined in section 4.3.2 for

the two systems given in table 5.5. The values shown in the table are produced with the varying ground reflectance also described in section 4.3.2. Values are shown for the first and last year of the system lifetime. The output in the last year is reduced compared to the first year due to the deterioration of the PV material.

Table 5.5: Yearly energy production, converter output and capacity factor of the two suggested PV systems

Configuration	Energy Production (MWh)	Converter Output (MWh)	Capacity Factor (%)
PV1	775/704	752/683	8.8/8.0
PV2	1334/1212	1294/1176	8.0/7.3

The results in 5.5 tells us that PV1 has a production of 775 $^{kWh}/_{kW_p}$, while PV2 has 702 $^{kWh}/_{kW_p}$. Compared to typical values reported in Norway [Solenergi, 2017], this is on the low side. Typical rooftop systems are however mounted at higher tilt angles, and with the panel slope angle in mind, the energy output can be classified as good. Despite having a lower output per kW_p, PV2 has a production of 129 $^{kWh}/_{m^2}$ of considered roof area, while for PV1 this number is 75 $^{kWh}/_{m^2}$. Thus PV2 obtains a much higher specific energy production. The capacity factor is slightly lower for PV2, which is a consequence of the azimuth orientation of the panels. The effect of altering azimuth angles is illustrated in figure 5.2, where the average daily profile for June is shown. The figure shows the yield of PV1, as well as the the east and west component of PV2.

It can be observed that even though the east component of PV2 has a lower power rating (0.95 MW) than the south facing system, it has a higher production during the early part of the day. The same goes for the west component, which produce more power than PV1 in the afternoon. Due to the azimuth orientation of the roof, which deviates 20° from directly south, this effect is more pronounced in the evening, as the west component is the component which is oriented closest to south. The effect of having an east/west configuration is that more power is produced in these periods, and less midday, compared to a south facing system. Electricity spot prices varies throughout the day, and are typically higher in the morning and evening. This shift in generation towards periods with higher electricity rates, might outweigh the overall reduced output per panel [Stoker, 2018]. Based on these observations, in addition to the increased overall production, PV2 is deemed the most suitable configuration. Thus further analyses will consider PV2.

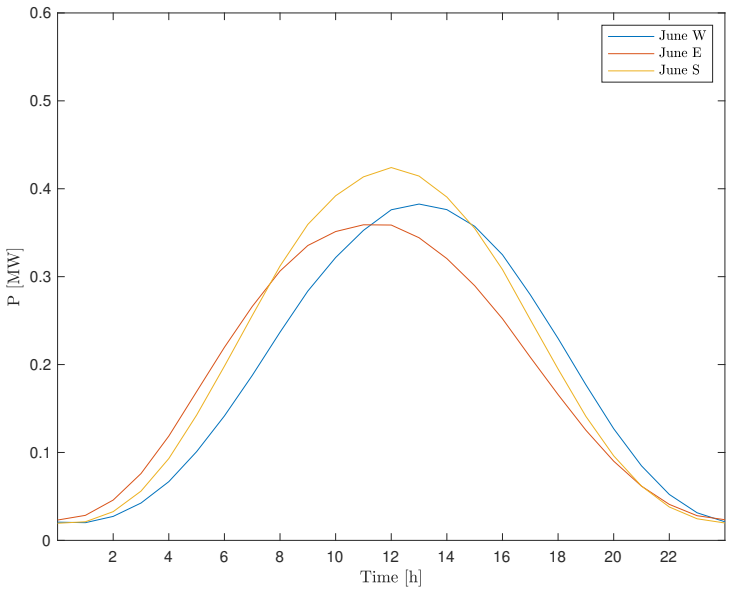

Figure 5.2: The average daily profile in June for PV1, and the east and west component of PV2

HOMER models a central inverter. This has little impact on simulation results since the same radiant power is assumed for all panels. However, in a real life assessment, the pros and cons of the array configurations presented in subsection 2.2.5 should be evaluated. This has to be done due to the fact that the central inverter configuration not necessarily is the best configuration for the location.

5.2.2 Yearly Variations in Production

The production of a PV system over the course of a year will vary considerably at high latitudes due to seasonal changes in the solar path. This results in high production during summer, and low production in the winter. As described in subsection 4.3.2, the surface conditions also vary over the course of one year. Since the surface tilt angle of the panels is as low as 10°, the contribution of the reflected radiation is assumed small. As shown in (2.10), the reflected radiation on a collector surface is proportional to $\frac{1-\cos\beta}{2}$ which gives a very weak dependence for low tilt angle (β). As an example, a collector at 60° tilt will receive 33 times the reflected radiation compared to a collector tilted 10°. Based on this observation, it is expected that the change in ground reflectance will have little effect on PV output. The output in year one with different ground reflectances is shown in table 5.6.

Table 5.6: The effect of varying the ground reflectance in simulations

Albedo [%]	**Energy Output** [MWh]
20	1330
60	1334
90	1337
Merged	1334

Table 5.6 clearly show that the effect of altering the ground reflectance is small. The increase in yearly production from increasing the ground reflectance from 20 to 90 % increases the yearly energy output by 7 MWh or 0.52 %. The increase in yearly energy production from the variations in surface explained in subsection 4.3.2 is 0.3 %, and thus reflected radiation from increased ground reflectance has very little impact on the yearly production. As mentioned in subsection 4.3.2, soiling effects from snow or other particles are not simulated in HOMER. Some soiling/shading is assumed through the derating factor, but it does not account for yearly variations due to snow. The most prominent soiling scenario would be due to snow in the winter, however radiation intensity is low in winter months. Thus the effect of soiling would probably be small on the system output.

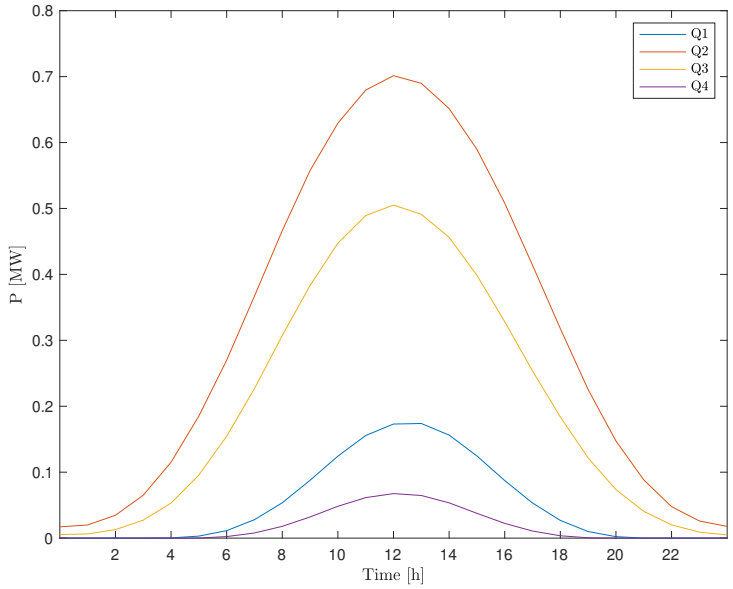

Figure 5.3: Average daily production profiles for each quarter of the year.

As previously mentioned, the output from PV installments at high latitudes will vary during the year. In order to observe the differences in different periods of the year, the average quarterly daily profile was calculated for all four quarters. The resulting average profiles are shown in figure 5.3. Quarter 1 (January-March) and 4 (October-December) have very limited production on average. Consequently the ability to contribute load shaving during these periods is low. Quarter 2 (April-June) has the best daily profile, with high production during most parts of the day. Quarter 3 (July-September) also show a good average production despite being lower than for quarter 2. It is evident that the most beneficial period for the plant owner would be quarter 2 through 3. The power duration curve is used to quantify the total time during a year the production is over a certain threshold. Figure 5.4 shows the duration curve for the production in year one.

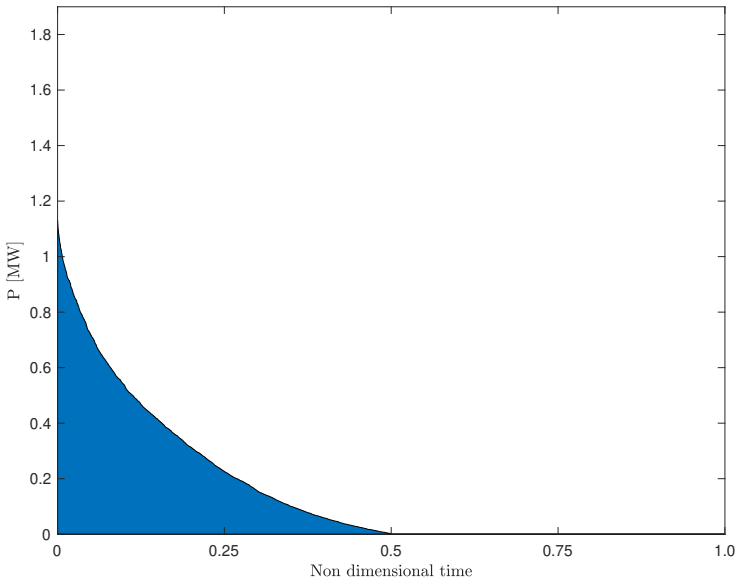

Figure 5.4: The power duration curve for the solar system, with hourly resolution. The filled area compared to the whole plot area illustrates the capacity factor

Half of the year the sun is suspended behind the horizon, thus there is zero production in this period. It can also be observed that a production of above 200 kW is maintained for a period corresponding to a quarter year, and that peak production is close to 1.2 MW. The curve gives a general overview of the yearly duration of power outputs. It also effectively illustrates that during real conditions, rated power production will not be obtained. The effects on power consumption from the factory that the PV system has, will be discussed in greater detail in section 6.1.

5.2.3 Sensitivity Analysis

As mentioned an analysis on the power output sensitivity is performed. The sensitivity variables is PV conversion efficiency, as well as the intensity of the solar irradiance data. The sensitivity is summarized in figure 5.5.

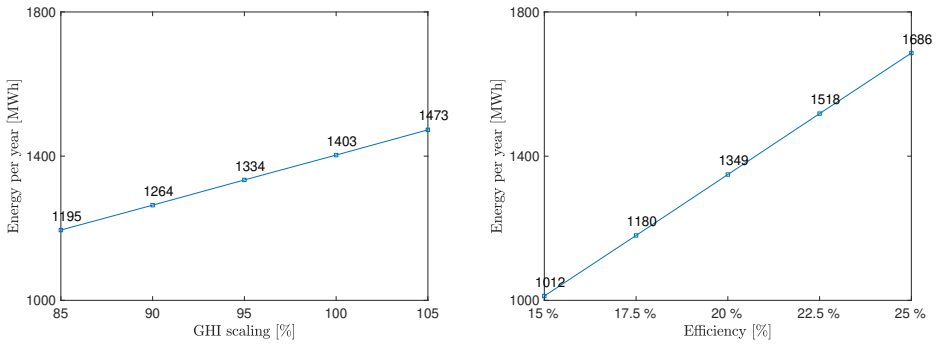

(a) **(b)**

Figure 5.5: The Energy output sensitivity to a) Global horizontal irradiance intensity and b) PV efficiency

The energy output shows a higher sensitivity to efficiency. This is mostly due to the fact that the steps between the efficiency values are larger percentage wise compared to the GHI steps. The energy production in fact shows an almost perfect linear relation for GHI, and as expected the sensitivity to efficiency is perfectly linear. When altering the scaling of the GHI resource, the capacity factor changes. With the lowest scaling a capacity factor of 7.2 % is obtained, and with the highest scaling it becomes 8.9 %. It was mentioned that the GHI for 2017 was 5 % higher than the average for 2012-2017. Thus the 90 % scaling, which corresponds to a capacity factor of 7.6 % represents the production that can be expected based on the average of the 6 year period. Increase in efficiency does not affect the capacity factor of the system, as the system rating changes proportionally to energy production. If the system was a south facing system with unlimited space, the sensitivity of the panel slope angle would be interesting to explore. However, it is not performed due to the restricted space and shading criteria discussed in section 5.2.

5.3 Technical Performance of the Wind Turbines

5.3.1 Analyzing the Effect of Surface Roughness Length

The proposed area of installation is a mountain ridge. However the elevation above sea level is only about 230 m, and thus there are trees present. This made it difficult to decide on the surface roughness length, and thus the effect it has is analyzed. As described in subsection 4.3.3 a surface roughness of 0.05 m is chosen for simulations, and the surface roughness is not varied due to the presence of coniferous trees, which do not vary as much in texture during the year as other trees. It was decided to analyze the effect of both increasing and reducing the roughness, as the surface roughness in the WRF model does not necessarily resemble the actual conditions. Thus the effect of varying the roughness is examined. It comes from (2.23) that increased surface length will yield higher winds at altitude, which in turn will imply higher production from the wind turbines. Table 5.7 shows the sensitivity of production with roughness lengths of 0.01 m, 0.05 m and 0.1 m.

Table 5.7: The effect of different surface roughness on wind turbine production

Surface roughness (m)	0.01	0.05	0.1
Production (MWh)	31 151	33 953	35 634

The results show that the largest difference is between a roughness length of 0.01 m and 0.05 m, where the yield increases by 9.0 %. An increase of 5.0 % is observed if the roughness is increased additionally to 0.1 m. This shows that the results depend on the roughness length chosen for simulations, and this must be kept in mind in further discussion. In order to quantify the real surface roughness, detailed analysis of the terrain with high resolution should be performed. As described in subsection 4.1.2, the WRF model has a resolution of 1 km, which might fail to render the surface conditions correctly. Accurate results would then be obtained by coupling such calculations with wind measurements.

5.3.2 Wind System Output

In order to quantify the performance of the wind system, the yearly output has to be evaluated. Table 5.8 shows the performance of the wind system for the wind pattern in 2017. The following results are produced with the parameters described in subsection 4.3.3, meaning that the turbine losses are 1.5 % and surface roughness is 0.05 m.

Table 5.8: Yearly production, average power output and capacity factor for the wind farm in 2017

Yearly Energy Production (MWh)	Average Power Output (MW)	Capacity Factor (%)
33 953	3.88	39.2 %

The yearly output from the wind turbines shows great potential for this site. With a capacity factor of 39.2 % and average power output of 3.88 MW, a good performance is obtained. The average capacity factor in Europe in 2018 was found in [WE, 2018] to be about 24 %, and hence a capacity factor of 39.2 % must be seen as very good. However only electrical losses in the turbines are considered, which probably causes an overestimation. If turbulence and wake losses is accounted for, the output will be reduced. In addition, HOMER does not factor wind direction, which equates to the turbines always facing directly into the wind. With variations in direction, the turbine has to adjust, which introduces a time delay due to the turbine jaw control. Wind gusts of short duration from other directions, would not be perfectly captured by the wind turbines either. These effects would also contribute in reducing the energy output of the turbines. The extent of these reductions depends on the steadiness of the wind direction. The direction of the wind throughout the year is shown in figure 5.6. It can be seen that the wind varies quite much during the year. Some periods are more steady than others, and thus the losses associated with wind direction will vary.

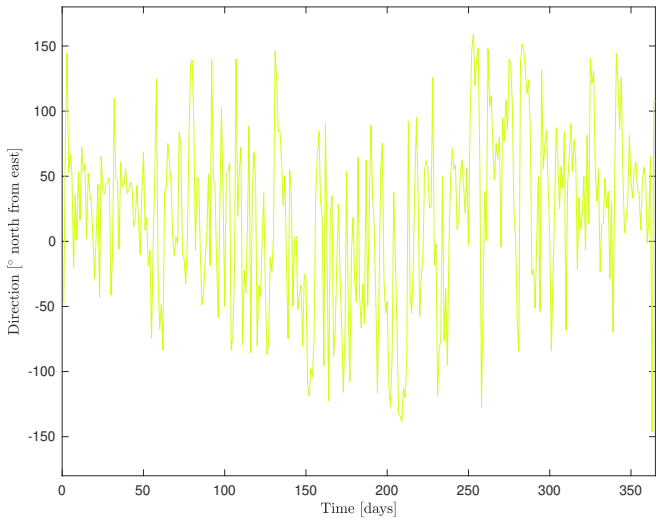

Figure 5.6: The 24 hour averaged wind direction over the course of 2017. The angle represents the deviation from east, where positive direction is in the north direction.

In comparison to a PV system, a wind system will produce a much steadier output averaged over the year. Yearly variations will still be present, with different daily average wind patterns. However, a wind system greatly reduce the problems associated with seasonal changes, compared to a PV system. In order to show the daily wind pattern during the year, the average daily profile for each quarter is plotted. The resulting graph is shown in figure 5.7.

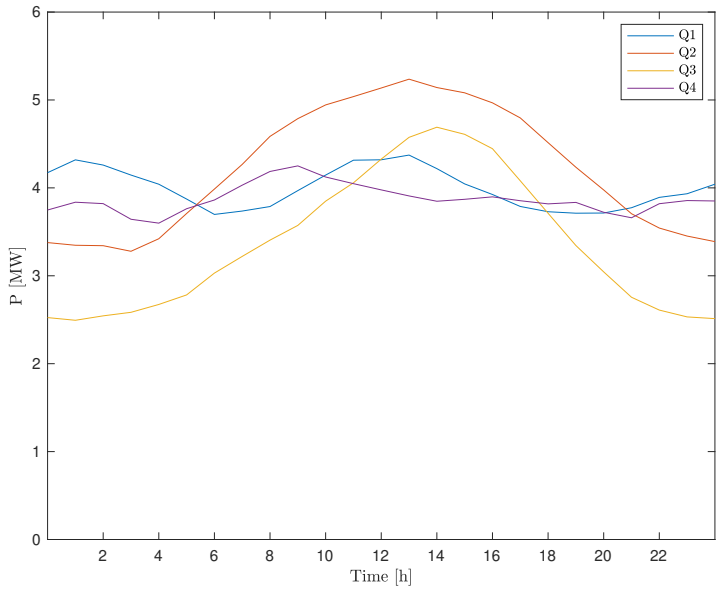

Figure 5.7: The average daily wind output profile for each quarter in 2017

It is clear from figure 5.7 that on average, the wind output is steadier throughout the day in the winter months. In quarter 2 and 3, an increase in wind is typically observed during midday. To learn if this is a long term trend, or just a yearly coincidence, would require a greater amount of data for the site. Typically several years of measurements. The results obtained from the data available, shows that the power output during midday on average is kept in the range 3-5 MW. However, varies greatly on a daily basis. Figure 5.8 shows the power duration curve, which shows that the wind system has considerable production during large fractions of the year. The relieving ability this wind system could have on the power system at Senja will be discussed in grater detail in section 6.1.

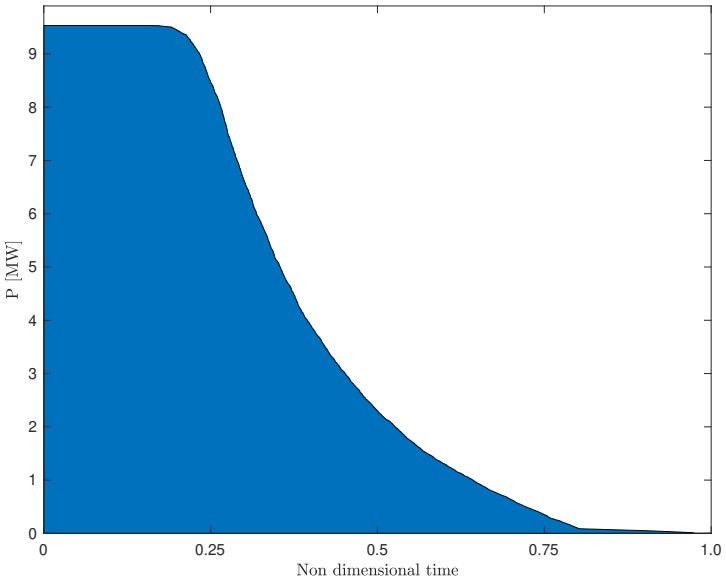

Figure 5.8: The power duration curve of the wind farm. The filled fraction compared to the whole frame illustrates the capacity factor

5.3.3 Sensitivity Analysis

In order to evaluate the sensitivity of certain parameters, sensitivity variables is defined. As described in subsection 4.3.4 the wind speed was chosen based on the uncertainty of the simulated data, as well as to quantify the effect of yearly wind variations. This is of interest as the variations could not be evaluated otherwise, due to the lack of wind data for several years. Turbine losses was also included, in order to quantify the effects of different amounts of losses. The sensitivity plots for wind speed and turbine losses is shown in figure 5.9.

The turbine output show an almost linear relation with wind speed scaling. However the increase in energy output is highest for the lower scalings, this is due to that with increasing wind speed, more of the power will be produced at rated power. The power in the wind fraction that is above rated speed is shed in order to keep the turbine at rated power. Thus increasing wind speed would eventually converge towards rated power being put out all the time. The capacity factor for different scaling range from 29.8 to 46.5 %, meaning that with a scaling of 80 % the capacity factor would still be higher than the average for large scale wind in Europe. The sensitivity to turbine losses is lower compared to wind speed. The capacity factor of the wind turbines is 31.8 % with 20 % turbine losses. Thus the output is still good in the case of high

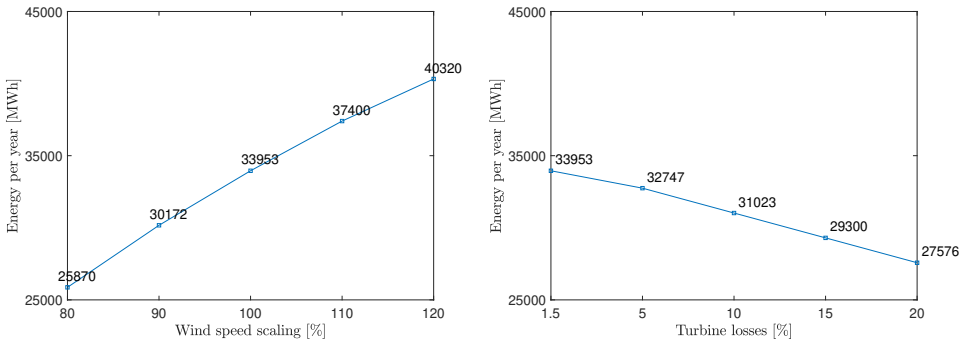

(a) **(b)**

Figure 5.9: The Energy output sensitivity to a) wind speed intensity and b) Turbine losses

turbine losses.

5.4 Sources of Error

In the simulations presented in this chapter, several sources of error are must be taken into account. Some of them are discussed earlier in the chapter, but the most important sources of error will be summarized. First and foremost, both the PV and wind potential has been quantified using simulated weather data, which introduces a degree of uncertainty. The GHI data was evaluated through a statistical analysis, so this uncertainty applies to the wind data to a greater extent.

Hourly temperature data for the location was not found, thus monthly averages was used. This introduces a degree of uncertainty due to the fact that the daily variations in temperature is not captured. This can cause a slight overestimation of simulated output during midday for the solar component.

As mentioned, the turbulence and wake effects at the wind site are not quantified. This introduces a degree of uncertainty, as it is difficult to estimate this value. Thus it must be factored that such losses are not considered. Surface roughness length does also introduce some uncertainty in the simulation results, as does the neglecting of wind direction.

6

Network Analysis

6.1 Effect of Renewable Generation on Network Performance

6.1.1 The Effect of Industrial Scale Solar

In this section the performance of the solar system presented in section 5.2 is discussed in context with network operation at Senja. As mentioned, the factory in question is a large fish processing factory. The highest consumption of power will, based on information received from *Salmar*, be during the summer months where large amounts of power is required for cooling. Thus the production in the summer months is especially interesting, as the highest consumption is thought to occur in the summer, not during winter. The quarterly production profiles in figure 5.3 show that production is high in quarter two and three. The voltage increments as an effect of the system will not be discussed, as it is assumed that all produced power is consumed by the factory, and hence no power is injected into the network.

The performance of the system is studied on a monthly basis, where the average daily profile for each month is utilized. Minimal power in the period 9 am to 3 pm is found, which quantifies the minimal expected production in the time frame. The average and maximal production is also found for time frame. Figure 6.1 shows the results of the analysis.

Table 6.1: The minimal, average, and maximal production for each month between 9 am and 15 pm. Based on the average monthly profile.

Month	Minimum Power (MW)	Average Power (MW)	Maximal Power (MW)
January	-	-	-
February	0.043	0.093	0.125
March	0.216	0.326	0.389
April	0.520	0.643	0.716
May	0.534	0.600	0.655
June	0.615	0.670	0.722
July	0.476	0.537	0.584
August	0.370	0.434	0.481
September	0.302	0.386	0.448
October	0.090	0.142	0.181
November	0.009	0.013	0.020
December	-	-	-

The average production in the considered period for each month, is used to quantify the average daily load shaving potential. It is considered that the factory has its peak load of 9 MW, and the amount of active load power shaved as a percentage is calculated. The results are shown in figure 6.1.

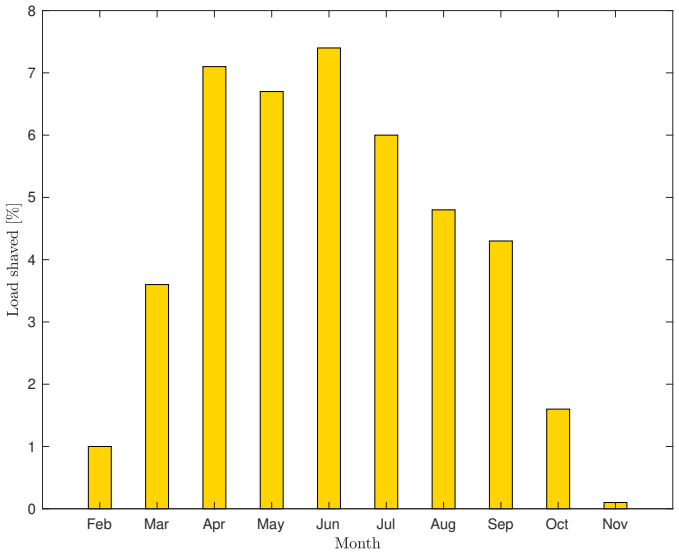

Figure 6.1: The average shaved fraction of factory load during the period 9 am to 3 pm for all months with PV production. The factory load power is assumed to be 9 MW in all cases.

June shows the best production potential, which is expected based on the energy potential for this month shown in table 5.2. The average shaved fraction for the average day in June, is 7.4 %. The peak load reduction is on average 8.0 % for June. The maximal production obtained throughout the year of 1.2 MW would decrease maximal load power by 13 %. In April and May the load demand is on average reduced by 7.1 % and 6.7 % respectively in the time frame considered. In July and August, the load demand is reduced by an average of 6.0 and 4.8 % respectively. In the remaining months the solar production's effect on factory load is limited. A smoother output from the PV system can be obtained through the utilization of a BESS, the effect of this is named as one of the possible subjects in future work.

The power output can be driven towards the average power output considered in figure 6.1, through the utilization of a BESS. The BESS could be operated in a similar manner as the operational principle proposed for peak shaving, which is described in appendix C. Only in this case, the PV output curve is driven towards the floating average. Smoothing of rapid fluctuations is also a highly relevant application. In order to evaluate the effects of this however, higher resolution production data would be required. This is due to the fact that the fluctuating behavior occurs on a time scale of seconds, not hours.

In order to quantify the effect PV production has on network performance a scenario was simulated in Netbas. The network configuration is described in subsection 4.4.2, and all hydro generators are seen upon as inactive. The case considers an extreme conductor temperature of T = 80° in order to represent a hot summer day. The load is scaled as described earlier. If the factory load is shaved as in the average case for June, the line loading is reduced by approximately 2 %. This shows that although the effect is limited, the solar plant has the possibility to reduce the main feeder loading during high production days. It is worth noting that during hot summer days where conductor temperatures are high, a PV system is likely to have high production if the weather is clear. As expected from the results in figure 6.1, the relieving ability is lower in the other months.

A hypothetical scenario where the installed PV capacity is equal to wind (10 MW), is considered in order to compare outputs. This can quantify the effect of several industrial, or residential customers, implementing PV systems. In this case, the average production in the 9am to 3 pm period in June amounts to 3.5 MW. This would relieve the main 66 kV feeder by approximately 10 %, which is a considerable relieving capacity. Again, for the other months, the production compared to June would be the same as that shown in figure 6.1. It can be argued equal rated powers is an unfair comparison, due to the fact that wind turbines can output close to rated power, while PV systems can not.

6.1.2 The Effect of Large Scale Wind

First, the network strength at the point of coupling for the wind farm is discovered. This will give an indication on the voltage effects that can be expected from wind farm injections. The network strength at the proposed point of coupling is quantified through the short circuit ratio described in subsection 2.3.6. The relation between short circuit capacity (S_k) and rated power injections in the coupling point (P_r) gives us this ratio. The combined rated power of the wind turbines is 9.9 MW, and the short circuit capacity at the point is found to be 223 MVA. In order to get a more exact value for S_k the network from the nearest central network station was considered, which limits the effect of a nearby slack bus on results. The short circuit ratio was found to be:

$$\frac{S_k}{P_r} = \frac{223}{9.9} = 22.5$$

As described in subsection 2.3.6, a network with a short circuit ratio below 25 is considered weak. This means that the network probably is susceptible to voltage changes due to wind farm injections, this does however also depend in the network impedance angle (γ) . In order to quantify the voltage increase from the wind plant, the voltage increment is measured with the wind power plant injecting rated power. This is done at 0.95 inductive, unity and 0.95 capacitive power factor. The wind power plant is modeled as a simple PQ source, supplying active and reactive power. The results are shown in figure 6.2. It is assumed that the wind turbine is compensated to give the resulting pf in each scenario, thus outputting rated active power.

Table 6.2: Voltage increment as an effect of a wind power plant injecting 9.9 MW of power at different power factors, during heavy load.

P	Q	Power factor	Voltage increment [%]
9.9	-3.254	0.95 (inductive)	0.23
9.9	0	Unity	1.5
9.9	3.254	0.95 (capacitive)	2.7

The voltage increment was found to be highest during heavy load conditions. In order to keep the voltage increment at zero, it is found that an injection at approximately 0.90 inductive pf is necessary at rated power. Thus if the requirement of the wind farm is to maintain zero voltage increment, equivalent compensation must be provided. This corresponds to a reactive power injection of -0.44 Q/P at rated power.

To quantify if the wind turbines have the possibility to relieve the power system at Senja, simulations in Netbas are performed. Again, the wind power plant is modeled as a PQ-bus. The prerequisites for the scenario is described

in subsection 4.4.2. The load scaling is 80 % in this case as well. As mentioned, the wind farm will be simulated to have the outputs described in subsection 4.4.2. The resulting load of the main 66 kV feeder in % of max capacity, is shown in table 6.3.

Table 6.3: The main feeder load measured in % of maximal capacity with different wind farm injections.

Power Injection [MW]	Main Feeder Load [%]
9.9	110
7.425	115
4.95	120
2.475	125
0	130

If the wind farm injects power at rated capacity, the main feeder load is reduced from 130 % to 110 %. Thus the wind farm possess a good potential for relieving the main feeder during high winds. With lower wind speeds and power outputs, the released capacity is lower. However, a power production 1/4 of rated power reduce the line load by about 5 %. Based on these observations it is clear that the wind farm can release the main feeder by a considerable amount during heavy load conditions. However, the line would still be loaded above its capacity, and thus high load conditions cannot be supplied with zero hydro production in todays network, even with the addition of wind power.

Obviously, it is not guaranteed that the wind plant outputs power when needed either. Figure 5.7 shows the average daily profile for each quarter during the year. From this figure, it can be seen that the average daily profile has a power rating in between the 2.475 and 7.425 MW scenario. Thus, the wind farm will release a considerable amount of capacity on average. Nevertheless, the wind resource varies considerably and at times there will be no production. The periods of low wind production coupled with no hydro production will overload the network. It is argued in subsection 6.2.3 that some sort of support agreement with the hydro power plants could become necessary in the future. The addition of a wind power plant could mean that the amount of support needed could be reduced, restricting the support requirement to periods with low winds. Despite the fact that wind power would not provide a solution for the worst case scenario if there is no wind, it is clear that the addition of the wind farm would have a positive impact on the performance of the power system at Senja. In order to quantify the amount of hydro production needed to keep the line from becoming overloaded under the given wind production scenarios, simulations were performed in Netbas. The results are shown in table 6.4.

Table 6.4: The amount of hydro production needed to keep the main 66 kV feeder from being overloaded during heavy load with the addition of the factory.

Wind Power Injection [MW]	Hydro Power Injection [MVA]	Main Feeder Load [%]
9.9	4.76 (2.30 + j4.11)	99
7.425	5.67 (4.70 + j3.02)	99
4.95	7.06 (6.70 + j2.22)	99
2.475	9.80 (9.70 + j1.19)	99
0	12.31 (12.30 + j0.46)	99

Table 6.4 shows that for high wind production the required hydro production is low. The reactive power output is higher in the high wind scenarios, due to generator excitation. With zero wind production, about 78 % of the installed hydro power needs to be active in order to prevent line over-loading. In the two lowest wind production cases considered, this number is lowered to 43 and 62 % respectively. In the two high production cases 15 and 30 % of the installed active power capability from hydro is required. In other words, scenarios with wind present could potentially reduce the required hydro output substantially. The hydro production in this case was evenly distributed in the two largest plants Bergsbotn and Lysbotn, and the results are are meant as an illustration of the relieving capability of the wind turbines. The relation between active and reactive production could prove to be different for scenarios where the hydro production is distributed differently between the power plants.

Compared to the hypothetical 10 MW PV system, the wind farm will on average contribute a larger relieving ability. This is obvious just from observing the capacity factors observed in chapter 5. If the same 9 am to 3 pm period is considered for the average daily profile for June, the wind power plant outputs an average of 6.2 MW, which is higher than for PV. If the two are combined, it can be concluded that the relieving ability is good on average in months with both high wind production and PV. In this average case for June the main feeder loading would be reduced by about 20 %. Again, especially for wind, the average daily profile for a month does not show the large daily variability. Thus results for each individual day will vary greatly.

6.2 Effect of Power Flow Control on Network Performance

The long outreach of the radial distribution network at northern Senja, coupled with unnecessary reactive currents causes high losses and poor voltage regulation. Increased industrial activity will generate even higher active and reactive power demand, thus measures to increase performance are simulated. In the simulations, network components meant to enhance performance is built into the network. As described in subsection 4.4.3, SCC and BESS are considered. All assumptions and prerequisites are defined and explained in subsection 4.4.3. Figure 6.2 shows the present day average voltage profile between the network substation at Svanelvmoen and Husøy, during normal operating conditions. The voltage profile for this distance is evaluated in all simulations.

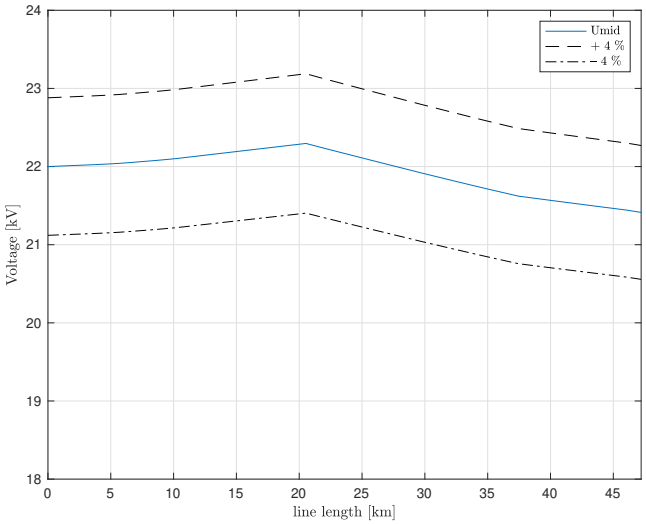

Figure 6.2: The average voltage profile between Svanelvmoen and Husøy in todays network.

The dotted lines represent a deviation of ±4 % from the medial voltage. These limits are used in todays network in order to formulate a voltage range which is adequate for maintaining customer voltage within the regulations formulated in subsection 2.1.6. For a given load increase, the new maximal load voltage profile should be within these limits. It is found that in the extreme locations in the network, the network strength is limited with I_{kmin} as low as 500 A, which should make the voltage sensitive to load additions. This means that connection of new loads, such as new industrial equipment might cause considerable changes to the voltage profile. In subsection 4.4.3 four different load scenarios are presented. To provide a reference for further simulations,

the voltage profile under these four load scenarios is simulated with todays network configuration. The result is shown in figure 6.3.

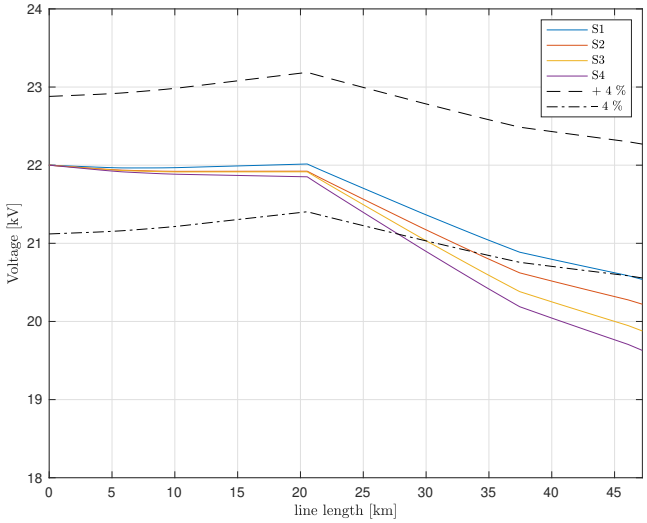

Figure 6.3: The voltage profile between Svanelvmoen and Husøy for S1-S4 with todays network configuration.

The sending and receiving end voltage, as well as voltage regulation is summarized in table 6.5. The network real power losses in these scenarios are also kept for future reference. Power losses are calculated for the radial branch that supply Husøya and surrounding areas with power, meaning that other radial feeders in the substation are disconnected. The percentage shown for power losses is P_{loss}/P_{load}. Since the hydro plant delivers 5.3 MW in all scenarios, a larger amount has to be transported out of the network in scenarios with lower loads. This is the reason the percentage wise power losses are slightly higher in example wise scenario 1.

Table 6.5: Sending end voltage (V_S), recieving end voltage (V_R) and voltage regulation for power supply to Husøy under scenarios 1 through 4.

	V_S [kV]	V_R [kV]	Voltage regulation [%]	P_L [kW]
S1	22.000	20.538	-6.6	332.9 (9.21 %)
S2	22.000	20.211	-8.0	362.8 (8.91 %)
S3	22.000	19.751	-10.2	431.8 (9.47 %)
S4	22.000	19.497	-11.4	480.8 (10.00 %)

Figure 6.3 and table 6.5 clearly show that only S1 falls within the permissible deviation from todays U_{mid}. In S2 a voltage drop of less than 10 % is achieved, but the deviation exceeds - 4% from U_{mid}. S3 and S4 has even poorer voltage

regulation. Thus none of the load increases fulfill the requirements opposed by the network operator. Based on these observations, the need for measures to maintain adequate voltage levels is obvious, if the network loading increases as suggested. Increasing the cross sectional area of the main feeder would off course improve voltage regulation through lower impedance and increased network strength. However, if measures can be initiated in the present network that restricts investment costs it would be preferable as new transmission lines are costly.

6.2.1 The Effect of Shunt Capacitor Compensation

In order to keep the voltage within acceptable limits with increasing demand, a network configuration featuring shunt capacitor compensation (see subsection 2.1.2) is simulated. The allocation problem was solved using the method explained in subsection 4.4.3, and resulted in the following for S1-S4:

Table 6.6: Optimal sizing and placement of capacitors during S1-S4 for the radial feeder supplying Husøy.

	Q_{total} [kvar]	Q_{end} [%]	Position 1	Position 2	Size [kvar]
S1	1320.3	30.9	0.579	1	528
S2	1637.7	29.2	0.565	1	655
S3	2123.4	29.8	0.570	1	849
S4	2423.5	29.7	0.569	1	969

One of the above configurations is chosen for simulations. The configuration for S3 rounded to the nearest 100 kvar is chosen. This is in order to assess the performance of a system that can be implemented in todays network, without being over dimensioned. Other configurations could have been chosen as well, but this configuration is kept for the remainder of simulations. As explained in subsection 4.4.3, SCC will also be implemented at other industrial loads in the network for pf correction. The resulting configuration which is implemented in the network is shown in table 6.7. The placement is also shown visually in figure 6.4.

Table 6.7: Placement and sizing of the preferred shunt capacitor configuration

Location	Radial length [km]	Size [kvar]
Lysbotn	25.4	800
Botnhamn	41.8	300
Husøy	47.2	800

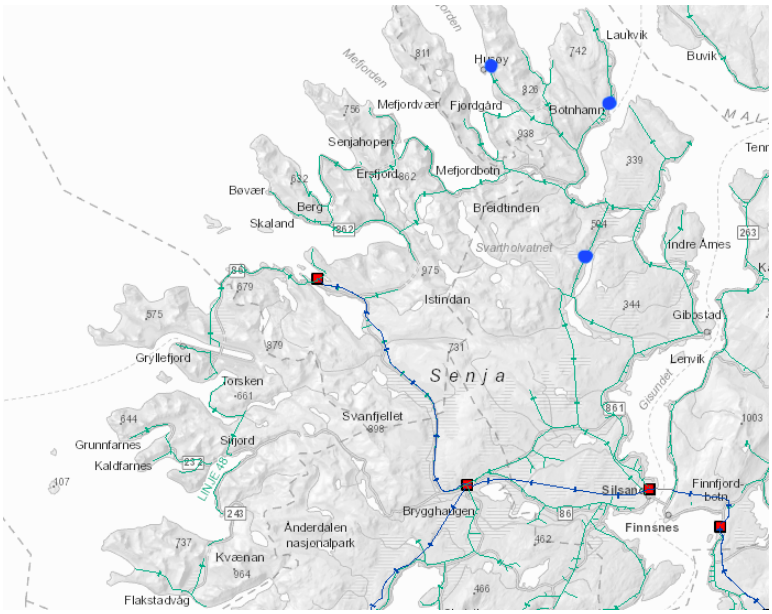

Figure 6.4: The placement of shunt capacitor banks in the distribution network, the capacitors are displayed as blue dots in the network.

Based on observations in subsection 2.1.4, the configuration should be ideal for voltage regulation, as it has good compensation at points far into the network. The allocation method of the main feeder capacitors seeks to minimize losses, hence we would also expect the configuration to reduce system losses (see subsection 6.2.4). The capacitors contribute a total of 1.9 Mvar of compensation, and throughout simulations on voltage performance, the capacitors will deliver full output. This is done to provide comparable results for all scenarios. The voltage profile including SCC between the network substation and Husøy is shown in figure 6.5.

The voltage regulation, as well as system active power losses for this configuration, is shown in table 6.8.

Table 6.8: Sending end voltage (V_S), recieving end voltage (V_R) and voltage regulation for power supply to Husøy under scenarios 1 through 4 with shunt capacitor compensation.

	V_S [kV]	V_R [kV]	Voltage regulation [%]	P_L [kW]
S1	22.000	21.316	-3.1	292.1 (8.08 %)
S2	22.000	21.044	-4.3	315.2 (7.74 %)
S3	22.000	20.571	-6.5	371.1 (8.14 %)
S4	22.000	20.325	-7.6	411.6 (8.562 %)

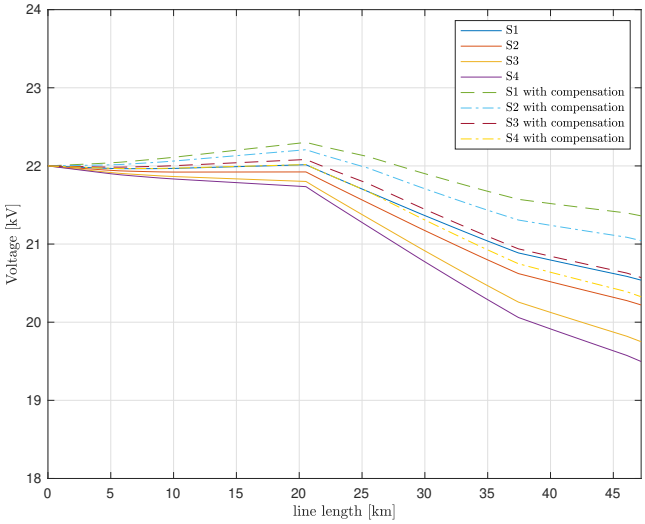

Figure 6.5: The effect of 1.9 MVar of shunt capacitor compensation on the voltage at Husøy. S1-4 is plotted against the uncompensated voltage profiles.

If voltage regulation in table 6.8 and 6.5 is compared, it is found that the average voltage drop has been reduced by 40.6 %, which is equivalent to a 4.1 % average increase of V_R. This shows that reactive power flow control, is well suited for improving voltage regulation in long distribution feeders. The losses shown in table 6.8 are also lower compared to 6.5, implying that the compensation also manage to limit reactive currents in network. The power losses for all four scenarios was reduced by 54.6 kW on average, which amounts to a reduction of 13.6 %. As mentioned, the capacitor rating is not tuned for each individual load scenario in order to keep the voltage regulation assessment consistent. Thus, the optimal capacitor stepping might be slightly different for each load scenario, yielding a slightly different result.

As already stated, SCC greatly improve the voltage regulation, and can thus be justified as a viable option for increasing the reliability of the network during heavy loads. The placement and sizing is meant to minimize system losses, and as mentioned, a considerable reduction in losses is obtained during all scenarios. In subsection 2.1.4 it is mentioned that in order to maximize the voltage regulation improvement, all compensation should be performed at the feeder endpoint. Thus, if voltage regulation is to be weighted more heavily, more of the installed capacity should be placed at the feeder endpoint.

As the installed capacity has a considerable impact on network voltage, it is suggested that capacitors should be able to implement several smaller steps. This will both enable more optimized operation concerning power losses, as

well smoother voltage characteristics.

6.2.2 The Effect of Battery Energy Storage Systems

As discussed in subsection 4.4.3 the utilization of industrial size BESS is considered as a mean to improve voltage regulation by decreasing peak power demand at Husøy. First, an appropriate system is found. It was defined that the system should be able to run with a utilization factor above 0.85 at heavy load, meaning that the battery would never discharge fully in a discharge cycle at this uf. Based on the arguments described in subsection 4.4.3, the following set up was used:

Table 6.9: The performance parameters of the BESS, including the minimum SOC considered in simulations.

Chemistry	Capacity [kWh]	SOC_{min} [%]	P_{max} [kW]	η [%]
Li-Ion	3000	20	± 400	90

Evaluation of battery chemistries is not in the scope of this thesis, and could thus have been chosen arbitrarily. As Li-ion is the most used chemistry for peak shaving applications, it is assumed this technology is used, with a typical Li-ion efficiency (see section 2.4). Effectively, the battery has 2400 kWh of storage, as it is favorable to limit the DoD as it limits battery cycle life. In simulations BESS is only considered as an addition to SCC. This is due to energy marked restrictions mentioned in section 2.4, which states that peak shaving is only allowed for network customers. Thus only the effect of industrial establishments incorporating the technology, as an addition to the SCC installed in the network, is considered. In order to quantify the effect of peak shaving, the algorithm is run for a 10 day period featuring the peak load days of the data presented in subsection 4.2.2. The data is scaled according to scenarios 1 through 4, and the amount of load shaved is calculated. Figure 6.6 shows the industrial load profile at Husøy during S4 load conditions, along with the new load profile due to the storage system.

As described in appendix C, the battery utilization factor has to be optimized for each scenario based on load prognoses. In table 6.10 the amount of load shaved, and utilization factor of the battery is shown. The plot clearly show that the new load profile has a considerably more even structure, reducing the rapidness of fluctuations. Thus does such systems not only contribute lower peak demands with higher peak demand voltages, they also reduce the extent of fluctuations which contributes better overall power quality.

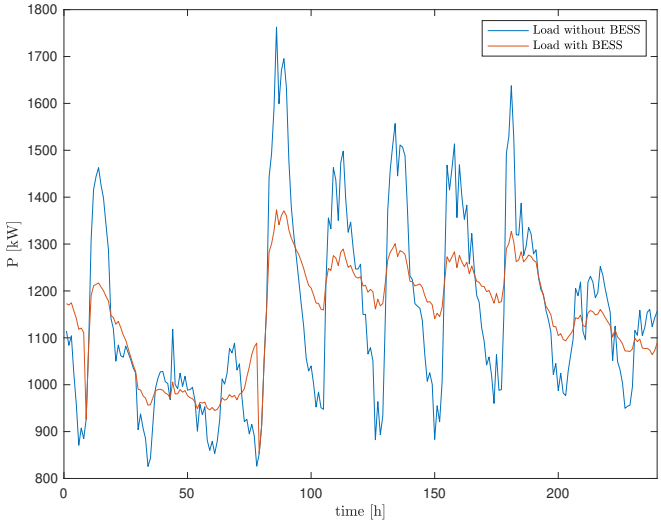

Figure 6.6: S4 industrial load at Husøya, with and without energy storage. The BESS is 400 kW 3000 kWh, with $\eta = 0.90$. The peak shaving algorithm uses a utilization factor of 0.865 in this scenario.

Table 6.10: Peak load shaving of the industrial load at Husøy during S1-4. P_L is the peak load.

Scenario	P_L [kW]	P_L w/ BESS [kW]	Load shaved [kW]	uf
1 & 2	1175	880	295	1
3	1528	1154	374	0.97
4	1763	1373	390	0.865

On average, the peak load is shaved by 23.9 %. In other words such a system has the capability to reduce the peak load quite substantially. As the battery is connected through power electronics to the AC side of the network, the system also has the capability to deliver reactive power. In simulations, this effect is used to keep the power factor at the nominal value. The industrial loads at Husøy are modeled with a pf of 0.95, and thus power injections are performed so that this power factor is conserved. The equivalent power injections on the AC side is shown in table 6.11.

Table 6.11: AC side injections from the BESS during peak load conditions for S1-S4 used in Netbas simulations

Scenario	S [kVA]	P [kW]	Q [kVar]
1 & 2	295	280.3	92.1
3	374	355.3	116.8
4	390	370.5	121.8

As described, injections are kept at nominal pf. It is possible that injections to provide a better load pf would provide better voltage regulation. However, the reduced pf of injected battery power implies that the reduction of active load power would decrease. Poor pf injections would cause lower economical gain for the owner of the battery, since they pay for active power. Thus, ideally, the battery owner would want to retrieve as much active power as possible from the battery system, meaning they would inject at unity pf. But as described, in this thesis the injections are done at the nominal load pf. The resulting voltage profile during scenarios 1 through 4 with shunt capacitor compensation and BESS is shown in figure 6.7.

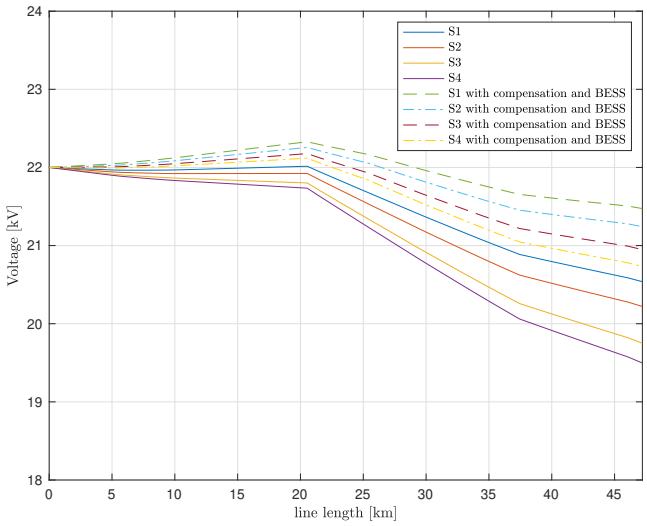

Figure 6.7: The effect of 1.9 MVar shunt capacitor compensation and a 3000 kWh BESS on the voltage at Husøy. S1-4 is plotted against the uncompensated voltage profile.

Again, the voltage regulation of the line with this configuration, is shown in table 6.12. The active power losses are also presented.

Table 6.12: Sending end voltage (V_S), recieving end voltage (V_R), voltage regulation and active power losses during scenarios 1 through 4 with shunt capacitor compensation and BESS.

	V_S [kV]	V_R [kV]	Voltage regulation [%]	P_L [kW]
S1	22.000	21.473	-2.4	273.4 (8.202 %)
S2	22.000	21.241	-3.5	293.5 (7.74 %)
S3	22.000	20.948	-4.9	325.4 (7.74 %)
S4	22.000	20.729	-5.8	354.6 (7.99 %)

Comparing the results from table 6.12 and 6.8, we can see that including the

BESS improves the voltage regulation of the network even further. Compared to the reference case, the voltage drop is on average reduced by 54.1 % in S1-S4, which corresponds to the receiving end voltage being 5.5 % higher on average. Compared to the network configuration installed with compensators only, the voltage drop reduced an additional 13.5 % relative to the reference case. This in turn corresponds to V_R being 1.4 % higher on average than if no BESS is installed.

V_R is well above the defined voltage limits from the reference case. Even in S4, V_R maintains a satisfactory value. With this network configuration, it is evident that the network is able to handle a considerable heavier load before the voltage reaches problematic values. Losses are reduced, but contributes a greater loss percentage in the lowest load scenarios, mainly due to reduced demand as a result of battery injections. Battery utilization is an energy neutral process, thus the same amount of energy has to be delivered over time. Line losses does however depend on line current squared, thus overall system losses are still reduced.

The implementation of BESS at industrial applications, will from the results above, be able to increase the performance of the system. During heavy loading, both voltage and losses will be reduced. Wether the peak shaving application is the best use of a BESS in distribution networks, is a question open for debate. In this specific case, the need for peak load reduction is imminent, and as such the application can be justified. As discussed in section 2.4, BESS are also suitable for high power low energy applications. Increased network performance could thus also be obtained by a storage system that smoothens rapid load fluctuations, with a much lower requirement for energy. However this would not enable greatly reduced peak loads.

6.2.3 The Effect of Limited Hydro Production

As mentioned, the operation of Lysbotn power plant is based upon optimal economical dispatch. If the power plant continues to be operated according to this principle, the network operator can not expect the power plant to produce the desired amount of power for a given load condition. In order to assess the robustness of the suggested network configuration, and to discover how it performs during low hydro production, a scenario with limited hydro production is considered. The amount of production during this scenario was chosen to be 1.75 MW, based on the production in the first quarter of 2018 (see figure 4.4). The generator is operated as a PV-bus in this case as well, with the voltage being kept at its nominal value of V = 6.6 kV. The voltage characteristics during these conditions in todays network is shown in table 6.13.

Table 6.13: V_S, V_R, voltage regulation and active power losses in todays network during 1.75 MW hydro production at 6.6 kV in S1-S4.

Load scenario	V_S [kV]	V_R [kV]	Voltage regulation [%]	P_L [kW]
S1	22.000	20.044	-8.9	288.8 (7.99 %)
S2	22.000	19.704	-10.4	386.4 (9.49 %)
S3	22.000	19.190	-12.8	544.9 (11.95 %)
S4	22.000	18.912	-14.0	643.8 (13.39 %)

The results displayed above, shows that the voltage regulation compared to the results from table 6.5 is poorer. This is also expected, due to the increased amount of power flow in transmission lines needed to meet demands. Figure 6.8 shows the the resulting profile for S1-S4 for both todays network and with the addition of the same SCC considered earlier in this section.

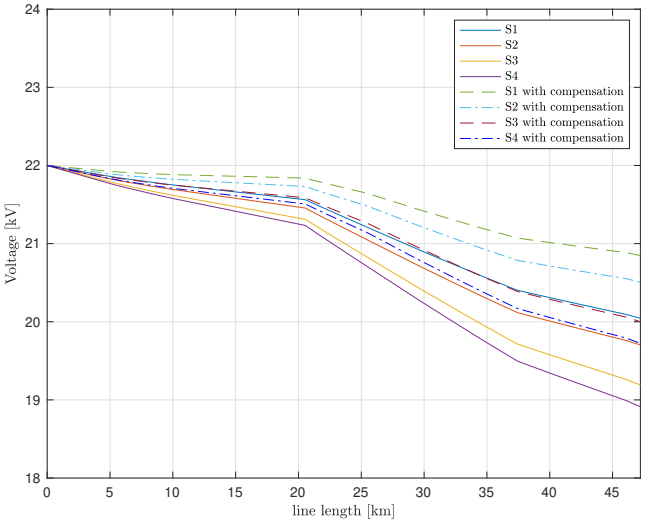

Figure 6.8: The effect of 1.9 MVar shunt capacitor compensation on the voltage between Svanelvmoen and Husøy in the case of low hydro production. The resulting profile for the uncompensated network is shown as reference.

The resulting voltage characteristics with the addition of compensation is shown in table 6.14.

Table 6.14: V_S, V_R, voltage regulation and active power losses with SCC built into the network during 1.75 MW hydro production at 6.6 kV in S1-S4.

Load scenario	V_S [kV]	V_R [kV]	Voltage regulation [%]	P_L [kW]
S1	22.000	20.848	-5.2	290.6 (8.04 %)
S2	22.000	20.507	-6.8	379.1 (9.31 %)
S3	22.000	20.000	-9.1	519.0 (11.38 %)
S4	22.000	19.725	-10.3	606.3 (12.61 %)

Comparing the results from table 6.13 and 6.14 shows a 31.9 % improvement in average voltage regulation with SCC installed. This is a lower improvement compared to the high production case. This is as expected, due to less injection from the hydro plant causing higher power flows through the full length of the radial network. This causes higher IZ_L voltage drops. Thus the phase angle shift from the reactive power compensation will contribute a smaller percentage-wise improvement. In addition, the hydro generator exciter injects considerable amounts of reactive power to maintain terminal voltage, thus the addition of the compensation contributes a smaller percentage of total injected reactive power as well. In the reference case, the injected reactive power from the hydro plant is in the range 1.5-2-5 Mvar.

It can be observed that active power losses also are reduced, but less than in the high production case. The average losses for S1-S4 are reduced by 17.225 kW which amounts to 3.7 %. Again, this is due to the already considerable reactive power injections from the hydro generator. It can be clearly seen that losses are reduced most during the heavier load scenarios. It is important to keep in mind that the shunt capacitors inject their maximal reactive power during all scenarios. If the configuration most suited for S1 is applied for example, network losses of 7.791 % is achieved, which is a more pleasing value than the value obtained for the uncompensated configuration in table 6.13.

The addition of the 3000 kWh battery at Husøy is also simulated, and the resulting voltage is shown in figure 6.9. The resulting voltage and loss characteristics with the addition of SCC and BESS is shown in table 6.16.

Table 6.15: V_S, V_R and voltage regulation in todays network during 1.75 MW hydro production at 6.6 kV in S1-S4.

Load scenario	V_S [kV]	V_R [kV]	Voltage regulation [%]	P_L [kW]
S1	22.000	20.953	-4.8	254.1 (7.62 %)
S2	22.000	20.704	-5.9	323.8 (8.54 %)
S3	22.000	20.399	-7.3	410.8 (9.77 %)
S4	22.000	20.159	-8.4	477.0 (10.75 %)

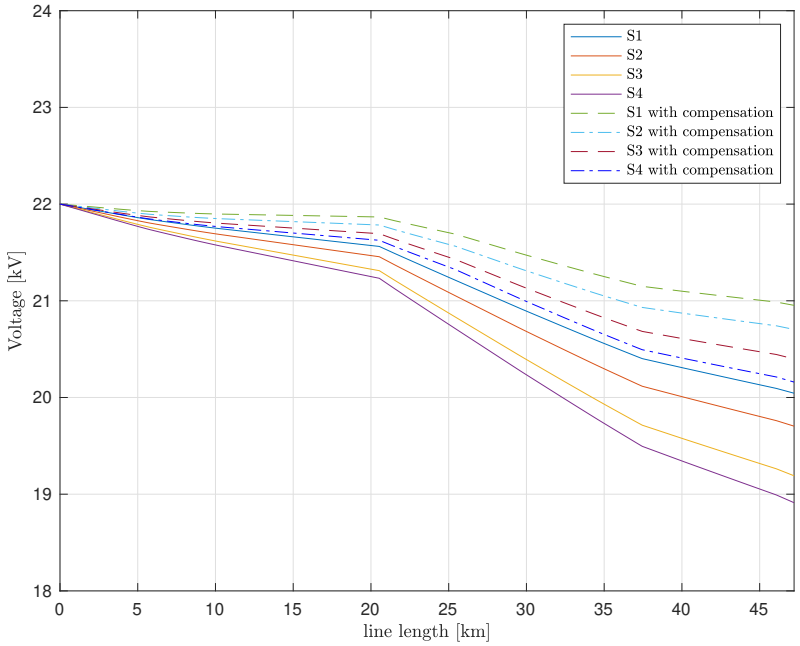

Figure 6.9: The effect of 1.9 MVAr shunt capacitor compensation and a BESS on the voltage between Svanelvmoen and HUsøy during low hydro production. The profile in the uncompensated network is plotted as reference.

As we can see from table 6.16, voltage regulation is improved. The improvement of voltage regulation compared to the reference case is 42.7 % on average through S1-S4. Again, the percentage wise improvement is lower than in the high production case. Compared to the SCC configuration, the average voltage drop is reduced by 15.9 %. This is a better improvement than in the high production case, indicating that limiting peak load is more effective for controlling voltage when synchronous production is low. The peak power losses are reduced substantially, with a reduction of 18.3 %. This of course comes from the fact that the demand is reduced as a function of the shaved peak load. Note however, that as mentioned, the power loss dependency on line current squared implies that overall losses are reduced in this case as well.

An analysis of the performance of the network during zero hydro production was also performed. This was done to discover whether the suggested network configuration can provide adequate voltage performance during high load hours, even when there is no support from the power plant. The resulting performance for all configurations is shown in table 6.16.

Table 6.16: V_S, V_R and active power losses for all configurations, with inactive hydro power plant for S1-S4. Voltage regulation is shown in the parenthesis.

	V_S [kV]	V_R SCC/BESS [kV]	V_R SCC [kV]	V_R ref [kV]
S1	22.000	20.022 (-7.9 %)	19.863 (-9.7 %)	18.679 (-15.1 %)
S2	22.000	19.607 (-9.8 %)	19.300 (-12.3 %)	18.105 (-17.7 %)
S3	22.000	19.113 (-12.1 %)	18.453 (-16.1 %)	17.230 (-21.7 %)
S4	22.000	18.714 (-13.9 %)	17.968 (-18.3 %)	16.772 (-23.8 %)

	P_L SCC/BESS [kW]	P_L SCC [kW]	P_L ref [kW]
S1	389.5 (11.68 %)	440.7 (12.19 %)	497.8 (13.77 %)
S2	487.2 (12.85 %)	565.2 (13.88 %)	661.3 (16.24 %)
S3	611.7 (14.54 %)	772.9 (16.95 %)	938.0 (20.57 %)
S4	709.1 (15.98 %)	910.6 (18.94 %)	1122.2 (23.34 %)

It can be read from table 6.16 that the voltage regulation is improved drastically in this case as well. The average improvement in voltage regulation amounts to 28.0 % and 44.2 % for the SCC configuration and the SCC and BESS configuration respectively. This amounts to an average increase in receiving end voltage of 6.8 % and 9.4 %. The increased robustness due to the active and reactive power compensation applied, will demand far less stepping of transformers, in order to achieve desired voltage. If the need for transformer stepping is reduced, phenomena such as over-voltages and general voltage instability are also reduced. With no support from synchronous generation, table 6.16 clearly shows that losses are reduced substantially with the addition of SCC and BESS. For the SCC configuration, the average loss reduction in S1-S4 amount to 16.5 %. For the configuration with BESS added, the corresponding number becomes 31.2 %. Again, the line power flow is also lower in this case due to the peak shaving.

Despite enabling better voltage regulation with the addition of SCC and BESS the regulation is still quite poor, especially in the higher load scenarios. This implies that it would be beneficial to impose a constraint on the hydro power plant, not enabling it to have zero production during the maximal load periods. Alternatively, a compensator configuration for improved voltage control can be considered. As discussed, this would mean placing all the compensation at the feeder end point, as this provides the best voltage improvement. However, this would not be economically beneficial concerning active power losses.

It is interesting to note that with the support of hydro, voltage regulation can be kept within acceptable limits even for the extreme load scenario. Problems does only occur when the hydro power plant has limited output. If the

hydro power plant should be constrained as discussed, the reserves that have to be kept, would also be drastically reduced with the compensation proposed in the network.

6.2.4 Detailed Yearly Analysis

In order to assess the network performance over a full year, a detailed analysis was performed. In this analysis, the network configuration is chosen to be the one featuring SCC. This is due to the difficulty og implementing batteries in the detailed analysis function inside of Netbas (see subsection 4.4.3). As mentioned, this function does not allow much flexibility in how the capacitors are operated, other than that they can be used for *voltage regulation*. It is stated that the software seek to find the optimal operation of capacitors in each time step, to provide optimal performance. In subsection 4.4.3, three different capacitor bank configurations are presented. Systems with 1, 5 and 10 steps are considered. Other than the difference in steps, the SCC configuration is the same. The resulting yearly statistics for the configurations in table 4.8 is shown in table 6.17. The simulations are run for S1, in order to present yields in the present demand pattern.

Table 6.17: Yearly losses for different configurations of shunt capacitor banks. Demand is sized as in S1. Reduction quantifies the savings compared to the uncompensated configuration.

Scenario	Load [MWh]	Losses [MWh]	Losses [%]	Reduction [MWh]
1	19272.03	2196.77	11.399	-
2	19272.03	2031.66	10.542	165.11
3	19272.03	2007.20	10.415	189.57
4	19272.03	2001.49	10.385	195.28

As table 6.17 clearly shows, the yearly losses are reduced quite substantially with the addition of the shunt capacitors. It can be argued that the configuration with 5 steps would be the optimal configuration. It would provide several steps, such that the voltage and losses can be controlled satisfactory. Table 6.17 shows only little improvement in yearly losses between the 10 and 5 step configuration, meaning that only little gain is obtainable from the increased complexity. The 5 step configuration is examined further in S2-S4 in order to assess the possible savings if the demand increases as suggested in the scenarios. Table 6.18 shows the results, where the reduction quantifies the saved losses over a network without capacitors.

Table 6.18: Yearly losses for a 5 step configuration, with savings relative to an uncompensated network.

	Load [MWh]	Losses [MWh]	Losses [%]	Reduction [MWh]
S2	21709.88	2028.92	9.346	202.49
S3	24058.09	2127.86	8.845	231.68
S4	25208.64	2202.33	8.736	250.92

As table 6.18 shows, the yearly energy savings is subject to an increase with increasing demand. The load increase considered is uniform for the whole year, which might not give an exact result. Nevertheless, increasing energy savings is a clear trend with increasing demand. This implies that if SCC is installed in the network, and the predicted demand increase occurs, savings will also be improved.

6.3 Sources of Error

As for the previous chapter, the sources of error related to the renewable energy systems also apply in this chapter. Which could mean that during real conditions, the results would be different from the ones obtained in this work.

In the network analysis, the slack bus assumption of the network station is a source of error. In real conditions, the voltage at the substation can be both lower and higher than the nominal value, which would have an impact on the voltages at other nodes in the network. The load scenarios are also uncertain. However, the load scenarios are only meant as a suggestion on load development.

As mentioned in subsection 4.4.3, Netbas does not explicitly state the operational regime of the shunt capacitors in the yearly analysis. Thus some uncertainty related to the operational regime, and wether this is truly optimal, is present.

7

Conclusion and Further Work

7.1 Summary

In this study the effect of power flow control and renewable production on power system performance has been simulated at Senja in northern Norway. A small wind farm and industrial scale PV rooftop system has been simulated, and the potential yield has been quantified (Chapter 5). An analysis was performed to evaluate the potential the renewable energy systems have on network performance (Chapter 6). This has been quantified through released transfer capacity. The performance of SCC and BESS on distribution network performance has also been evaluated (Chapter 6).

It was found that the potential for wind power was good at the location considered, yielding a capacity factor of about 39 %. This equates to an average power output of about 3.9 MW for the 9.9 MW system. Thus a wind farm at the location is deemed sustainable based on potential energy output. Inspecting the yearly variations in wind, it was found that the wind on average was most stable in the winter months, which correlates well with peak demand periods. As the effect of turbulence and wake losses was not included in the initial simulations, approximation of these losses was part of a sensitivity analysis. It was found that with turbine losses resembling high turbulence, a capacity factor of above 30 % was still obtained.

Based on the rated power of the wind farm, it was found that it had good potential for releasing network capacity. About 1/5 of the island's main feeder capacity was released at rated power. The released capacity was also quantified during lower production scenarios, and the the resulting capacity release was also considerable. Meaning that even during low production scenarios, considerable fractions of main feeder capacity is released. Voltage increments due to wind farm injections was found to be limited, despite the network having a SCR on the low side. A reactive power compensation of approximately -0.4 Q/P was needed to ensure zero voltage increment at rated power.

An east/west configuration was chosen for the industrial solar system, after a comparison with a south facing system. The decision was made due to the increased installed capacity and specific energy yield. The monthly potential for the system was quantified, and the results was promising in summer months. It was found that the system could provide about 1/10 of the total factory consumption during peak production days. Quarter two and three was found to be the the periods that had a somewhat noticeable impact compared to factory consumption. The released capacity of the island's main feeder was however found to be small. In the peak production days, the feeder load could be reduced by about 2 %. An upscaling of the PV system to 10 MW was performed in order to compare it to the wind system. It was found that with this amount of installed PV capacity, the main feeder could be relieved by up to 1/10 at daytime during summer. Although not as substantial as the possible wind power relieving ability, it would make a considerable contribution.

Allocation of SCC and BESS along the main feeder in a radial distribution network was considered. The effects was simulated, and found to be promising. Reactive power flow control by shunt capacitors was found to reduce reactive currents considerably, thus reducing the voltage drops in the transmission network by 30-50 % on average. Reduction of active current in peak load hours was also simulated through the utilization of a BESS. The shaving capacity of a large scale battery was found to be considerable, and provided a reduction in peak power demand. This was found to additionally improve the voltage regulating performance in the network. A considerable reduction of network losses was also observed in both cases.

The effect of limited hydro production was evaluated, and it was found that SCC and BESS enabled the ability to sustain acceptable voltage regulation for heavier loads. In the extreme case of no hydro production, the performance was drastically improved, but performance was still poor, especially in the extreme load scenarios. The use of SCC was found to reduce network losses considerably over the course of a year, and it was concluded that SCC should inherit a possibility of stepping in order to improve general voltage quality and minimize power losses.

7.2 Concluding Remarks

The objective of this study was to evaluate the effect of power flow control and distributed generation on network performance. In order to quantify the effect of the latter, the yearly potential was simulated. Senja shows a promising potential for harvesting the wind resource, and the solar resource potential is also good in summer months. The effects of the considered components on the network performance, is deemed positive overall. They would both have the ability to release transfer capacity, improve voltage regulation, reduce losses and thus improve over all power quality. In the distribution network, the improvements will enable the network to operate satisfactory, even with considerable increases in peak load patterns. During peak load however, the network requires some support from the hydro power plant.

Despite releasing transfer capacity, the renewable energy sources will not be able to relieve the main 66 kV feeder enough with the addition of the new factory load. During heavy load conditions and zero hydro production, the line will still be overloaded with maximal wind production, which can not be expected when it is needed due to wind variability. This tendency makes it clear that with considerably increased energy demand, transmission upgrades will become necessary. The measures considered in the distribution network, shows the most promising results for postponing investments in transmission capacity.

7.3 Further Work

As described, in order to confine the scope of this thesis, system economics was not considered. This should be included in future work. In order to asses whether the renewable energy systems are feasible, the generated energy should be evaluated with respect to system costs over the course of the system lifetime. A net present value analysis should also be performed on SCC and BESS implementation. In addition, the potential savings from reducing the need for line investments should be quantified. All these analyses has to be performed in order to assure that the implementation of the considered systems is feasible.

The design of a large and interconnected smart power system for Senja, should also be considered as future work, and will be a natural part of the *Smart Infrastructure Senja* project. Here, the interaction between all system components and factors should be considered. This includes smart data assimilation in order to enable better interaction between parts of the system. The assimilated data should be used to control system components such that they

work together, and optimize network performance. The operation of components suggested in this thesis should be implemented in such an operational regime. As for the components discussed in this thesis, especially alternative applications of BESS should be evaluated. For example as load curve or renewable smoothers, which could enhance the stability of network operations. The effect of customer load control should also be evaluated further in such a project. Lastly, large scale implementation of PV systems with the addition of BESS at residential customers would be essential to evaluate.

To conclude, a more active and smart control of distribution systems will become an important feature in the power system of tomorrow. Further study on the topics considered in this thesis, as well as those mentioned in this section, will be important in order to drive technological advances. Ultimately, this will help the shift into a more sustainable and efficient energy infrastructure, suitable for the needs of the future.

A

How HOMER Calculates Production Output

A.1 Solar Time Correction

All derivations given in this appendix are from the HOMER documentation at homerenergy.com [Energy, 2019]. In subsection 2.2.2 a Time Correction was defined. As mentioned, this time correction accounts for the longitudinal differences within each time zone, as well as the excentrity of the earths orbit. This time correction is calculated through the Equation of Time (EOT).

$$\mathrm{EoT} = 9.87\sin(2\mathrm{B}) - 7.53\cos(\mathrm{B}) - 1.5\sin(\mathrm{B}) \tag{A.1}$$

Where

$$\mathrm{B} = \frac{360}{365} \cdot \mathrm{d} \cdot (-81) \tag{A.2}$$

Combining this phenomena with the longitudinal differences within each timezone, gives us a correction factor.

$$\mathrm{TC} = 4(\mathrm{Longitude} - \mathrm{LSTM}) + \mathrm{EoT} \tag{A.3}$$

A.2 Incident Radiation on a Collector Surface

When HOMER calculates the radiation incident on a collector surface, the irradiance data is corrected in accordance with the TC described in appendix A. This transforms the time domain of the irradiance data to LST. The angle of incidence θ defines the angle between radiation and the normal of the collector surface. This angle is given by:

$$\cos\theta = \cos\alpha\cos(\Phi_S - \Phi_C)\sin\beta + \sin\alpha\cos\beta \tag{A.4}$$

Where Φ_S and Φ_C denotes the solar and collector azimuth angles. The relation between GHI (I_{GH}) and extraterrestrial horizontal irradiance (I_{EH}) is known as the clearness index K_T is calculated for each time step. I_{EH} is integrated over each time step, which gives the hourly average extraterrestrial irradiance (I_{EH}).

$$I_{EH} = \int_{\omega_1}^{\omega_2} I_E \sin\alpha = \frac{12}{\pi} I_E \left[\cos\phi\cos\delta\sin\omega + \frac{\pi(\omega)}{180}\sin\phi\sin\delta\right]_{\omega_1}^{\omega_2} \tag{A.5}$$

Where ω_1 and ω_2 are the hour angle at the start and end of the time step and I_E is the extraterrestrial irradiance. The clearness index is calculated in this time step by dividing the GHI by I_{EH}. In subsection 2.2.1 the distinction between direct and diffuse irradiance was explained. HOMER calculates the direct and diffuse fraction from a fourth order expression inputing K_T. The ratio of diffuse irradiance (I_{DIF}) to global irradiance (I_{GH}) is calculated as:

$$\frac{I_{DIF}}{I_{GH}} = \begin{cases} 1.0 - 0.09K_T & \text{for} \quad K_T \leq 0.22 \\ 0.9511 - 0.1604K_T + 4.388K_T^2 - 16.638K_T^3 + 12.336K_T^4 & \text{for} \quad 0.22 < K_T \leq 0.80 \\ 0.165 & \text{for} \quad K_T > 0.80 \end{cases}$$

From calculating the direct and diffuse fractions, the irradiance incident on the collector surface (I_C) can be calculated from (A.6):

$$\begin{aligned} I_C &= (I_{DN} + I_{DIFi})R_b \\ &+ I_{DIF}(1 - A_i)\left(\frac{1+\cos\beta}{2}\right)\left(1 + f\sin^3\left(\frac{\beta}{2}\right)\right) + I_{GH}\rho_r\left(\frac{1-\cos\beta}{2}\right) \end{aligned} \tag{A.6}$$

Where R_b is the ratio of beam radiation on the tilted surface and the horizontal ($^{\cos\theta}/_{\sin\alpha}$), A_i is the anisotropy index ($^{I_{DN}}/_{I_{EH}}$) and f is a horizon brightening factor which is defined as $\sqrt{^{I_{DN}}/_{I_{GH}}}$.

A.3 PV Temperature Calculations

From the energy balance of a PV cell, we can define the expression for cell temperature T_c:

$$T_c = T_a + I_C \left(\frac{\tau\alpha}{U_L}\right)\left(1 - \frac{\eta_c}{\tau\alpha}\right) \tag{A.7}$$

Where τ is the solar transmittance, α solar absorptance, U_L the coefficient of heat transfer and η_c the PV efficiency. T_a is the ambient temperature. The expression $\frac{\tau\alpha}{U_L}$ is then defined in terms of the NOCT, as follows:

$$\frac{\tau\alpha}{U_L} = \frac{T_{c,NOCT} - T_{a,NOCT}}{I_{C,NOCT}} \tag{A.8}$$

Where $T_{c,NOCT}$ is the cell temperature during NOCT, and $T_{a,NOCT}$ is the ambient temperature during such conditions (20°). If this expression is assumed constant, it can be substituted into (A.7). HOMER assumes that the cells are always operated at the maximal power point, thus $\eta_c = \eta_{mp}$.

$$T_c = T_a + I_C \left(\frac{T_{c,NOCT} - T_{a,NOCT}}{I_{C,NOCT}}\right)\left(1 - \frac{\eta_{mp}}{\tau\alpha}\right) \tag{A.9}$$

A value of 0.9 is assumed for $\tau\alpha$. In addition, the cell efficiency is dependent on temperature as well, which gives the following expression for efficiency:

$$\eta_{mp} = \eta_{mp,STC}\left[1 + \alpha_p(T_c - T_{c,STC})\right] \tag{A.10}$$

Where $\eta_{mp,STC}$ is the efficiency during STC, $T_{c,STC}$) is the cell temperature during STC and α_p is the temperature coefficient. If this is substituted into (A.9), we get the final expression for cell temperature:

$$T_c = \frac{T_a + (T_{c,NOCT} - T_{a,NOCT})\left(\frac{I_C}{I_{C,NOCT}}\right)\left(1 - \frac{\eta_{mp,STC}(1-\alpha_p T_{c,STC})}{\tau\alpha}\right)}{1 + (T_{c,NOCT} - T_{a,NOCT})\left(\frac{I_C}{I_{C,NOCT}}\right)\left(\frac{\alpha_p \eta_{mp,STC}}{\tau\alpha}\right)} \tag{A.11}$$

A.4 PV Array Output

If the PV array is chosen to have a temperature dependance, the panel temperature is calculated in accordance to the method described in this appendix. Then the PV array power for each time step is calculated from (A.12):

$$P_{PV} = P_r f_{PV}\left(\frac{I_C}{I_{C,STC}}\right)\left(1 + \alpha_p(T_c - T_{c,STC})\right) \tag{A.12}$$

Where P_r is the rated power of the PV array, f_{PV} is the derating factor and $I_{C,STC}$ and $T_{c,STC}$ is the irradiance and cell temperature during STC. α_p is the temperature coefficient of the PV array. The method described in this section is applied to every time step throughout the year, and thus gives the yearly energy together with power production in each time step.

B

Control of Reactive Power in Distribution Networks

In this thesis the optimal sizing and placement of shunt capacitors is found using the technique proposed by [A. Salama et al., 1985]. The technique determines the optimal sizing and placement along a radial feeder with an end load, for a fixed load condition. This is used to find the sizing needed in the worst case scenario, which has no hydro production. The remainder of the clarifications and methods explained in this appendix is from [A. Salama et al., 1985].

B.1 Equivalent Uniform Feeder Resistance

The idea of an equivalent uniform feeder resistance, is to produce a uniform feeder that produces the same losses as a non uniform one. The uniform feeder resistance can be retrieved from (B.1).

$$\sum_{j=1}^{ns} i_j^2 R_j = \frac{1}{3} I^2 R_{base} \tag{B.1}$$

ns is the number of line segments, while i_j and R_j is the reactive current and resistance in each line segment. I is the total reactive current and R_base is the base resistance. A per unit base for the reactive power also has to be

formulated.

B.2 Peak Power Loss Reduction for Uniform Feeder with End Load

Only reactive loads are considered in this method, hence only reactive currents. In the calculations that follow all quantities are expressed as *per unit values*, which is based on the base values formulated. The peak power losses per phase can be expressed in as:

$$L_{ph} = \int_0^1 [I_1 - (I_1 - I_2)l]^2 \, Rdl \tag{B.2}$$

Where I_1 is the sending en reactive current, and I_2 is the reactive current of the end load. On a per unit base $I_1 = 1.0$ while I_2 is a fraction of I_1. The per unit resistance is $R = 1.0$ while l is the distance from substation, where 1 indicates the end of the feeder. Integrating (B.2) and multiplying by three yields the three phase power losses. If a capacitor with reactive current injection I_C is placed at a distance a along the feeder, the three phase losses become:

$$L_c = \left[\left(1 + I_2 + I_2^2\right) + 3aI_c\left(a(1 - I_2) + I_c - 2\right)\right] \tag{B.3}$$

If (B.3) is subtracted from the three phase losses prior to the installation, the reduction in power losses is found. Differentiate the equation with respect to a to find a_{opt}:

$$a_{opt} = \frac{2 - I_c}{2(1 - I_2)} \tag{B.4}$$

In the case of n capacitors, the reduction in losses become:

$$\Delta L = 3I_c \sum_{m=1}^{n} a_m \left[2 - a_m(1 - I_2) - (2m - 1)I_c\right] \tag{B.5}$$

Optimal locations are again found by differentiating $\frac{\partial \Delta L}{\partial a_m} = 0$, which gives:

$$a_{m,opt} = \frac{2 - (2m - 1)I_c}{2(1 - I_2)} \tag{B.6}$$

In order to find the optimal compensation level, the injected current from capacitors I_c is replaced by $\frac{K}{n}$, where K is the capacitor rating in per unit. If this is inserted into (B.3), and differentiation is performed with respect to K, the optimal placements can be found as $\frac{\partial \Delta L}{\partial K} = 0$:

$$K_{opt} = \frac{4n(n + 1)}{(1 - I_2)(2n + 1)^2} \tag{B.7}$$

B.3 MATLAB Code

The MATLAB code used for solving the allocation problem in this thesis is given below. The equations derived above is formulated directly in the code, and solved to find the optimal placement and size.

```
%% Optimal capacitor placement for uniform feeder %%
n = 2; % number of capacitors
aopt = zeros(n,1);
Kopt = 2*n/(2*n + 1); % Optimal capacitor rating in p.u
Ic = Kopt/n; % Capacitor current
R = 1; % Impedance in p.u
I1 = 1; % Sending end reactive current in p.u
I2 = 0.297 *I1; % Recieving end reactive current in p.u

% System losses with capacitors
Lc = R*((I1 + I2 + I2^2) + 3*a*Ic*(-2 + a*(I1 - I2) +
    Ic));
% Find optimal placement
for i = 1:n
    aopt(i) = (2-(2*i-1)*Ic)/(2*(1-I2));
    if aopt(i) > 1 % Adjust if aopt > 1
        aopt(i) = 1;
    end
end
```

C

Peak Load Shaving using BESS

C.1 The Algorithm

In this appendix, the peak shaving algorithm proposed by [Rahimi et al., 2013] used as an inspiration for the BESS shaving algorithm, is presented. The algorithm seeks to alter the load curve towards the floating average, which has the possibility of drastically reducing peak load values. Average load power of the aggregated load profile (P_{av}) after each time interval (τ) is calculated for the next utilization period (up). This is done to quantify the charge/discharge of the battery for each time interval. The charge/discharge is restricted by the utilization factor (uf), which in this algorithm defines how much of the difference between P_{av} and the actual load curve the BESS should shave. $uf = 1$ tries to shave all load above the moving mean, while $uf = 0$ does not operate. The algorithm proposed in this thesis uses the assumed load profile, and figures the appropriate uf.

In each time step the amount of charged/discharged energy for the battery is found by:

$$|E_{bat}| = (P - P_{av}) \cdot uf \tag{C.1}$$

Where P is the aggregated load for that time step. Thus the battery discharge

power becomes:

$$|P_{bat}| = \eta \frac{|E_{bat}|}{\tau} \tag{C.2}$$

Where η is the BESS efficiency. The power is subject to the constraint of the max charge/discharge power of the battery, and if P_{bat} exceeds this value it is set to be equal to the max power or minimum power. This is shown in (C.3).

$$P_{min} \leq \frac{|P_{bat}|}{\tau} \leq P_{max} \tag{C.3}$$

The second condition is that the state of charge of the batteries must be within the predefined boundaries:

$$SOC_{min} \leq SOC \leq SOC_{max} \tag{C.4}$$

When the uf is to be found, it should be defined as 1 initially. When the algorithm is run for the proposed period, it will be checked for complete discharge in the battery. If complete discharge occurs, the uf will be lowered, and the algorithm run again. This is performed until the appropriate uf is found.

C.2 MATLAB Code

The MATLAB code used during simulations, shows a code that will find the appropriate uf for a 10 day period. The code is shown below:

```
% / PEAK SHAVING ALGORITHM \ %
% / KEY PARAMETERS \ %
up = 24; n = 24; uf = 1;
tau = 1;
SOCmax = 2400; SOCmin = 0; SOC = 0.5*SOCmax; eta = 0.9;
Pmax = 400; Pmin = -400;
% Moving mean for utilization calculation
slidemean = movmean(loadtimeseries1h.Data,up);
% Define start and length of simulation
tstart = 2208;
nsamples = 10*24;
% Initialize
Pbess = zeros(length(slidemean),1);
SOCg = zeros(length(slidemean),1);
SOCp = zeros(length(slidemean),1);

%% CALCULATION OF BESS OPERATION %%
```

```
18
19 P = loadtimeseries1h.Data;
20 Pav = slidemean;
21
22
23
24 k = tstart -1 ;
25 true = 0;
26 i = tstart - 1;
27 while true < 1
28     i = i + 1;
29     br = 0;
30     k = k + 1;
31     Es = (P(i)-Pav(i))*uf;
32     Ebat = Es;
33     Pbat = eta*Ebat/tau;
34     % Check if Ebat exceeds Pmax/min
35     if Ebat > Pmax
36         Pbat = eta*Pmax;
37     elseif Ebat < Pmin
38         Pbat = eta*Pmin;
39     end
40
41     % Calculate State of Charge
42     SOC = SOC+Pbat;
43     SOCg(i) = SOC;
44
45     % Restrict State og Charge
46     if SOC <= SOCmin
47         SOC = SOCmin;
48         Pbat = 0;
49     elseif SOC >= SOCmax
50         SOC = SOCmax;
51         Pbat = 0;
52     end
53
54     % Calculate Power and new state of charge
55     Pbess(i) = Pbat;
56     SOCp(i)  = 1 - SOC/SOCmax;
57     if k == tstart+nsamples
58         if ismember(0,SOCp(tstart:tstart+nsamples)) ==
               1
59             i = tstart-1;
```

```
60              uf = uf -0.01;
61              k = tstart-1;
62              SOC = 0.5*SOCmax;
63              SOCp = zeros(length(slidemean),1);
64              Pbess = zeros(length(slidemean),1);
65              SOCg = zeros(length(slidemean),1);
66          else
67              true = 1;
68          end
69
70      end
71
72  end
73
74  % Calculate new load profile
75  Load_bess1(tstart:tstart+nsamples) = loadtimeseries1h.
      Data(tstart:tstart + nsamples) - Pbess(tstart:tstart
       + nsamples);
```

Bibliography

[A. Salama et al., 1985] A. Salama, M. M., Chikhani, A. Y., and Hackam, R. (1985). Control of reactive power in distribution systems with an end-load and fixed load condition. *IEEE Transactions on Power Apparatus and Systems*, PAS-104(10):2779–2788.

[ABB, 2013] ABB (2013). Power capacitors and harmonic filters.

[Abril and Quintero, 2003] Abril, I. P. and Quintero, J. A. G. (2003). Var compensation by sequential quadratic programming. *IEEE Transactions on Power Systems*, 18(1):36–41.

[AEMO, 2016] AEMO (2016). System stength.

[Alhamali et al., 2016] Alhamali, A., Farrag, M., Bevan, G., and Hepburn, D. (2016). Review of energy storage systems in electric grid and their potential in distribution networks. pages 546–551.

[Aman et al., 2014] Aman, M., Jasmon, G., Bakar, A., Mokhlis, H., and Karimi, M. (2014). Optimum shunt capacitor placement in distribution system—a review and comparative study. *Renewable and Sustainable Energy Reviews*, 30:429 – 439.

[Andreani et al., 2019] Andreani, L. C., Bozzola, A., Kowalczewski, P., Liscidini, M., and Redorici, L. (2019). Silicon solar cells: toward the efficiency limits. *Advances in Physics: X*, 4(1):1548305.

[Andrews and Jelly, 2017] Andrews, J. and Jelly, N. (2017). Energy science.

[Apogee, 2018] Apogee (2018). Sp-510 user manual.

[Baran and Wu, 1989] Baran, M. and Wu, F. F. (1989). Optimal sizing of capacitors placed on a radial distribution system. *IEEE Transactions on Power Delivery*, 4(1):735–743.

[Bhatnagar and Nema, 2013] Bhatnagar, P. and Nema, R. (2013). Maximum power point tracking control techniques: State-of-the-art in photovoltaic applications. *Renewable and Sustainable Energy Reviews*, 23:224 – 241.

[Bioforsk, 2018] Bioforsk (2018). Om målestasjoner.

[Bourne, 2017] Bourne, B. (2017). Ground albedo field measurements.

[Byrne et al., 2018] Byrne, R. H., Nguyen, T. A., Copp, D. A., Chalamala, B. R., and Gyuk, I. (2018). Energy management and optimization methods for grid energy storage systems. *IEEE Access*, 6:13231–13260.

[Chis et al., 1997] Chis, M., Salama, M. M. A., and Jayaram, S. (1997). Capacitor placement in distribution systems using heuristic search strategies. *IEE Proceedings - Generation, Transmission and Distribution*, 144(3):225–230.

[Colmenar-Santos et al., 2014] Colmenar-Santos, A., Campinez-Romero, S., Enriquez-Garcia, L. A., and Perez-Molina, C. (2014). Simplified analysis of the electrical power losses for on-shore wind farms considering weibull distribution parameters.

[Coster, 2010] Coster, E. J. (2010). Distribution grid operation including distributed generation.

[Deign, 2018] Deign, J. (2018). New efficiency record for perovskite solar.

[Disha, 2018] Disha, M. (2018). Correlation: Meaning, types, and computations.

[Djohra et al., 2014] Djohra, S., Mustapha, K., and Hadji, S. (2014). Technical and economic study of a stand-alone wind energy system for remote rural area electrification in algeria. *Renewable Energy and Power Quality Journal*, pages 638–643.

[EIA, 2018] EIA (2018). U.s. battery storage market trends.

[eKlima, 2019] eKlima (2019).

[Eller and Gauntlett, 2017] Eller, A. and Gauntlett, D. (2017). Energy storage trends and opportunities in emerging markets.

[EnergiNorge, 2018] EnergiNorge (2018). Nettstruktur og organisering.

[Energy, 2019] Energy, H. (2019). Homer pro user manual.

[EnergyStar, 2013] EnergyStar (2013). Energy star market and industry scoping report.

[Ertugrul, 2016] Ertugrul, N. (2016). Battery storage technologies, applications and trend in renewable energy. In *2016 IEEE International Conference on Sustainable Energy Technologies (ICSET)*, pages 420–425.

[Foster et al., 2006] Foster, S., Xu, L., and Fox, B. (2006). Grid integration of wind farms using svc and statcom. In *Proceedings of the 41st International Universities Power Engineering Conference*, volume 1, pages 157–161.

[Fraunhofer, 2019] Fraunhofer (2019). Photovoltaics report.

[Fuchs and Masoum, 2008] Fuchs, E. F. and Masoum, M. A. (2008). Chapter 10 - optimal placement and sizing of shunt capacitor banks in the presence of harmonics. In *Power Quality in Power Systems and Electrical Machines*, pages 397 – 441. Academic Press, Burlington.

[Goldberg, 2012] Goldberg, L. H. (2012). Active bypass diodes improve solar panel efficiency and performance.

[Goudarzi and Zhu, 2013] Goudarzi, N. and Zhu, W. (2013). A review of the development of wind turbine generators across the world. *International Journal of Dynamics and Control*, 1.

[Gueymard, 2018] Gueymard, C. A. (2018). Revised composite extraterrestrial spectrum based on recent solar irradiance observations. *Solar Energy*, 169:434 – 440.

[Gyuk et al., 2014] Gyuk, I., Johnson, M., and Vetrano, J. (2014). Grid energy storage.

[Hesse et al., 2017] Hesse, H., Schimpe, M., Kucevic, D., and Jossen, A. (2017). Lithium-ion battery storage for the grid—a review of stationary battery storage system design tailored for applications in modern power grids. *Energies*, 10:2107.

[Honsberg and Bowden, 2015] Honsberg, C. and Bowden, S. (2015). Pv education.

[Ierides et al., 2018] Ierides, M., Suarez, E., Fernandez, V., and Bax, L. (2018). Battery energy storage.

[Jordan et al., 2016] Jordan, D. C., Kurtz, S. R., VanSant, K., and Newmiller,

J. (2016). *Compendium of photovoltaic degradation rates*. JOHN WILEY & SONS.

[Katsigiannis et al., 2013] Katsigiannis, Y. A., Stavrakakis, G. S., and Pharconides, C. (2013). Effect of wind turbine classes on the electricity production of wind farms in cyprus island. 2013:6.

[Kleinberg and Miu, 2011] Kleinberg, M. and Miu, K. (2011). A study of distributed capacitor control for electric power distribution systems. In *2011 North American Power Symposium*, pages 1–6.

[Knight, 2000] Knight, K. (2000). *Mathematical Statistics*. Chapman & Hall.

[Kroposki et al., 2006] Kroposki, B., Basso, T., DeBlasio, R., and Friedman, N. R. (2006). *Interconnection of Alternative Energy Sources with the Grid*, chapter 14, pages 354–378. John Wiley & Sons, Ltd.

[Leitermann, 2012] Leitermann, O. (2012). *Energy Storage for Frequency Regulation on the Electric Grid*. PhD thesis, Massachusetts Institute of Technology.

[Lopes and Fernandes, 2014] Lopes, D. A. R. and Fernandes, A. R. (2014). Atmospheric scattering - state of the art.

[Lovdata, 2019] Lovdata (2019). Forskrift om leveringskvalitet i kraftsystemet.

[Luo et al., 2015] Luo, X., Wang, J., Dooner, M., and Clarke, J. (2015). Overview of current development in electrical energy storage technologies and the application potential in power system operation. *Applied Energy*, 137:511 – 536.

[Lydia et al., 2014] Lydia, M., Kumar, S. S., Selvakumar, A. I., and Kumar, G. E. P. (2014). A comprehensive review on wind turbine power curve modeling techniques. *Renewable and Sustainable Energy Reviews*, 30:452 – 460.

[Machowski, 2008] Machowski, J. (2008). Power system dynamics : stability and control.

[Masters, 2013] Masters, G. M. (2013). *Renewable and Efficient Electric Power Systems*. JOHN WILEY & SONS.

[MIT, 2008] MIT (2008). A guide to understanding battery specifications.

[Miu et al., 1997] Miu, K. N., Chiang, H. ., and Darling, G. (1997). Capacitor placement, replacement and control in large-scale distribution systems

by a ga-based two-stage algorithm. *IEEE Transactions on Power Systems*, 12(3):1160–1166.

[Ndiaye et al., 2013] Ndiaye, A., Charki, A., Kobi, A., Kébé, C., Ndiaye, P., and Sambou, V. (2013). Degradations of silicon photovoltaic modules: A literature review. *Solar Energy*, 96:140–151.

[NEPSI, 2012] NEPSI (2012). Step and size considerations.

[Niayifar and Porté-Agel, 2016] Niayifar, A. and Porté-Agel, F. (2016). Analytical modeling of wind farms: A new approach for power prediction. *Energies*, 9:741.

[Njiri and Söffker, 2016] Njiri, J. G. and Söffker, D. (2016). State-of-the-art in wind turbine control: Trends and challenges. *Renewable and Sustainable Energy Reviews*, 60:377 – 393.

[Norge, 2018] Norge, S. (2018). Snødekke 1971-2000.

[Norgeskart, 2019a] Norgeskart (2019a). Corine landcover norge.

[Norgeskart, 2019b] Norgeskart (2019b). Kart over norge.

[NVE, 2007] NVE (2007). Anleggskonsesjon for vindkraftverk med installert effekt < 10 mw.

[NVE, 2019] NVE (2019). Karttjenester.

[Panasonic, 2017] Panasonic (2017). Photovoltaic module hit product sheet.

[Powel, 2019] Powel (2019). Netbas documentation.

[Powers et al., 2017] Powers, J. G., Klemp, J. B., Skamarock, W. C., Davis, C. A., Dudhia, J., Gill, D. O., Coen, J. L., Gochis, D. J., Ahmadov, R., Peckham, S. E., Grell, G. A., Michalakes, J., Trahan, S., Benjamin, S. G., Alexander, C. R., Dimego, G. J., Wang, W., Schwartz, C. S., Romine, G. S., Liu, Z., Snyder, C., Chen, F., Barlage, M. J., Yu, W., and Duda, M. G. (2017). The weather research and forecasting model: Overview, system efforts, and future directions. *Bulletin of the American Meteorological Society*, 98(8):1717–1737.

[Rahimi et al., 2013] Rahimi, A., Zarghami, M., Vaziri, M., and Vadhva, S. (2013). A simple and effective approach for peak load shaving using battery storage systems. In *2013 North American Power Symposium (NAPS)*, pages 1–5.

[Rana, 2012] Rana, A. (2012). *Role of Remote Sensing and GIS in Agrometeorology*.

[Riffonneau et al., 2011] Riffonneau, Y., Bacha, S., Barruel, F., and Ploix, S. (2011). Optimal power flow management for grid connected pv systems with batteries. *IEEE Transactions on Sustainable Energy*, 2(3):309–320.

[Robson and Bonomi, 2018] Robson, P. and Bonomi, D. (2018). Growing the battery storage market 2018.

[Romero-Cadaval et al., 2013] Romero-Cadaval, E., Spagnuolo, G., Franquelo, L. G., Ramos-Paja, C. A., Suntio, T., and Xiao, W. M. (2013). Grid-connected photovoltaic generation plants: Components and operation. *IEEE Industrial Electronics Magazine*, 7(3):6–20.

[Rühle, 2016] Rühle, S. (2016). Tabulated values of the shockley–queisser limit for single junction solar cells. *Solar Energy*, 130:139 – 147.

[Saadat, 2010] Saadat, H. (2010). Power system analysis.

[Sallam et al., 1994] Sallam, A. A., Desouky, M., and Desouky, H. (1994). Shunt capacitor effect on electrical distribution system reliability. *IEEE Transactions on Reliability*, 43(1):170–176.

[Seljeseth, 2013] Seljeseth, H. (2013). Det norske distribusjonsnettet.

[Singh et al., 2009] Singh, B., Saha, R., Chandra, A., and Al-Haddad, K. (2009). Static synchronous compensators (statcom): a review. *IET Power Electronics*, 2(4):297–324.

[Sinha et al., 2014] Sinha, D., Das, A. B., Dhak, D. K., and Sadhu, P. K. (2014). Equivalent circuit configuration for solar pv cell. In *2014 1st International Conference on Non Conventional Energy (ICONCE 2014)*, pages 58–60.

[Solenergi, 2017] Solenergi (2017). Solceller.

[Sourkounis and Tourou, 2013] Sourkounis, C. and Tourou, P. (2013). Grid code requirements for wind power integration in europe. 2013:9.

[Stoker, 2018] Stoker, L. (2018). Five considerations for east-west solar design.

[Tande et al., 2007] Tande, J. O., Marzio, G. D., and Uhlen, K. (2007). System requirements for wind power plants.

[TKN, 2016] TKN (2016). Energiforbruk i sjømatsregionen senja 2016-2030.

[TKN, 2018] TKN (2018). Regional kraftsystemsutredning for område 21.

[TKN, 2019] TKN (2019). Tall fra kraftsystemet.

[Tønne et al., 2014] Tønne, E., Foosnæs, J. A., and Sand, K. (2014). Planlegging av fremtidens smarte aktive distribusjonsnett.

[Vestas, 2019] Vestas (2019). 4 mw platform.

[Vita et al., 2015] Vita, V., Alimardan, T., and Ekonomou, L. (2015). The impact of distributed generation in the distribution networks' voltage profile and energy losses. In *2015 IEEE European Modelling Symposium (EMS)*, pages 260–265.

[Wang et al., 2018a] Wang, C., Graham, R. M., Wang, K., Gerland, S., and Granskog, M. A. (2018a). Comparison of era5 and era-interim near surface air temperature and precipitation over arctic sea ice: Effects on sea ice thermodynamics and evolution.

[Wang et al., 2018b] Wang, Z., Tian, W., and Hu, H. (2018b). A comparative study on the aeromechanic performances of upwind and downwind horizontal-axis wind turbines. *Energy Conversion and Management*, 163:100 – 110.

[WE, 2018] WE (2018). Wind energy in europe.

[Weihao Hu et al., 2010] Weihao Hu, Zhe Chen, and Bak-Jensen, B. (2010). Optimal operation strategy of battery energy storage system to real-time electricity price in denmark. In *IEEE PES General Meeting*, pages 1–7.

[windturbinemodels, 2015] windturbinemodels (2015). Vestas v126-3.3 datasheet.

[Wolfgang et al., 2009] Wolfgang, O., Haugstad, A., Mo, B., Gjelsvik, A., Wangensteen, I., and Doorman, G. (2009). Hydro reservoir handling in norway before and after deregulation. *Energy*, 34(10):1642 – 1651. 11th Conference on Process Integration, Modelling and Optimisation for Energy Saving and Pollution Reduction.

[Youn and Cho, 2009] Youn, L. T. and Cho, S. (2009). Optimal operation of energy storage using linear programming technique.

[Zeqiang et al., 2013] Zeqiang, B., Wenhua, L., Yizhuo, S., Xiaolei, and Wei, C. (2013). Research on performance test method of silicon pyranometer. *IEEE International Conference on Electronic Measurement & Instruments*, 11.